

UC San Diego

UC San Diego Electronic Theses and Dissertations

Title

Computational and pharmacological modeling of membrane proteins

Permalink

<https://escholarship.org/uc/item/8429d1xn>

Author

Babakhani, Arneh

Publication Date

2009

Peer reviewed|Thesis/dissertation

UNIVERSITY OF CALIFORNIA, SAN DIEGO

Computational and Pharmacological Modeling of Membrane Proteins

A dissertation submitted in partial satisfaction of the
requirements for the degree Doctor of Philosophy

in

Chemistry with specialization in Computational Science

by

Arneh Babakhani

Committee in charge:

Professor J. Andrew McCammon, Chair
Professor Michael Holst
Professor Judy E. Kim
Professor Katja Lindenberg
Professor Stanley J. Opella

2009

Copyright

Arneh Babakhani, 2009

All rights reserved.

The Dissertation of Arneh Babakhani is approved, and it is acceptable in quality and form for publication on microfilm and electronically:

Chair

University of California, San Diego

2009

DEDICATION

*To Daniela and Lucas, for teaching me how to smile and
enjoy the simpler things in life.*

EPIGRAPH

Computers are incredibly fast, accurate, and stupid. Human beings are incredibly slow, inaccurate, and brilliant. Together they are powerful beyond imagination.

Albert Einstein

TABLE OF CONTENTS

Signature Page	iii
Dedication	iv
Epigraph	v
Table of Contents	vi
List of Abbreviations	viii
List of Figures	x
List of Tables	xiii
Acknowledgements	xiv
Vita, Publications, Fields of Study	xviii
Abstract of the Dissertation	xx
Chapter 1: An Introduction to Computing in Biochemical Phenomena	1
Chapter 2: Computational Investigation of Pressure Profiles in Lipid Bilayers with Embedded Proteins	12
2.1 Introduction	12
2.2 Materials and Methods	15
2.3 Results	21
2.4 Discussion	28
2.5 Acknowledgements	30
Chapter 3: Peptide Insertion, Positioning, and Stabilization in a Membrane: Insight from an All-Atom Molecular Dynamics Simulation	31
3.1 Introduction	31
3.2 Materials and Methods	34
3.3 Results and Discussion	35
3.4 Conclusion	48
3.5 Acknowledgements	50
Chapter 4: Thermodynamics of Peptide Insertion and Aggregation in a Lipid Bilayer	51
4.1 Introduction	51
4.2 Materials and Methods	53
4.3 Results and Discussion	58

4.4 Conclusion	74
4.5 Acknowledgements	75
Chapter 5: A Virtual Screening Study of the Acetylcholine Binding Protein using a Relaxed-complex Approach	76
5.1 Introduction	76
5.2 Materials and Methods	82
5.3 Results and Discussion	85
5.4 Conclusion	103
5.5 Acknowledgements	105
Chapter 6: Inhibitor Binding of Group IVA Phospholipase A ₂ Probed by Molecular Dynamics and Deuterium Exchange Mass Spectrometry ...	106
6.1 Introduction	106
6.2 Materials and Methods	110
6.3 Results and Discussion	116
6.4 Conclusion	130
6.5 Acknowledgements	130
Appendix	132
References	138

LIST OF ABBREVIATIONS

Ac	<i>Aplysia californica</i> species of AChBP
AChBP	Acetylcholine Binding Protein
ATK	Arachidonyl Trifluoromethyl Ketones
Bt	<i>Bulinus truncates</i> species of AChBP
DMPC	Dimyristoylphosphatidylcholine
DOPA	Dioleoylphosphatidic Acid
DXMS	Deuterium Exchange Mass Spectrometry
GIVA CPLA2	Group IVA Phospholipase A2
GROMACS	Groningen Machine for Chemical Simulation (software)
LGIC	Ligand-Gated Ion Channels
LINCS	Linear Constant Solver
Ls	<i>Lymnaea stagnalis</i> species of AChBP
MAFP	Methyl Arachidonyl Fluoro Phosphonate
MD	Molecular Dynamics
MLT	Melittin
nAChR	Nicotinic Acetylcholine Receptor
NAMD	Nanoscale Molecular Dynamics (software)
NCI	National Cancer Institute
NCIDS	National Cancer Institute Diversity Set
NMR	Nuclear Magnetic Resonance
PDB	Protein Data Bank
PME	Particle mesh Ewald

PMF	Potential of Mean Force
RMSD	Root Mean Square Deviation
RMSF	Root Mean Square Fluctuation
SMD	Steered Molecular Dynamics
SPC	Simple Point Charge
TRP	Tryptophan
VMD	Visual Molecular Dynamics (software)
WL5	Peptide (tryptophan + 5 leucines)

LIST OF FIGURES

Figure 1: Initial snapshot of melittin-DMPC system	16
Figure 2: Distribution of melittin & lateral pressure profile	22
Figure 3: Partial pressures of melittin	26
Figure 4: Protein–lipid interactions in DMPC+melittin system.....	29
Figure 5: Simulation snapshots at a) 25 ns and b) 50 ns	37
Figure 6: Position along the membrane normal vector (z-axis) of the peptide	38
Figure 7: Average number of hydrogen bonds formed	40
Figure 8: Orientation angles of the peptide and tryptophan side chain.....	42
Figure 9: Ramachandran plot	44
Figure 10: Displacement of the center of mass of the peptide	45
Figure 11: Deuterium lipid order parameters of the acyl chains in DMPC	47
Figure 12: The free energy profile of the peptide as a function of position	59
Figure 13: The extent of convergence of the free energy profile	60
Figure 14: Ramachandran plots of the internal leucine residues in WL5	61
Figure 15: Nitrogen heteroatom distribution along the reaction coordinate	62
Figure 16: Snapshots of WL5 in the upper and lower leaflets of the membrane	63
Figure 17: Hydrogen bonds between the indole nitrogen and lipids	64
Figure 18: Peptide tilt as a function of position along the z-axis	65
Figure 19: Root mean square fluctuation (RMSF) of the peptide	68
Figure 20: RMSD of the peptide as a function of position	69
Figure 21: A proposed thermodynamic cycle of peptide insertion	70
Figure 22: Snapshots from the molecular dynamics simulation of AChBP.....	86

Figure 23: Docked vs. crystal structures of some common ligands vs. AChBP	88
Figure 24: Calculated free energies of binding vs, experimental values	90
Figure 25: Molecular weight vs. the calculated free energy of binding	91
Figure 26: Free energies of binding of all docked conformations	91
Figure 27: Front and rear views of the binding (interfacial) site	92
Figure 28: The frequency of contacts	92
Figure 29: NCI 105017, binding against Ls AChBP	94
Figure 30: The extensive hydrogen-bonding character of NCI 108608	95
Figure 31: Binding of 2-amino-6-((7-(hydroxy(oxido)amino).....	97
Figure 32: 5-(2-(1H-tetraazol-5-yl)ethyl)-1H-tetraazole (NCI 282034)	99
Figure 33: 2D Structure of Tolypomycin (NCI 177383) and binding.....	101
Figure 34: Structural sequence alignments of the AChBP	102
Figure 35: Inhibitors of GIVA PLA ₂	108
Figure 36: Deuterium exchange 10 μM Pyrrophenone or AX007	113
Figure 37: Modeling uncrystalized residues	114
Figure 38: Peptide digest map of GIVA PLA ₂	117
Figure 39: Root mean square distance of protein and inhibitor	118
Figure 40: Deuterium exchange information	120
Figure 41: Regions in contact with inhibitors	121
Figure 42: Deuterium exchange upon binding of 10 μM Pyrrophenone.....	123
Figure 43: Residues involved in the binding pyrrophenone	124
Figure 44: Deuterium exchange upon binding of 10 μM AX007	126

Figure 45: Residues involved in the binding of the Oxoamide AX007.....	128
Figure 46: Different inhibitors cause different rates of exchange.....	129

LIST OF TABLES

Table 1: Per-monolayer tension computed from pressure profile	23
Table 2: A comparison of the docked and experimental results.....	87

ACKNOWLEDGEMENTS

First and foremost, I would like to acknowledge my adviser and committee chair, Professor J. Andrew McCammon, for providing such a warm and productive environment for scientific discourse. From day one of my affiliation, the McCammon Lab has been a welcoming and nurturing group. Professor McCammon goes to great lengths to make sure all of us are well-funded, well-equipped, and well-fed! His effort ensures that all of us achieve our utmost scientific potential. I tell incoming members that the hardest thing about the McCammon Lab is *having to leave it*. Because when the time does come to leave, you're uncertain whether you'll ever work again in a group as cultivating and collaborative as this one!

Acknowledgements are in order for some particular members of the McCammon Lab. I thank Patricia Craft, our administrative assistant, for making sure that I was always paid, happy, and caffeinated! I thank Professor Donald Hamelberg (now at Georgia State University) for initially setting me up in the lab and taking care of my computing needs. I thank Professor Alemayehu Gorfe (now at the University of Texas at Houston) and Dr. Justin Gullingsrud (now at D. E. Shaw Research) for guiding me through the intricacies of molecular dynamics simulations and membrane modeling. I thank post-doctoral fellow, Dr. Rommie Amaro, for many helpful discussions regarding virtual screening techniques and drug discovery. I thank Barrett Abel for all of his assistance with computing requirements towards the end of my time here in the group. Last, but most certainly not least, I thank the huge cadre of graduate students and post-docs in the group—including David Minh, Robert Swift, Mikolai Fajer, Morgan Lawrenz, Dr. Barry

Grant, Dr. Riccardo Baron, Dr. Ilja Khavrutskii, Dr. Cesar de Oliveira, Dr. Dong Xu—for many discussions ranging from chemistry to computers, to college football and beer!

I also thank Professor Michael Holst for introducing and accepting me into the Computational Science Math & Engineering (CSME, <http://csme.ucsd.edu/>) program here at U.C. San Diego. A few years ago, Professor Holst realized that computational science plays an integral role in the research of many graduate students from a variety of departments. He created the CSME program to foster a more in-depth education in aspects of scientific computing for such students. Indeed, the program has provided me with a deeper understanding and appreciation for computational science in my own research and scientific endeavors. I hope that future computing students here at UCSD continue to embrace this program as it further develops and flourishes.

In every computational effort that I made as a graduate student, I always strived to tie my results and thinking with some experimental component. I learned quickly that the coupling of computational and experimental findings can yield a much grander understanding than any single component by itself. Thus, it is imperative that I thank my experimental collaborators—Professor Judy E. Kim (and members of her lab), as well as Dr. Todd Talley and the rest of the Palmer Taylor Lab—for their guidance and for allowing me to dabble in some experimental chemistry. I also thank Dr. John Burke and members of the Edward Dennis Lab for their collaborative efforts. I was fortunate to have these experimentalists co-located here with me at UCSD. This proximity and their willingness made for very feasible relationships in which data, information and ideas were seamlessly transferred. I cherished our team efforts, and this model of success via

collaboration is one of the most important lessons that I have learned as a graduate student.

I thank my doctoral committee, Professors J. A. McCammon (chair), Judy E. Kim, Katja Lindenberg, Stanley Opella, and Michael Holst. All members gave great guidance and were very amenable to my scheduling needs. I thank them for keeping me on track!

Above all, I thank my wife Daniela and my son Lucas for providing warm familial support, without which none of this would have been possible. Having such a strong foundation at home makes school more manageable and stress-free. I also thank our parents, siblings, and extended family for their love and support.

Authorship Acknowledgements:

Chapter 2, in full, is a near reprint of the material as it appears in *Molecular Simulation* 2006, Volume 32, Pages 831-838. The dissertation author and J. Gullingsrud were the primary co-contributors to this work. J. A. McCammon served as the head adviser and principal investigator.

Chapter 3, in full, is a near reprint of the material as it appears in *Biopolymers* 2007, Volume 85, Pages 490-497. The dissertation author was the primary investigator and author of this paper. A. A. Gorfe, J. Gullingsrud, and J. E. Kim contributed in an advisory capacity. J. A. McCammon served as the head adviser and principal investigator.

Chapter 4, in full, is a near reprint of the material as it appears in the *Journal of Physical Chemistry B* 2008, Volume 112, Pages 10528-10534. The dissertation author was the primary investigator and author of this paper. A. A. Gorfe and J. E. Kim

contributed in an advisory capacity. J. A. McCammon served as the head adviser and principal investigator.

Chapter 5, in full, is a near reprint of the material as it appears in *Computational Biology and Chemistry* 2009, Volume 33, Pages 160-170. The dissertation author was the primary investigator and author of this paper. T. T. Talley and P. Taylor contributed in an advisory capacity. J. A. McCammon served as the head adviser and principal investigator.

Chapter 6, in full, is a near reprint of the material as it appears in a submission to the *Journal of the American Chemical Society* 2009. The dissertation author and J. Burke were the primary co-contributors to this work. A. A. Gorfe, G. Kokotos, S. Li, and V. Woods contributed in an advisory capacity. J. A. McCammon and E. Dennis served as the head advisers/principal investigators of the computational and experimental components (respectively) of the work.

VITA

- 1996 – 2000 Bachelor of Science, Chemistry
University of California at Berkeley
Undergraduate Research Mentor: Prof. Carolyn R. Bertozzi
- 2001 – 2005 United States Naval Officer, Active Duty, San Diego, CA
- 2005 – 2009 United States Naval Officer, Active Reserve Duty, San Diego, CA
- 2005 – 2006 Teaching Assistant, University of California at San Diego
- 2005 – 2007 Master of Science, Chemistry
University of California at San Diego
- 2005 – 2009 Graduate Student Researcher
University of California at San Diego
Department of Chemistry & Biochemistry
Adviser: Prof. J. Andrew McCammon
- 2005 – 2009 Doctor of Philosophy, Chemistry,
with a specialization in Computational Science
University of California at San Diego
Dissertation: “Computational and Pharmacological Modeling of
Membrane Proteins”

PUBLICATIONS

1. Burke, J.; Babakhani, A.; Gorfe, A. A.; Kokotos, G.; Li, S.; Woods, V.; McCammon, J. A.; Dennis, E. *Inhibitor Binding of Group IVA Phospholipase A2 probed by molecular dynamics and deuterium exchange mass spectrometry* **2009**, Journal of the American Chemical Society, Accepted.
2. Babakhani, A.; Talley, T. T.; Taylor, P.; McCammon, J. A. *A virtual screening study of the acetylcholine binding protein using a relaxed complex approach* **2009**, Computational Biology and Chemistry, 33, 160-170.
<http://dx.doi.org/10.1016/j.compbiolchem.2008.12.002>
3. Babakhani, A.; Gorfe, A. A.; Kim, J. E.; McCammon, J. A. *Thermodynamics of peptide insertion and aggregation in a lipid bilayer* **2008**, Journal of Physical Chemistry B, 112, 10528–10534.
<http://pubs.acs.org/cgi-bin/abstract.cgi/jpcb/2008/112/i34/abs/jp804710v.html>

4. Gorfe, A. A.; Babakhani, A.; McCammon, J. A. *H-ras protein in a bilayer: interaction and structure perturbation* **2007**, Journal of the American Chemical Society, 129, 12280-12286.
<http://pubs.acs.org/cgi-bin/abstract.cgi/jacsat/asap/abs/ja073949v.html>
5. Gorfe, A. A.; Babakhani, A.; McCammon, J. A. *Free energy profile of H-ras membrane anchor upon membrane insertion* **2007**, Angewandte Chemie International Edition, 46, 8234-8237.
<http://www3.interscience.wiley.com/journal/116321299/abstract>
6. Babakhani, A.; Gorfe, A. A.; Gullingsrud, J.; Kim, J. E.; McCammon, J. A. *Peptide insertion, positioning, and stabilization in a membrane: insight from an all-atom molecular dynamics simulation* **2007**, Biopolymers, 85, 490-497.
<http://www3.interscience.wiley.com/journal/114107490/abstract>
7. Gullingsrud, J.; Babakhani, A.; McCammon, J. A. *Computational investigation of pressure profiles in lipid bilayers with embedded proteins* **2006**, Molecular Simulation, 32, 831-838.
<http://www.journalsonline.tandf.co.uk/link.asp?id=l57842265v8r04m5>

FIELDS OF STUDY

Major Field: Chemistry, with specialization in Computational Science

Studies in Peptide-Membrane Interactions and Thermodynamics
Professors J. Andrew McCammon and Judy E. Kim

Studies in Computational Science Techniques and Applications
Professors J. Andrew McCammon and Michael Holst

Studies in Pharmacological Modeling and Drug Discovery
Professors J. Andrew McCammon, Palmer Taylor, and Edward Dennis

ABSTRACT OF THE DISSERTATION

Computational and Pharmacological Modeling of Membrane Proteins

by

Arneh Babakhani

Doctor of Philosophy in Chemistry with specialization in Computational Science

University of California, San Diego, 2009

Professor J. Andrew McCammon, Chair

Computational modeling has played a great role in solving many questions in biochemical and biomedical research. Computers in chemistry are now readily used to study enzymatic reactions, protein-ligand binding, protein folding, macromolecular assembly and other dynamical phenomena. Particularly, in the realm of cell membrane and transmembrane-protein chemistry, computer modeling has provided a great deal of information and guidance. The research presented here in this dissertation furthers the

body of work in membrane-protein modeling. The mechanical properties of membranes—tension and lateral pressure—are demonstrated along with the change in these features when a peptide (melittin) is inserted into the membrane. By the simulation technique of umbrella sampling, the thermodynamics of a model hexapeptide (WL5) are probed, as it transverses the span of a membrane. The first free energy calculation of such a system is presented. Coupled with previous experimental findings, a grand model of peptide insertion and aggregation in a membrane host is assembled. Membrane proteins also serve as pharmacological targets in drug discovery. The work presented here focuses on the acetylcholine binding protein (AChBP), a surrogate structure of the nicotinic acetylcholine receptor (nAChR). A virtual screening study was conducted using the relaxed-complex method—in which protein flexibility is captured via a molecular dynamics simulation—of AChBP against a database of ligands from the National Cancer Institute (NCI). The study shows that several small molecule ligands from NCI can bind AChBP and possibly nAChR. Such ligands can serve to differentiate between the three species of AChBP and between the subtypes of the receptor. Furthermore, such ligands can resemble agonistic/antagonistic behavior of addictive narcotics, thus aiding in counter-drug addiction treatments. A final, peripheral membrane-protein is also studied here; a molecular dynamics simulation of the cytosolic phospholipase A₂ (CPLA2) is conducted, along with a docking study of its known inhibitors. The results are correlated with experimental deuterium exchange data, to afford a broader understanding of protein-ligand interactions in this system. As CPLA2 is an important target in pharmacology, this work contributes to the design of novel ligands that can bind appreciably to the enzyme.

CHAPTER 1: An Introduction to Computing in Biochemical Phenomena

Examining scientific history, one can easily highlight several inventions that have significantly affected the trajectory of human existence. To mention only a few, one could cite the inventions of the reading glasses, the telescope, the microscope, the telephone and penicillin. Particularly in the 20th Century, man enjoyed a great renaissance in technological innovation; and arguably the single most important invention to stem from the 20th Century was the computer, an electrical device capable of carrying out simple calculations in a repetitive and rapid manner. Yet, what distinguishes the computer from other inventions is that it is not a static product. The computer is always changing with respect to function, accuracy, speed and size. This last quality is best demonstrated by the cell phones of today that harbor the computing power of once warehouse-sized machines! To put it mildly, computers have changed many aspects of our lives. Man employs them for a wide spectrum of tasks, including weapons control, security, personal finance, work, leisure, communication, etc. With the advent of the Internet, computers can be used to seamlessly transfer information in quantities and with speeds unimaginable by previous generations. And as we continue to use computers on a hourly basis in our lives, we observe the computer changing both functionally and aesthetically, to meet all of our professional and personal needs.

The scientific communities—particularly those in the physical sciences, such as physics, mathematics and engineering—were the first to harness the power of computing

in their professional forums.¹ Computers made it possible to carry out numerous and mundane calculations once the theory of such work was grounded. For instance, in the study of partial differential equations, although the equations were well-posed, the solutions were unattainable or lacked analytical forms. With the advent of computing, these equations—which span many disciplines—were solved numerically by carrying out many calculations using computers.²

Such numerical methods became the pillar of scientific computing and held the throne until the 1970s, when the art of scientific simulation came on the horizon.³ As computing and visualization technology advanced, scientists took advantage of this ongoing renaissance by devising simulation schemes. In a simulation, the same numerical procedures are carried out as before, but a visual element can also be added to show (for instance) how a particular solution of a differential equation changes as the boundary conditions are varied. The simulations can also demonstrate a model for the real physical world. Fluid mechanics simulations can demonstrate the movement of an eddy in the ocean,⁴ geophysicists can simulate an earthquake,⁵ and chemists can simulate the dynamics of molecules.⁶ This world of simulation and the accompanying visualization now intersects with many roads in our lives; from computer-animated graphics in video games and movies, to scientific models that yield a better understanding of the physical world, it is now hard to imagine a life without computing power and simulation.

In science, investigators have been using computers to solve complex problems for over 70 years.⁷ As technology evolved throughout this time, so too did the relationship between scientists and computing. The first computers filled up entire buildings and scientists went through laborious tasks to employ them.⁸ But as computers

advanced, they became smaller and more easily accessible. Once their spatial requirements were reduced down to the size of a large room, laboratories all around the globe began to purchase computers and integrate them into research. And with the relatively recent advent of the personal computer, nowadays, one would be hard-pressed to find a single office without a computer.⁹

Along with the technological advances in computing, another (and arguably more important) change occurred, regarding the mindset of scientists and how they conduct their research. At the beginning of the computing age, scientists would first formulate their ideas and mathematical notions without consideration of computing techniques. Later, they would write code trying to emulate their formulations, but the former could never influence their thinking regarding the latter. In other words, they viewed their traditional formulations as ground truth and forced the computing code to follow suit. Oftentimes, the result was an inefficient computational method.¹

In due time, it dawned on many scientists that if they can construct their formulations with the computing code in mind, then they can employ computers to carry out their calculations in more efficient and accurate ways. Even if a particular algorithm was correct and elegant on paper, if the scientist knew that that algorithm would become cumbersome in computing, then that algorithm was immediately discarded. It was replaced with a more efficient one.¹⁰ This type of forward thinking at the conception level is now common practice among all scientists. Every time a mathematician pens a new algorithm for numerical optimization, or when a chemist scribbles down a new formulation for molecular dynamics, he/she is thinking, “How can I code this? How can this be implemented in C++, PERL, MATLAB, etc?”

Although computers and science have been intertwined for decades now, their relationship has enjoyed a stimulating growth particularly over the past 20 years. With the advent of faster processors, larger memory storage, and more feasible inter-hardware communication, today, even a modest desktop computer can perform many scientific calculations and simulations. The user no longer requires a warehouse full of machines for simple scientific tasks.⁹ Moreover, parallel programming codes and architecture make it possible for one to link up two or more desktop machines (or simply their processors), for even faster computing. In such a parallel fashion, even a small cluster can perform at the level of yesterday's supercomputer. Parallel processing has catapulted scientific thinking into realms that were once thought to be unreachable.¹¹ Running on hundreds, thousands, even tens of thousands of processors, scientists can simulate and study events that are unfeasible by experimental means, such as the collision of galaxies.¹² If the invention of computing can be heralded as one of the great inventions of the 20th Century, then undoubtedly, parallel computing will be held in the same light from the current era.

The other dramatic change that has occurred over the past 20 years is in the demographics of the computing community. What used to be a body of only "hard" scientists (those rooted deeply in the physical sciences) now consists of investigators from many disciplines. Epidemiologists use computational science to probe the spread of disease,¹³ while financial analysts use modeling to simulate stock market fluctuations.¹⁴ Many subjects now reap the benefits of computing power. The ease of numerical calculations, the predictive power of simulation, and the visual insight gained from modeling are but a few of the advantages afforded by computational science, across a

variety of genres. In due time, every discipline will have a significant computational component to it.

In the discipline of chemistry, many problems lend themselves to the art of scientific computing. In general, these problems can be divided into the following categories: many-body problems, such as molecular dynamics (MD), where the interactions of several atoms or molecules are simulated, usually in a classical manner; quantum chemical calculations, where numerical computing is used to solve a complex partial differential equation, namely the Schrodinger Equation; energetic calculations pertaining to conformational and/or electronic states of molecules (for instance, the calculation showing that one protein conformer is more stable than the other, i.e. the protein folding problem); and the calculation of thermodynamic parameters (such as entropy, enthalpy, free energy) in various chemical interactions. The importance of computers in chemistry was recognized in a grand sense, by the 1998 Nobel Prize in chemistry. The award went to Walter Kohn and John A. Pople, for their efforts in the field of quantum computing, including the discovery and implementation of density functional theory (DFT).^{15,16}

In all of the aforementioned categories, computational science continues to propel chemical thinking in the modern day. Particularly in biochemistry, scientists employ computers to study a variety of phenomena, such as biomolecular dynamics, protein folding, and protein-ligand interactions. The first computational approaches in biochemistry arose in the 1970s, during which the structure and dynamics of proteins were elucidated.^{17,18} Throughout the 1980s, various techniques in molecular dynamics paved the way for the first biochemical simulations. Computational code such as

GROMACS¹⁹ and AMBER²⁰ made it possible to construct movies of dynamical events in biochemistry, thus affording new knowledge in the field. In the 1990s, parallel computing was integrated into much of the computational chemistry codes, such as NAMD,²¹ making it possible to run even larger simulations. In the current decade, the computational study of protein-ligand interactions, more commonly termed as ‘docking’, has also become a central theme in chemical computing.²² All of this biochemical computing has advanced so quickly and thoroughly that today, it can be used to augment, predict, and guide experimental endeavors. Biochemical computing now plays a crucial role in research, in both academia and industry. As stated by Professor Tamar Schlick of New York University:²³

In biomolecular modeling, a multidisciplinary approach is important not only because of the many aspects involved—from problem formulation to solution—but also since the best computational approach is often closely tailored to the biological problem. In the same spirit, close connections between theory and experiment are essential: computational models evolve as experimental data become available, and biological theories and new experiments are performed as a result of computational insights.

Almost every conceivable category of molecules in biochemistry has been addressed by computational modeling and simulation, including proteins, carbohydrates, nucleic acids, and lipids.²³ Computational approaches have shed much light on a wide breadth of biochemical problems and dilemmas. Simulations can demonstrate how proteins fold, how one conformation dominates over another, or how a drug binds to its target.²⁴ It is now possible to simulate even larger structures, such as viruses,²⁵ ribosomes,²⁶ and other cellular organelles.

One such organelle is the cell membrane, which consists of an organized arrangement of phospholipids. Each lipid interacts with its neighbors in a non-covalent

fashion; the packing and consequent stress/strain created by these lipids ascribe to the membrane an overall structural integrity.²⁷ Yet, the membrane is by no means homogenous in composition; the type and concentrations of the lipids can vary, large macrocyclic molecules (such as cholesterol) can embed into the membrane, and peptides/proteins can also carve homes for themselves in this hydrophobic environment. Some of these proteins span across the entire membrane, while others only bind to one peripheral side.²⁸

Computational simulations of membranes began in the early 1980s, with the work of Berendsen *et al.*²⁹ Of course, these first models were primitive and consisted only of a few dozen lipids, accounting for a small patch of a cellular membrane. Nonetheless, the work was pivotal in that it was the first to accomplish the parameterization of lipids and allow for their simulation. As computing power and the field of molecular dynamics progressed, it soon became possible to simulate much larger patches of membranes.³⁰ During the 1990s, the work of Peter Tieleman *et al.* demonstrated that if simulated with careful attention to key parameters (including pressure and temperature coupling), a model membrane patch could mimic the physical properties of a real cell membrane (such as tension, area-per-lipid, etc).³¹

With confidence in the capability to simulate model membranes, scientists then turned their attention to membrane proteins. The first simulations of proteins in a lipid environment took place in the late 1990s, and the field of membrane-protein modeling has taken great leaps in the current decade. A wide variety of such systems has been examined, including the mechano-sensitive protein channels,³² ligand-gated ion channels and receptors,³³ anti-microbial peptides,³⁴ and G-protein coupled receptors.³⁵ In the work

presented here, the computational and pharmacological modeling of membrane proteins is further advanced.

The distribution of surface tension within a lipid bilayer, also referred to as the lateral pressure profile, has been the subject of theoretical scrutiny recently due to its potential to radically alter the function of biomedically-important membrane proteins. Experimental measurements of the pressure profile are still hard to come by, leaving first-principles all-atom calculations of the profile as an important investigative tool. Described and validated here (in Chapter 2) is an efficient implementation of pressure profile calculations in the molecular dynamics package NAMD, capable of distinguishing between internal, bonded and nonbonded contributions as well as those of selected atom groups. The new implementation can also be used in conjunction with Ewald summation for long-range electrostatics, improving the accuracy and reproducibility of the calculated profiles. Described are the results of the calculation of a pressure profile for a simple protein–lipid system consisting of melittin embedded in a model bilayer. While the lateral pressure in the protein–lipid system is nearly the same as that of the bilayer alone, partitioning of the lateral pressure by atom type revealed substantial perturbation of the pressure profile and surface tension in an asymmetric manner.

Next, in Chapter 3, Peptide insertion, positioning, and stabilization in a model membrane are probed via an all-atom molecular dynamics simulation. One peptide (WL5) is simulated in each leaflet of a solvated dimyristoylglycero-3-phosphate (DMPC) membrane. Within the first 5 ns, the peptides spontaneously insert into the membrane and then stabilize during the remaining 70 ns of simulation time. In both leaflets, the peptides localize to the membrane interface, and this localization is attributed to the

formation of peptide-lipid hydrogen bonds. It is shown here that the single tryptophan residue in each peptide contributes significantly to these hydrogen bonds; specifically, the nitrogen heteroatom of the indole ring plays a critical role. The tilt angles of the indole rings relative to the membrane normal in the upper and lower leaflets are approximately 26° and 54° , respectively. The tilt angles of the entire peptide chain are 62° and 74° . The membrane induces conformations of the peptide that are characteristic of β -sheets, and the peptide enhances the lipid ordering in the membrane. Finally, the diffusion rate of the peptides in the membrane plane is calculated (based on experimental peptide concentrations) to be approximately $6 \text{ \AA}^2/\text{ns}$, thus suggesting a 500 ns time scale for intermolecular interactions.

In Chapter 4, the free energy change of the same peptide (WL5) as it inserts into a model membrane is explored. This is an important phenomenon because a variety of biomolecules mediate physiological processes by inserting and reorganizing in cell membranes, and the thermodynamic forces responsible for their partitioning are of great interest. Recent experiments provided valuable data on the free energy changes associated with the transfer of individual amino acids from water to membrane. However, a complete picture of the pathways and the associated changes in energy of peptide insertion into a membrane remains elusive. To this end, computational techniques supplement the experimental data with atomic-level details and shed light on the energetics of insertion. In Chapter 4, the technique of umbrella sampling is employed in a total 850 ns of all-atom molecular dynamics simulations to study the free energy profile and the pathway of insertion of a model hexapeptide consisting of a tryptophan and five leucines (WL5). The computed free energy profile of the peptide as it travels from bulk

solvent through the membrane core exhibits two minima: a local minimum at the water-membrane interface or the head group region; and a global minimum at the hydrophobic-hydrophilic interface close to the lipid glycerol region. A rather small barrier of roughly 1 kcal mol⁻¹ exists at the membrane core, which is explained by the enhanced flexibility of the peptide when deeply-inserted. Combining these results with those in the literature, a thermodynamic model is presented for peptide insertion and aggregation which involves peptide aggregation upon contact with the membrane at the solvent-lipid head group interface.

Chapter 5 begins the examination of large and more biologically-relevant membrane proteins. The nicotinic acetylcholine receptor (nAChR), which is a member of the ligand-gated ion channel family, is implicated in many neurological events. Yet, the receptor is difficult to target without high-resolution structures. In contrast, the structure of the acetylcholine binding protein (AChBP) has been solved to high resolution, and it serves as a surrogate structure of the extra-cellular domain in nAChR. A virtual screening study of the AChBP is presented using the relaxed-complex method, which involves a combination of molecular dynamics simulations (to achieve receptor structures) and ligand docking. The library screened through comes from the National Cancer Institute, and its ligands show great potential for binding AChBP in various manners. These ligands mimic the known binders of AChBP; a significant subset docks well against all species of the protein and some distinguish between the various structures. These novel ligands could serve as potential pharmaceuticals in the AChBP/nAChR systems.

Finally, in Chapter 6, an analysis of Group IVA (GIVA) phospholipase A₂ (PLA₂) inhibitor binding is presented using a combination of deuterium exchange mass

spectrometry (DXMS) and molecular dynamics simulations. Models of the GIVA PLA₂ inhibitors pyrrophenone and the 2-oxoamide AX007 docked into the protein were designed based on deuterium exchange results, and extensive molecular dynamics simulations were run to determine protein-inhibitor contacts. The models show that both inhibitors interact with key residues that also exhibit changes in deuterium exchange upon inhibitor binding. Pyrrophenone is bound to the protein through numerous hydrophobic residues located distal from the active site, while the oxoamide is bound mainly through contacts near the active site. We also show changes in protein dynamics around the active site between the two inhibitor-bound complexes. This combination of computational and experimental methods is useful in defining more accurate inhibitor binding sites, and can be used in the generation of better inhibitors against GIVA PLA₂.

CHAPTER 2: Computational Investigation of Pressure Profiles in Lipid Bilayers with Embedded Proteins

2.1 Introduction

Lipid bilayers are the dominant structural component of cellular membranes. However, the diversity of lipids expressed in cells as well as their specific localization reflects their active role in determining the propensity of peptides to insert into bilayers, as well as the activity and function of integral membrane proteins. While protein–lipid interactions occur via a number of modes, including direct hydrogen bonding and specific interactions with the transmembrane portion of membrane proteins, the role of chemically non-specific lateral pressures has become increasingly well appreciated in recent years.

At equilibrium, cellular lipid bilayers are found in a tension-free state. Yet, the internal membrane lateral pressure, which stems from the interactions of membrane constituents, can vary significantly according to depth in the bilayer as well as the lipid composition.³⁶ This variation is attributable to a complex interplay of interactions between lipid components and the surrounding solvent, including the repulsion of the phosphate headgroups (a positive pressure), the hydrophobic–hydrophilic interface (a negative pressure) and the entropic repulsion of the hydrocarbon tails (a positive pressure).³⁷ The profile could be expected to be even more complex in the presence of transmembrane proteins, which make up a significant portion of many lipid bilayers in vivo.

While some progress has been made in directly measuring the lateral pressures in bilayers,³⁸ computational approaches are still an important tool for investigating the nature of the pressure distributions and their dependence on membrane composition. Both statistical models,³⁷ coarse-grained molecular dynamics (MD),^{39,40} and all-atom MD^{41,32} have been used to directly calculate the lateral pressure from the underlying molecular interactions. The MD approach, while much more computationally intensive than more coarse-grained approaches, benefits from the decades-long development of transferable force fields as well as the ability to model specific lipid headgroups and protein inclusions in atomic detail. An all-atom approach thus presents the opportunity to develop a consistent model of both specific, chemical interactions between lipids and proteins, as well as non-specific, physical effects such as those arising from inhomogeneous distributions of, and shifts in, lateral pressures.

Recent experimental results seem to suggest that, while specific lateral pressure profiles play a role in modulating membrane protein behavior in some cases, specific lipid–protein interactions are still critical for function. An illustrative example is the interaction of the nicotinic acetylcholine receptor (nAChR) with its surrounding lipid environment. Solid-state NMR measurements suggest a strong interaction between the $\alpha 1$ segment of nAChR and dimyristoylphosphatidylcholine (DMPC) bilayers, leading to effects on lipid organization that cannot be explained solely by hydrophobic mismatch or bilayer rigidity.⁴² Contrary to physical mechanisms of membrane protein control, it was found by Martinez *et al.* that nAChR exhibits binding kinetics in a complex of amphipathic polymers similar to that of its native membrane environment.⁴³ However, in detergent, the kinetic properties of the channel are markedly different. The authors argue

that the data supports a molecular mechanism of channel function modulation, rather than a generic, physical mechanism. Baenzinger *et al.* find mixed results: either dioleoylphosphatidic acid (DOPA) or cholesterol in a reconstituted egg phosphatidylcholine membrane can influence the equilibrium between nAChR states, but anionic lipids are required for nAChR to adopt a fully functional conformation.⁴⁴

The present work seeks to extend lateral pressure calculations to protein–lipid systems. For comparison with previous work we chose to model a well-studied peptide, melittin, which forms stable helices and aggregates in bilayers. Pressure profiles for membrane proteins have been studied previously,^{45,46} to our knowledge no protein–lipid systems have been studied in this manner using all-atom MD. The effect of lateral pressures on a system as simple as a single helical peptide ought to be discernable in simulation, as thermodynamic transfer energies for insertion of helices of varying composition have been shown to depend on the location of residues within the polypeptide chain.⁴⁷

Consisting of 26 amino acids, melittin embeds itself in cellular membranes, disrupts their integrity and eventually leads to lysis. The mechanism of such embedment as well as the orientation of melittin in the lipid bilayer are the subjects of much research. It has long been suggested that melittin can lie either laterally across the membrane or insert itself parallel to the lipid normal, with the hydrophilic carboxy terminus protruding out of the membrane.⁴⁸ A computational study of the former orientation demonstrating its stability has been presented.⁴⁹

The present article introduces preliminary findings of a computational study of the latter orientation of melittin (parallel to the normal) in a lipid bilayer. In particular, we

seek to calculate the lateral pressure profile of a DMPC bilayer hosting melittin in the normal-parallel orientation and to contrast this to a profile of the membrane without melittin. The objective is to demonstrate a significant difference between the pressure profiles of the membrane-protein and no-protein complexes. If such a difference exists, one can then study the effect of the protein-altered pressure profile on other constituents (possibly other proteins) in the membrane.

2.2 Materials and Methods

The DMPC system was based on a pre-equilibrated membrane from the Tieleman laboratory (<http://www.ucalgary.ca/tieleman/download.html>). The melittin coordinates used were those of 2MLT.pdb, downloaded from the Protein Data Bank.⁵⁰ The DMPC membrane originally contained 128 lipids (divided evenly between the top and bottom monolayers), was solvated with 3655 water molecules and previously equilibrated for 1 ns at a constant area of 0.596 nm²/lipid. The membrane normal was oriented with the z-axis.

Using the Visual Molecular Dynamics program⁵¹ and in a manner similar to that of Bachar *et al.*,⁵² three DMPC residues near the center of the membrane were deleted from the bottom monolayer, as well as four from the top monolayer. The melittin structure, stripped of its sulfate ions, was carefully placed along the z-axis in this cavity; see Figure 1. After neutralization, this new system, which we refer to as DMPC+Mel, consisted of 121 DMPC lipids (61 in the bottom monolayer, 60 in the top), the 26-residue melittin, five chloride ions and 3637 TIP3 water molecules for a total of 25,625 atoms.

Following a 5 ps equilibration period, pressure profile data was gathered under conditions identical to equilibration from runs of 14.3 ns for the DMPC system and 22.08 ns for the DMPC+Mel system.

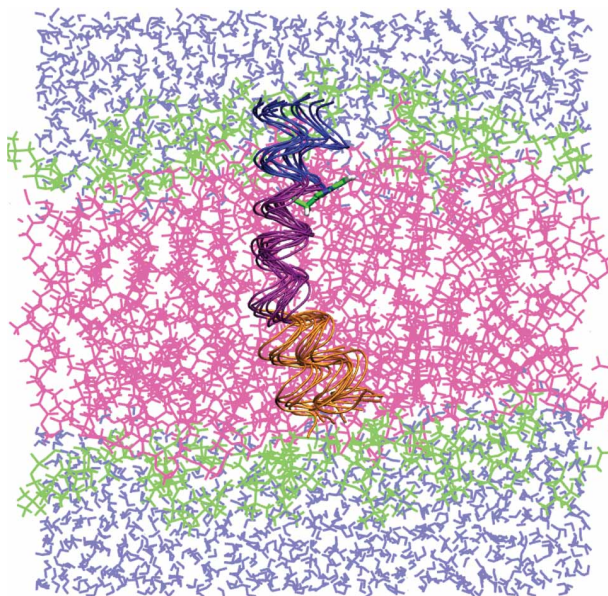


Figure 1: Initial snapshot of melittin-DMPC system, colored by atom type used in the pressure profile analysis: lipid headgroups (green), lipid tails (pink), water (light blue), Melittin residues 1–11 (orange), 12–20 (purple), and 21–26 (dark blue). Melittin conformations are shown from snapshots separated by 2 ns. See online version for color.

The molecular dynamics program NAMD⁵³ with the CHARMM27 force field⁵⁴ was employed for all MD simulations and calculations. Following the procedure of Berneche *et al.*,⁴⁹ the system was equilibrated at 330 K, with temperature control provided by Langevin dynamics with a coupling constant of 2 ps, and pressure control via the Langevin piston method.⁵⁵ The cross-sectional area of the membrane was held fixed at 59.4 by 63.0 Å, while the pressure normal to the bilayer was maintained at 1 atm. Bonds to hydrogens were fixed, permitting a timestep of 2 fs. Nonbonded interactions were smoothly switched off between 9 and 10 Å. Long-range electrostatic forces were

evaluated using the particle mesh Ewald (PME) method⁵⁶ with grid spacing less than 1 Å along each axis.

The pressure profile was further partitioned by atom type (see below). The partition for the melittin system is shown in Figure 1. Besides lipid and solvent atoms, we partitioned the melittin peptide into three segments, which we refer to as Mel (1–11), Mel (12–20), and Mel (21–26), corresponding to the residues included in each partition.

The bulk pressure P is expressed in terms of the contributions made by kinetic and inter-particle interactions as:

$$\mathbf{P} = \frac{1}{\Delta V} \left[\sum_i m_i \mathbf{v}_i \otimes \mathbf{v}_i - \sum_{ij} F_{ij} \otimes \mathbf{r}_{ij} \right] \quad (1)$$

where ΔV is the change in volume, m_i and \mathbf{v}_i are the mass and velocity of the i^{th} -particle, F_{ij} and r_{ij} are the interaction force and distance between particles i and j . Calculation of the lateral pressure profile requires partitioning into several different spatial regions. At equilibrium the off-diagonal elements of pressure vanish, and in a homogeneous system such as bulk solvent the diagonal components will be equal. Anisotropic systems such as lipid bilayers may maintain a non-vanishing surface tension (γ), given by:

$$\gamma = \int_{-h/2}^{h/2} dz \left[P_{zz} - \frac{1}{2} (P_{xx} + P_{yy}) \right] \quad (2)$$

where $2h$ is the total bilayer thickness (with the membrane center placed at 0), and the latter quantity in the integrand is the lateral pressure.⁴¹ The integration takes place over the entire simulation space.

We consider here systems with anisotropy only along one axis, which we assign to z , so that the system may be partitioned into “slabs” perpendicular to the z -axis.

Calculation of the spatial distribution of the lateral pressure requires that the contributions to the virial be somehow distributed over the several slabs. A natural choice of contour, employed by several previous efforts,^{41,45} is the Irving–Kirkwood contour,⁵⁷ in which the contribution from each interaction is distributed evenly between slabs lying on a straight line between the interacting particles. It has been pointed out, however, that this approach is limited to describing pairwise interactions, which precludes the use of common electrostatics methods such as PME in the computation of the pressure profile.⁵⁸ PME can be reasonably well approximated using long cutoffs, but artifacts may still remain due to the non-uniform distribution of charges in the plane of the bilayer and the slow convergence of the distribution of lipids.

Using a different contour, known as the Harasima contour,⁵⁹ full electrostatics can readily be employed in the pressure profile calculation by using Ewald sums.⁵⁸ At sufficiently high accuracies, the Ewald sum and the particle mesh ewald computation converge to precisely the same result. PME has the advantage of converging faster and producing smooth forces, which are required for MD simulation.

For the purpose of determining the contributions of water, lipid, protein, or other classifications of atom types to the pressure profile, we also computed pressure profiles decomposed by atom type. Following the notation of Essman *et al.*,⁵⁶ the reciprocal space contribution to the electrostatic energy E_{rec} of a configuration of N charged particles with coordinates r_i is given by:

$$E_{rec} = \frac{1}{2\pi V} \sum_{m \neq 0} \frac{\exp(-\pi^2 m^2 / \beta^2)}{m^2} S(m)S(-m) \quad (3)$$

where the structure factor $S(m)$ is given by:

$$S(\mathbf{m}) = \sum_{j=1}^N q_j \exp(2\pi i \mathbf{m} \cdot \mathbf{r}_j) \quad (4)$$

and the reciprocal lattice vectors $\mathbf{m} = m_1 \mathbf{a} + m_2 \mathbf{b} + m_3 \mathbf{c}$, where \mathbf{a} , \mathbf{b} , \mathbf{c} designate the reciprocal unit vectors, and for integers m_1 , m_2 , and m_3 not all zero. For the purpose of obtaining a pressure profile, one simply expands one of the structure factor terms in equation (4) and rearranges the order of summation to obtain the contribution of the pressure provided by each individual atom:

$$\mathbf{V} \prod_{\text{rec } \alpha\beta}^i = \frac{q_i}{2\pi\mathbf{V}} \sum_{\mathbf{m} \neq 0} f_{\alpha\beta}(\mathbf{m}) \text{Re} [\exp(-i \mathbf{m} \cdot \mathbf{r}_j) S(\mathbf{m})] \quad (5)$$

where we have defined:

$$f_{\alpha\beta}(\mathbf{m}) \equiv \frac{\exp(-\pi^2 \mathbf{m}^2 / \beta^2)}{\mathbf{m}^2} \times \left(\delta_{\alpha\beta} - 2 \frac{1 + \pi^2 \mathbf{m}^2 / \beta^2}{\mathbf{m}^2} m_\alpha m_\beta \right) \quad (6)$$

where α and β are the unit cell vector and conjugate vectors (respectively), and $\delta_{\alpha\beta}$ is the Kronecker delta (if $\alpha = \beta$, $\delta_{\alpha\beta} = 1$, otherwise $\delta_{\alpha\beta} = 0$).

The particle mesh Ewald method proceeds by interpolating the structure factor onto a grid. Although it seems that the pressure profile could in principle be determined directly from the PME approximation to the structure factor, such an expression is much more unwieldy than the direct Ewald sum. Moreover, since (as described below) the Ewald contribution may be calculated offline, and plays no role in the simulation dynamics, the calculation of the Ewald contribution need not be as fast as PME.

The Ewald sum also admits a partition into contributions from selected atom types. If the structure factor equation (4) is decomposed into k partitions $S_1(\mathbf{m}) + S_2(\mathbf{m}) + \dots + S_k(\mathbf{m})$, then, from equation (3), the reciprocal energy can be written:

$$E_{\text{rec}} = \sum_{s=1}^k E_{\text{rec},s} + \sum_{s \neq t} \sum_{m \neq 0} \frac{\exp(-\pi^2 m^2 / \beta^2)}{m^2} S_s(m) S_t(-m) \quad (7)$$

where E_s is the reciprocal space energy if only particles of type s are considered. The remaining cross terms can be considered to arise from the interactions between particles of type s and t , and can themselves be partially-partitioned just as was done for interactions between atoms of the same type.

In the new NAMD implementation, all contributions to the pressure profile except the Ewald sum are computed “online”; that is, as the simulation proceeds. For each pressure profile slab, the module outputs the average of the pressure tensor for all timesteps since the previous output. This self-averaging improves the convergence of the nonbonded contribution to the pressure profile and avoids problems associated with using multiple timestepping.³² In addition to the total pressure profile, the contributions from “internal”, “bonded”, and “nonbonded” are output separately. “Internal” incorporates contributions from the kinetic energy of the particles, as well as correction forces arising from rigid bond constraints. The “bonded” portion contains the usual covalent terms present in the force field, while “nonbonded” contains all van der Waals and electrostatic interactions.

If multiple atom types have been specified, all three contributions to the pressure profile are further subdivided by atom type. One set of “internal” contributions are reported for each atom type. For “bonded” and “nonbonded”, the self interactions of each atom type with other atoms of the same type, as well as the pairwise interactions of each atom type with every other atom type, are recorded. In the current implementation, up to 15 different atom types can in principle be analyzed simultaneously.

If a simulation was conducted using PME for electrostatics, a second offline calculation needs to be made to account for the reciprocal space contribution to the pressure. In the previous implementation (present in NAMD 2.5), this could be done only by setting a long cutoff. In the new implementation, the PME contribution can be estimated using a cutoff as before (by ignoring the nonbonded contribution in the online calculation and re-computing the nonbonded contribution using a long cutoff), or with the Ewald summation method.

The calculations presented here all used the Ewald sum for the calculation of the pressure profile. The maximum Ewald k-vector along each direction was sixteen; no significant improvement was observed when more k-vectors were added.

2.3 Results

The distribution of melittin residues within the DMPC bilayer is shown in Figure 2a. While the N-terminal half of the peptide lies entirely within the hydrophobic core of the bilayer, much of the C-terminal region resides in the solvent-headgroup interface region. That this region (and specifically residue 19, tryptophan) remains in the interface during the entire simulation agrees well with previous experimental and simulation results.^{52,60} A small kink in the helix is reflected in a change in slope of the melittin residue distribution at GLY12. This kink, as well as the overall disposition of the melittin within the bilayer, remained fairly constant for the duration of the simulation. Such observations are characteristic of melittin-membrane simulations.⁵²

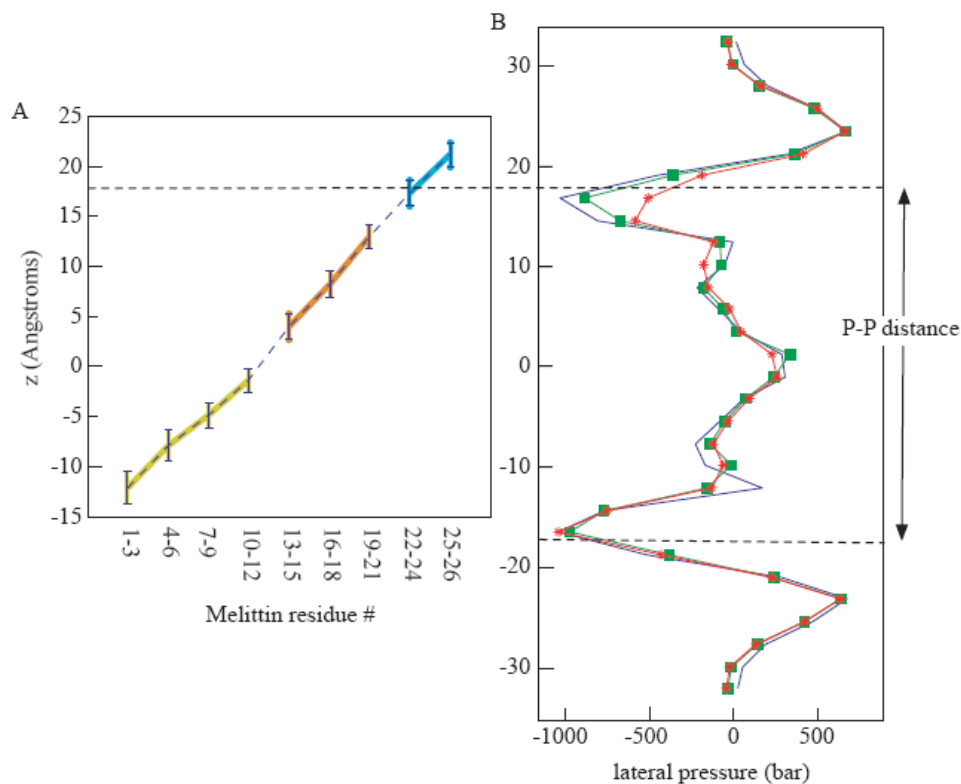


Figure 2: a) Distribution of melittin residues within the bilayer. b) Lateral pressure profile computed from DMPC-only simulation (DMPC, blue), DMPC with melittin (DMPC+Mel, green), and DMPC with melittin but excluding the contribution of melittin interactions (DMPC+ExcMel, red) in online version.

We computed lateral pressure profiles for both the DMPC and DMPC+Mel systems. For purposes of comparison, we also computed the pressure profile for the DMPC+Mel system with the contributions from melittin atoms excluded from the sum. We refer to this “virtual” system as DMPC+ExcMel. The lateral pressure profiles computed from the DMPC, DMPC+Mel and DMPC+ExcMel simulation are shown in Figure 2b. As in previous work,³² the peak tension, corresponding to minimum lateral pressure, lies just inside the average depth of the phosphate groups of the bilayer. In both simulations the profile is reasonably symmetric, and drops to zero in the water phase, indicating that the bilayer is sufficiently hydrated.

While the total pressure profile in the DMPC and DMPC+Mel simulations appears very similar, the contribution to the lateral pressure made by the lipid alone is substantially offset in the upper monolayer by the contribution made by the melittin. Only a small change in the profile of the DMPC+Mel simulation compared to the pure DMPC simulation is observed in the lower leaflets. As seen in Table 1, the total tension in the membrane is nearly the same in the two systems, differing by less than the statistical error in their measurement. Although the area per lipid and lipid order parameter (Figure 4) in our simulations are in good agreement with experimental membrane values,⁶¹ the system still exhibits positive surface tension. This is in agreement with previous work employing the CHARMM parameter set for lipids,⁶² where it was found that a surface tension of 35 – 45 dyne cm⁻¹ gave the best agreement with known area per lipid. Our smaller tensions in the range of 10 – 20 dyne cm⁻¹ probably derive from the larger size of the bilayers in our simulations (60 lipids per monolayer, compared to 36 in reference 62).

Table 1: Per-monolayer tension computed, respectively, from total virial during the simulations, from the pressure profile, and from the pressure profile for the lower and upper leaflets separately. All units are in dyne cm⁻¹. See the caption of Figure 2 for definitions of abbreviations.

	<i>Pressure Tensor</i>	<i>Pressure Profile</i>	<i>Lower Leaflet</i>	<i>Upper Leaflet</i>
DMPC	12.2 ± 1.4	12.7	12.9	12.6
DMPC+Mel	13.2 ± 1.1	13.3	18.0	8.5
DMPC+ExcMel	N/A	8.0	19.2	3.2

The tension computed from the pressure profile analysis will necessarily differ slightly from the tension computed on the fly during the respective simulations, simply because it is based in part upon post-processing of trajectory timesteps sampled 500 ps

apart. As seen in Table 1, the tensions computed from the pressure profiles are both well within the statistical error of the direct simulation values. However, the pressure profile analysis also reveals that the tensions in the individual monolayers are nearly the same in the DMPC simulation, but differ substantially in the DMPC+Mel simulation. The tension in the lower leaflet is nearly 5 dyne cm^{-1} larger than in pure DMPC, and 4 dyne cm^{-1} smaller in the upper leaflet. This is despite the fact that, in the construction of the DMPC+Mel system, the upper leaflet has fewer lipids than the lower leaflet (60 vs. 61, respectively); thus, if the two termini of melittin were perfectly symmetric, one would expect that the upper leaflet would exhibit greater tension due to its increased area per lipid. In fact, the opposite is observed, suggesting that protein–lipid interactions are the primary mechanism responsible for decreasing the tension in the upper leaflet and increasing the tension in the lower leaflet.

The asymmetry in the tension is even more striking when melittin interactions are excluded from the calculation. Values in the third line of Table 1 are computed for contributions to the pressure profile from lipid, water, and interactions between lipid and water. The average tension in the DMPC+Mel system when melittin is excluded is only 8 dyne cm^{-1} , compared to $13.3 \text{ dyne cm}^{-1}$ for the complete system. Yet, the computed tension in the lower leaflet is even greater than in the complete DMPC+Mel system, $19.2 \text{ vs. } 18 \text{ dyne cm}^{-1}$, while the tension in the upper leaflet is much smaller, $3.2 \text{ vs. } 8.5 \text{ dyne cm}^{-1}$.

Despite the large difference in tension between the two leaflets, the available area per lipid is not substantially different, and thus, as shown Figure 4a, the lipid order parameter in the two leaflets is virtually indistinguishable. This similarity in order

parameter between the two leaflets has also been noted in previous membrane-melittin simulations.⁵²

As shown qualitatively in Figure 1, and quantitatively in Figure 2a, the melittin peptide was quite stable during the course of the DMPC+Mel simulation in terms of its secondary structure, its orientation relative to the bilayer normal and its depth in the bilayer. We therefore consider the spatial regions within the bilayer where the components of the melittin peptide contributed to the lateral pressure.

Figure 3a shows the partial lateral pressures arising from interactions involving three subsections of the melittin peptide; residues 1–11, referred to as Mel(1–11); residues 12–20, Mel(12–20); and residues 21–26, Mel(21–26). It is somewhat surprising that interactions due to the respective components of melittin were visible well outside the spatial region occupied by those components. In order to establish whether those interactions were due in part to the use of periodic boundary conditions in the simulation along the z direction, a second DMPC+Mel system was constructed with a water layer 20 Å thicker than the one described here. No significant difference was seen in the location or size of the peaks in the pressure profile, indicating that the pressure profile peaks visible in Figure 3 are due to interactions within the membrane and not from interactions with neighboring periodic images.

The most pronounced contribution from the melittin to the pressure profile occurs around $z = 18 \text{ \AA}$, with a large negative peak. This is, of course, consistent with the result of Figure 2, where it was shown that excluding the contribution of melittin to the pressure profile leads to an increase in lateral pressure in the region around $z = 18 \text{ \AA}$.

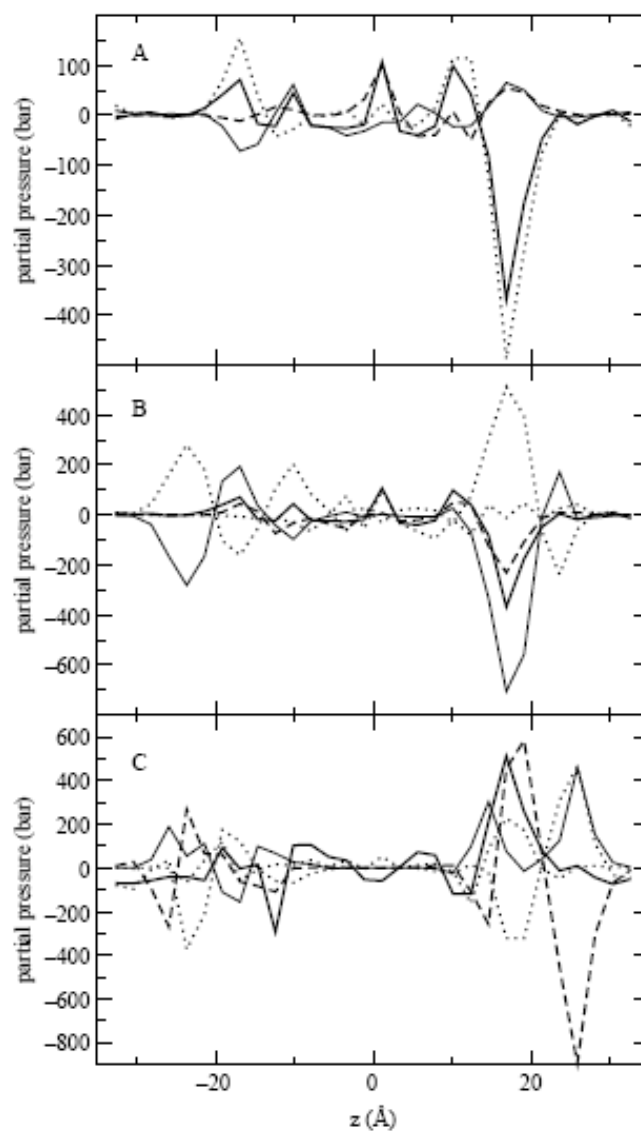


Figure 3: a) Partial pressures of melittin: contribution from complete protein(thick solid line); melittin residues 1–11(thin solid line); residues 12–20(dashed line); residues 21–26(dotted line). b) Partial pressures arising from interactions of melittin with other simulation components. Thick solid line: total melittin pressure; thin solid line: interactions with lipid headgroups; dashed line: interactions with lipid tails; dotted line: interactions with water; dot-dashed line: interaction with self. c) Difference between pressure profile components in DMPC+melittin simulation and pure DMPC simulation. Thick solid line: total difference in membrane and water contribution to the pressure profile; thin solid line: headgroup–headgroup interactions; dashed line: headgroup–water interactions; dotted line: tail–water interactions; dot-dashed line: water–water interactions.

Most of this peak is due to Mel(21–26), which, with its four positively charged side chains near the highly polar lipid headgroups, is well positioned to interact strongly with the bilayer. The other two melittin segments studied here slightly offset the contribution of Mel(21–26) in this region.

Figure 3b shows the same total pressure arising from melittin interactions as in Figure 3a, but instead partitioned by interaction partner rather than by melittin component. A great deal of cancellation between interacting terms is seen, especially between water and headgroups. In particular, melittin gives rise to zero net partial pressures in the region near $z = \pm 25 \text{ \AA}$ due to the cancellation of interactions involving water and lipid headgroups. We can observe that the small peaks at $z = -18 \text{ \AA}$ and $z = -2 \text{ \AA}$ are due to melittin interactions with the lipid tails. Water and headgroup interactions together provide about half the contribution to the large negative peak at $z = 18 \text{ \AA}$, with the rest provided by melittin–tail interactions and a small cancellation due to protein–protein forces.

Figure 3c shows how the partial pressures of membrane and water components in DMPC changed upon insertion of melittin. We observe an increase in lateral pressure at $z = 18 \text{ \AA}$ where the bilayer and solvent interact with the charged residues in Mel(21–26), and also a small decrease in lateral pressure around $z = -16 \text{ \AA}$. Most strikingly, we see very little change in the solvent region near the upper leaflet due to near perfect cancellation of the change in contribution from headgroup–water interactions with those from headgroup–headgroup and water–water interactions. While headgroup–water interactions are the dominant contributor of surface tension in both simulations, they make a stronger contribution in the presence of melittin; however, headgroup–headgroup

and water–water interactions still offset headgroup–water interactions just enough to give nearly zero net change in the tension in the solvent region.

Figure 4b and 4c shows the number of hydrogen bonds made by Mel(12–20) and Mel(21–26) with surrounding phosphate groups and water molecules. Mel(1–11), being deeply buried in the hydrophobic portion of the bilayer (Figure 2), made very few hydrogen bonds. Mel(12–20) was found to be hydrogen bonded to phosphate in 5.6 % of simulation snapshots, compared to 82% for Mel(21–26). Similarly, Mel(12–20) formed at least one hydrogen bond with water 35% of the time, compared to 91% for Mel(21–26). The difference is, of course, reflected in the proximity of Mel(21–26) to the interface as well as the large number of charged side chains present in Mel(21–26), as compared to Mel(12–20).

2.4 Discussion

The importance of proteins, small molecules, and other non-lipid components in modulating the hydrophobic environment of lipid bilayers is becoming increasingly well-recognized, in part due to recent contributions of molecular simulations. Pressure profile studies of lipids with varying amounts of cholesterol revealed a surprisingly complex pattern of pressure peaks and troughs that varied with cholesterol concentration.⁴⁶ Simulations of DPPC over a range of lipid areas (50 – 80 Å² per lipid) showed that the tension in the bilayer could be lowered upon addition of trehalose, which is known to stabilize lipid bilayers,⁶³ providing a possible mechanism for the stabilization. Here, we analyzed the lateral pressure of a DMPC bilayer both with and without a melittin peptide,

under conditions of nearly identical total surface tension. We find that a single melittin significantly lowers the tension of the lipids surrounding the peptide.

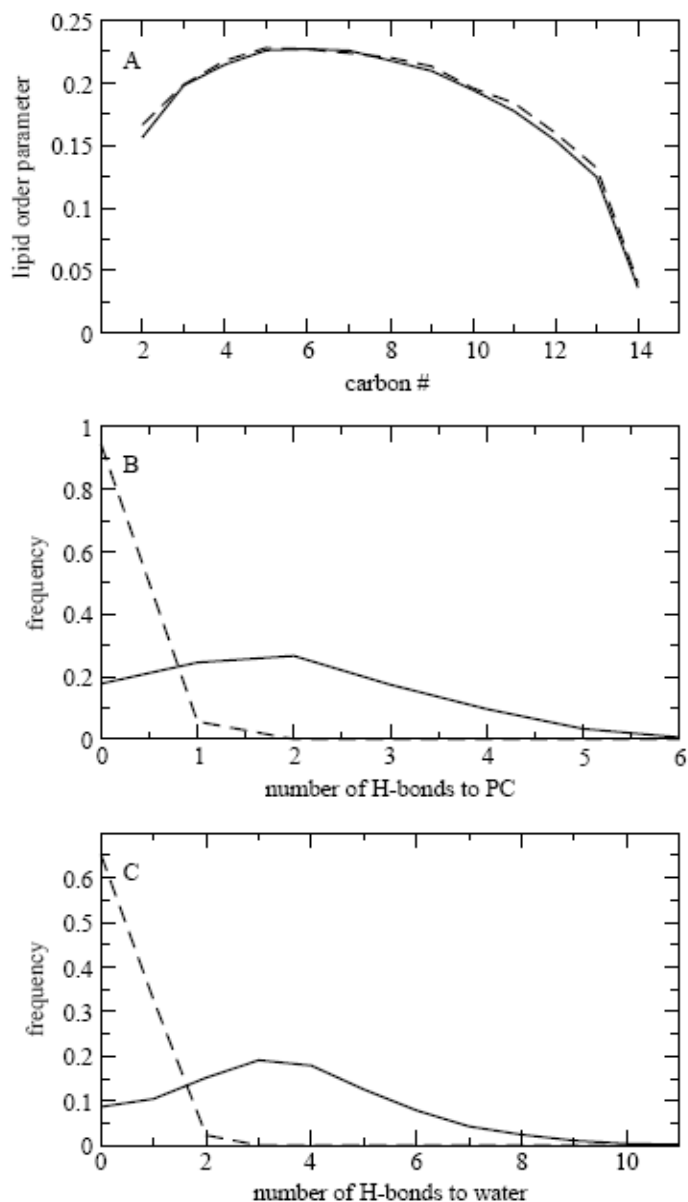


Figure 4: Protein-lipid interactions in DMPC+melittin system. a) Averaged lipid order parameters of the lower (solid line) and upper (dashed line) leaflets. b) Fraction of simulation snapshots containing the indicated number of hydrogen bonds with phosphate oxygens for melittin residues 12–20 (dashed line) and 21–26 (solid line). c) Same as b), but for hydrogen bonds to water.

The two leaflets of the bilayer exhibit the same surface tension in the peptide-free system, but markedly different tensions when melittin is inserted. The tension in the leaflet containing the amino terminus of the melittin increased by 50% upon melittin insertion, while in the carboxyl terminus the tension decreased by nearly the same amount.

The present work demonstrates that protein–lipid interactions contribute significantly to the total bilayer tension in the vicinity of an inclusion. Additional investigation under conditions of constant surface tension and/or variable lipid number will be required in order to determine how lateral pressure figures into other modes of protein–lipid interaction, such as the electrostatic potential, in modulating the propensity of peptides to insert into bilayers as well as the equilibrium between conformations of peptide aggregates and integral membrane proteins.

2.5 Acknowledgements

This work was supported in part by the National Science Foundation, the National Institutes of Health (GM34921), the Howard Hughes Medical Institute, the National Biomedical Computing Resource, Accelrys, the Keck Foundation, and the Center for Theoretical and Biological Physics.

Chapter 2, in full, is a near reprint of the material as it appears in *Molecular Simulation* 2006, Volume 32, Pages 831-838. This is a co-authored article. The dissertation author and J. Gullingsrud were the primary co-contributors to this work. J. A. McCammon served as the head adviser and principal investigator.

CHAPTER 3: Peptide Insertion, Positioning, and Stabilization in a Membrane: Insight from an All-Atom Molecular Dynamics Simulation

3.1 Introduction

A wide range of functions, such as proton transport and cell signaling, illustrate the importance of transmembrane proteins in biological phenomena. Consequently, elucidating the chemical and biochemical behavior of these proteins is the subject of much research. For example, extensive spectroscopic techniques have been used to probe the relationship between the structure and function of transmembrane proteins.⁶⁴ Properties such as helix tilt angles, side chain orientations, and functional conformations have been studied in a variety of transmembrane proteins using NMR and Raman spectroscopy.^{65,66,67} Tryptophan fluorescence and circular dichroism techniques have also been used to study the equilibrium penetration depth of small transmembrane peptides.⁶⁸

Computational methods—including implicit membrane models, coarse-grained, and all-atom molecular dynamics (MD) simulations—have complemented experimental techniques. In the implicit membrane approach, the membrane is represented by an electrostatic continuum (such as the Generalized Born model) while the protein is treated explicitly.⁶⁹ This technique reduces the computational time required to model protein-membrane phenomena but does so at the expense of relevant details regarding the membrane. In coarse-grained modeling, two or more atoms can be merged to form a

single bead; for instance, all of the phosphate atoms of a lipid head group can be represented by one bead, while the choline group atoms by a second bead.^{70,71,72} This approach strives to employ the simplest possible description of its system components, in order to gain specific physical insight, such as the conformational dynamics of a channel transmembrane protein.⁷³ As a result, coarse-grained modeling can provide insight on reactions that occur on relatively long biological time scales.

In contrast to implicit and coarse-grained modeling approaches, the all-atom MD method—in which nearly every atom is treated explicitly—can employ broadly transferable and accurate force fields describing the interactions between lipid, protein, and water. As an example, Aliste *et al.* employed all-atom MD simulations to study the thermodynamics of small peptides at a membrane-solvent interface.⁷⁴ In this study, the authors attempted to reproduce the Wimley-White scale⁷⁵ which provides the free energy associated with the transfer of a residue from the solvent to the membrane. Although they were not completely successful in this endeavor, Aliste *et al.* successfully elucidated the energetic differences for peptide-partitioning into a non-polar solvent or a membrane. They also demonstrated that the penetration depth of the peptide into a membrane is a function of the peptide hydrophobicity.

Protein insertion and positioning in a membrane host are of particular interest in transmembrane peptides. As experimental approaches continue to expand in this area,^{76,77} computational approaches are also being utilized to reveal the details of protein insertion and positioning. Gorfe *et al.* used all-atom MD to study the insertion and stabilization of a lipidated peptide.⁷⁸ In their simulations, the authors applied an artificial force on the lipidated peptide to induce the insertion process. Once inserted, the applied force was

turned off, and the lipidated peptide was allowed to stabilize. This non-equilibrium approach—also known as steered molecular dynamics (SMD)—was used to enhance the rate of insertion. This technique is valid as long as the applied force does not significantly perturb the physical properties of the model membrane during the simulation.⁷⁹ If the thickness, order parameters, or cross-sectional area of the membrane are dramatically altered as the peptide inserts into the membrane, the SMD simulation is considered unrealistic. For this reason, care must be taken in selecting the magnitude of the pulling force. In addition to utilizing realistic forces, an equilibrium, all-atom MD simulation of biomolecular insertion into a membrane is challenging because of the time scale; protein insertion requires μs to ms simulations, which are currently inaccessible by all-atom MD.⁸⁰

In this study, we present an equilibrium all-atom MD simulation—with no biasing force—of a solvated peptide membrane system. The peptide used is WL5 and consists of one tryptophan (TRP) residue followed by five leucines. It is acetylated and amidated at its N- and C-termini, respectively. The membrane of choice is a 1,2-dimyristoylglycero-3-phosphocholine (DMPC) bilayer. We chose this small peptide in hopes of observing its spontaneous insertion into the membrane during an equilibrium MD study. The available experimental work on this system shows that multiple units of WL5 assemble in the membrane to form a multimeric anti-parallel β -sheet.^{81,82,83} While the experimental data will help validate the simulation results presented here, the latter will provide important atomic-level details and hence shed additional light on the phenomena of peptide insertion, positioning, and stabilization in the membrane host.

3.2 Materials and Methods

A single WL5 peptide was assembled in an extended conformation using SYBYL.⁸⁴ Using the GROMACS MD package,¹⁹ the peptide was placed by itself in a 25 nm³ cubic box and solvated with 4092 water molecules. The peptide was held fixed in position and the water molecules were energetically minimized. This minimization scheme consisted of 2500 steps of steepest descent followed by 2500 steps of conjugate gradient minimization. The peptide was then liberated and the entire free system was again minimized by the same scheme. While restraining the heavy atoms of the peptide (with a force constant of 1000 kJ mol⁻¹nm⁻¹), the system was heated to a temperature of 310K over 50 ps. Pressure coupling was then included, the restraints were lifted, and the free system of peptide in water was equilibrated for 5 ns. The last snapshot of the peptide (still in its extended form) was used as the starting conformation in the membrane/peptide simulation. A pre-equilibrated, 128-lipid DMPC membrane was obtained from the Tieleman laboratory.^{74,85} To ensure the integrity of the membrane, it was further equilibrated in solvent for 10 ns. No appreciable change in the membrane thickness, order parameters, or area per lipid occurred (data not shown).

Using VMD,⁵¹ one copy of the equilibrated peptide was situated on either side of the equilibrated bilayer, at an average distance of 10 Å from the nearest lipid head groups. The principal axis of the peptide was oriented parallel to the membrane plane, which was set to be the xy-plane. Using GROMACS, the system was placed in a box of dimensions 6.02 × 6.02 × 9.50 nm and then solvated with 6631 water molecules. The peptides and membrane were held fixed in position, while the water molecules were

minimized via 2500 steps of steepest descent then 2500 steps of conjugate gradient minimization. The peptides and membrane were then liberated, and this entire free system was again minimized by the same scheme. The heavy atoms of the peptides and membrane were then restrained in position (force constant of $1000 \text{ kJ mol}^{-1} \text{ nm}^{-1}$), while the solvent was heated to 310K, over 50 ps. Finally, all restraints were removed, and the all-atom MD simulation (25,925 atoms) was conducted for a total of 75 ns.

The GROMOS (ffgmx) force field parameters were used for the peptides and solvent, while the lipid parameters provided by Berger *et al.*⁸⁶ were employed for the DMPC lipids. A time step of 2 fs and a non-bonded cutoff of 1.0 nm (for van der Waals interactions) were used. Full electrostatics were calculated using the particle mesh Ewald (PME) method, with 6th order spline interpolation and a tolerance of 1×10^{-5} .^{87,56} Berendsen temperature coupling was employed,⁸⁸ with a reference temperature of 310K and a coupling of 0.1 ps. For the production run, a semi-isotropic pressure coupling scheme was used, with a reference pressure of 1.0 bar, a pressure coupling of 0.5 ps, and a compressibility of $4.5 \times 10^{-5} \text{ bar}^{-1}$. Trajectories were analyzed using the various GROMACS tools. Rendering and visualization were done in VMD. Plots and figures were created in MATLAB©.⁸⁹

3.3 Results and Discussion

During the first 5 ns of the production run, the peptide on either side of the membrane diffuses throughout the simulation box and associates with the membrane. The peptides then spend the remaining 70 ns of simulation time stabilizing in the membrane

host (see Figure 5), consistent with the known thermodynamics of the system. The solute (peptide) is very hydrophobic and initially resides in a polar solvent. The head group region of the membrane is less polar,⁹⁰ and the local dielectric constant of the membrane core varies between 2 and 5.^{91,92} Thus, as expected, the membrane serves as a thermodynamically favorable environment for the model peptide. Despite changes in their conformation and lateral positions, the peptides remain in the membrane for the duration of the simulation (as discussed below).

Shown in Figure 6 are the penetration depths of the peptides in each leaflet of the membrane. When averaged over 50 ps blocks during the last half of the simulation, the penetration depth of the peptide into the upper leaflet is 2.70 ± 1.05 Å. The corresponding depth in the lower leaflet is 1.26 ± 1.47 Å. The peptide in the upper leaflet resulted in a slightly more convergent result. The penetration depths in both leaflets are in agreement with each other, consistent with the symmetrical nature of the system. This observed penetration demonstrates the spontaneous insertion of the peptides, without the need for an external biasing force.

A noteworthy observation is that despite their hydrophobic nature, the peptides do not completely submerge into the membrane core. On our time scale, they stabilize at the membrane interface—a region defined to contain the first solvation layers, the lipid head groups, and the beginning of the lipid tails. This interfacial localization of the peptides can be ascribed to the tryptophan residue, as noted previously.⁹³ Yau *et al.* observe that the role of TRP in anchoring proteins to the interfacial region of membranes can be attributed to the physical characteristics of the indole side chain. Relevant characteristics

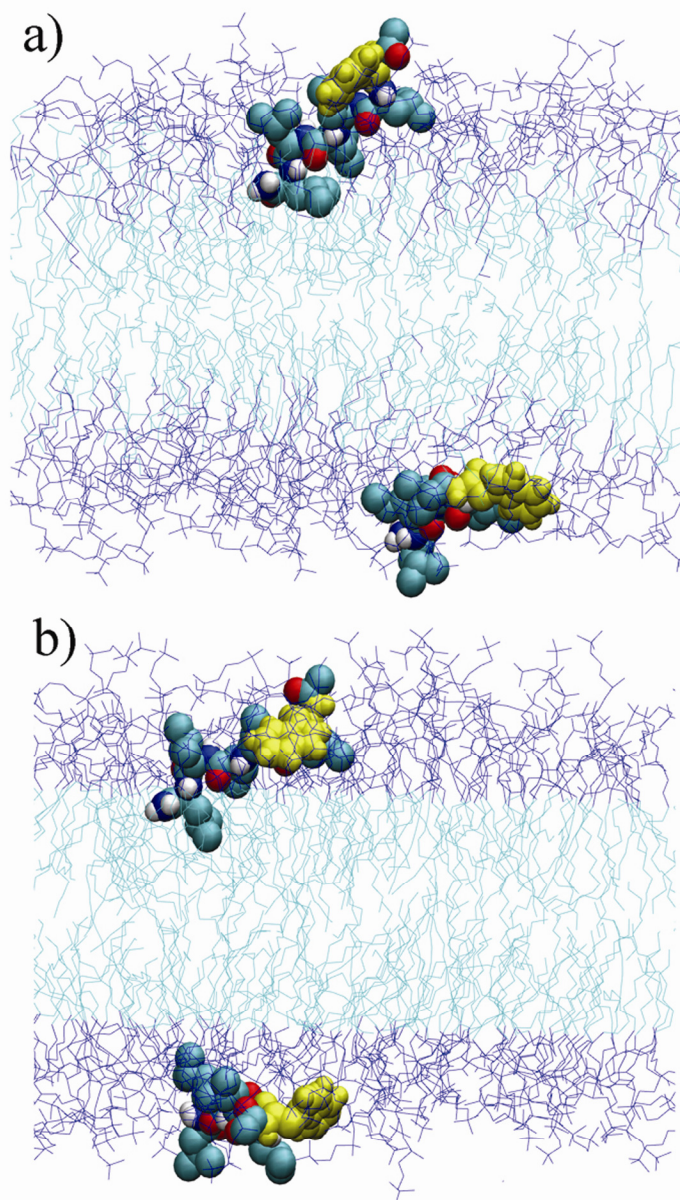


Figure 5: Simulation snapshots at a) 25 ns and b) 50 ns. Lipid head groups and tails are colored in dark blue and light green, respectively. Peptides are shown in the van der Waals representation, colored by atom (carbon = light green , nitrogen = dark blue, white = hydrogen, red = oxygen). The entire TRP residue in each peptide is colored yellow. Water molecules are omitted for clarity.

of the indole group include the propensity of the indole nitrogen for hydrogen bonding and the orientation of the indole ring in the membrane host.

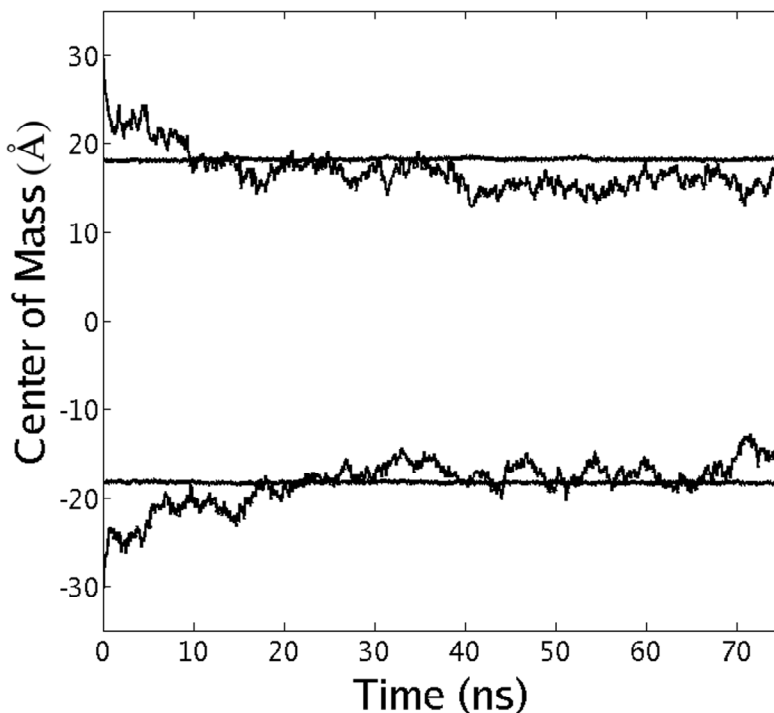


Figure 6: Position along the membrane normal vector (z -axis) of the peptide centers of mass as a function of time. Horizontal lines represent the position of the phosphorus atoms in the lipid head groups. The membrane is centered on the zero position; thus, profiles in the positive and negative zones correspond to the upper and lower membrane leaflets, respectively.

The TRP residue contributes significantly to the hydrogen bonding interactions of the entire peptide. Averaging over the entire course of the simulation (see Figure 7a), we find that TRP accounts for approximately 43% of the total peptide-membrane hydrogen bonds in the upper leaflet and 14% in the lower; thus, the TRP residue contributes significantly more to the hydrogen bonding in the upper leaflet of the membrane. Considering that TRP harbors only 3 of the 15 hydrogen bonding elements in the peptide,

one would expect its contribution to be about 20%. Moreover, the entire peptide in the lower leaflet forms more hydrogen bonds with the membrane host, and this peptide penetrates the membrane slightly less than its counterpart in the upper leaflet. Although we do not definitively present such a relationship here, our results suggest that peptide insertion is directly correlated with the extent of hydrogen bonding.

The TRP residue contains three hydrogen bonding elements: the hydrogen-accepting carbonyl of the backbone; the hydrogen-donating amide also of the backbone; and the hydrogen-donating nitrogen atom of the indole ring. The indole side chain appears to be primarily responsible for the hydrogen bonding of the TRP residue in both peptides, during most of the simulation (see Figure 7b). During the entire length of the simulation, this nitrogen heteroatom accounts for 81% of the hydrogen bonds formed between tryptophan and the membrane. This data suggests then that the indole ring contributes most significantly to the hydrogen-bonding potential of tryptophan, which in turn contributes to the hydrogen bonds formed between peptide and membrane. The prevalence of such hydrogen bonding between tryptophan and a membrane host has also been noted experimentally.⁹³ Thus, although hydrogen bonding alone does not explain the interfacial localization and stabilization, it is clear that the peptides hydrogen bond significantly with the membrane.

In addition to hydrogen bonding, the orientation of the indole ring is relevant for peptide localization and stabilization in a membrane host. We examine temporal variations in the angle between the plane of the indole ring and that of the membrane in both leaflets. As shown in Figure 8 (the dashed profiles), the orientation of the TRP

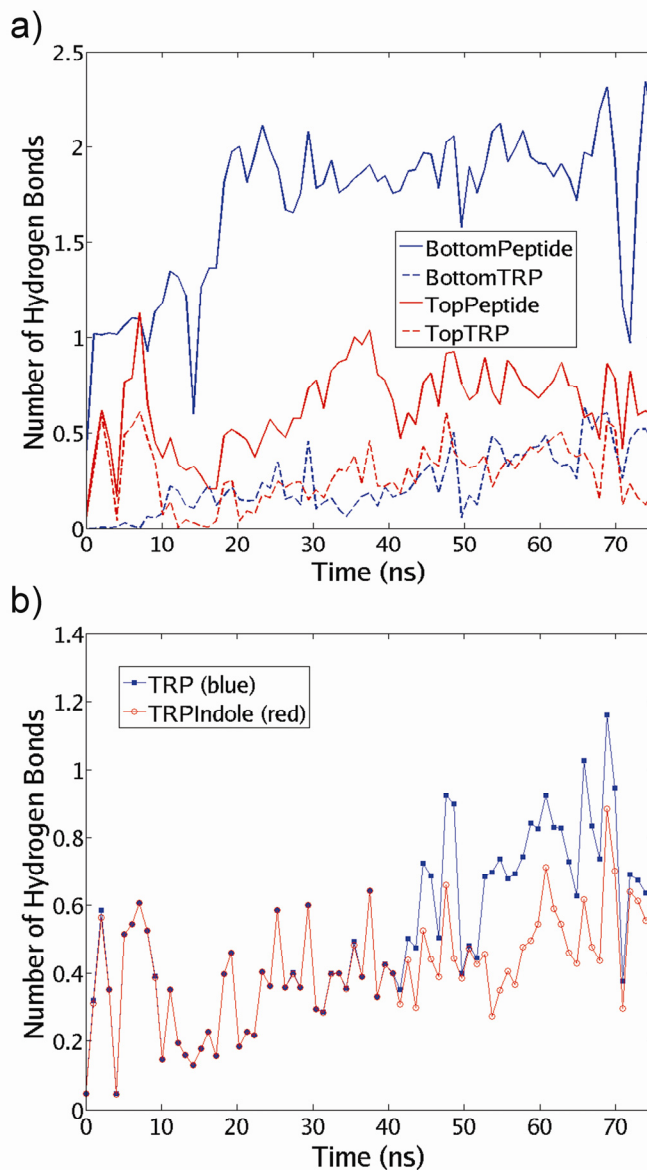


Figure 7: Average number of hydrogen bonds formed (over each ns of simulation). The cut-off criteria for hydrogen bonding was set to an angle of 30° and a radius of 0.3 nm. a) Red and blue lines indicate profiles in the upper and lower membrane leaflets, respectively. Solid and dashed lines indicate hydrogen bonding between the membrane and the entire peptide or just the TRP residue, respectively. b) Average number of hydrogen bonds between the indicated entity—either the entire TRP residue (blue squares) or just the indole side chain (red open circles)—and the DMPC membrane.

indole rings fluctuates dramatically during the first half of the simulation but converges in the second half. During this last portion of the simulation, the average orientation angle of the indole ring in the upper leaflet is $26.2 \pm 6.9^\circ$ (averaged over blocks of 1 ns). That angle in the lower leaflet is $54.2 \pm 6.8^\circ$. It appears that the most stable orientation angle of the indole ring in the membrane is neither 0° nor 90° but an intermediate value. Moreover, the fluctuation of the ring is small in magnitude ($\sim 7^\circ$) thus demonstrating the constriction of the indole ring (at least with respect to its orientation angle). This is consistent with the previous discussion on the propensity of the indole ring to form hydrogen bonds. Because of its strong interactions with the membrane, the indole ring converges tightly to a particular orientation angle.

As the peptides insert, they are oriented parallel to the membrane plane. Following insertion, the peptides adopt a more tilted orientation during stabilization (see Figure 8, solid line profiles). This tilting can be rationalized in terms of thermodynamics; the preferred state of the hydrophobic leucine side chains is buried inside an apolar environment (the membrane core), while the preferred state of the indole ring is situated at the membrane interface. Thus, the indole ring acts as an anchor or a pivot point, about which the rest of the peptide rotates to insert into the membrane. In both leaflets, the peptide tilt angles converge to similar values. In the upper leaflet—as averaged over the last half of the simulation and in blocks of 1 ns—the tilt angle is $62.3 \pm 4.3^\circ$. In the lower leaflet, the value is slightly larger at $73.8 \pm 5.3^\circ$. These angles are comparable to experimentally-determined tilts. For example, Bradshaw *et al.* observed a tilt angle of 55° for a fusion peptide.⁷⁶

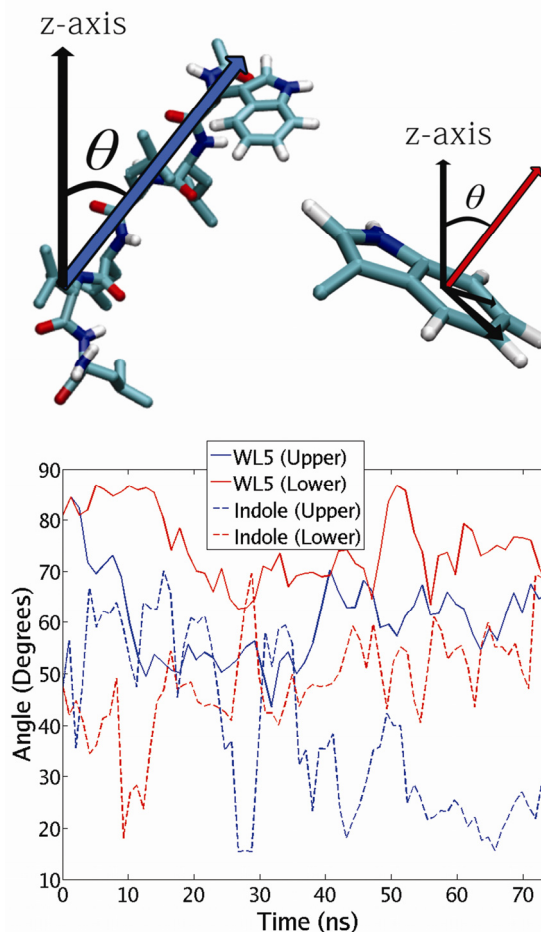


Figure 8: Orientation angles of the peptide and tryptophan side chain. Top panel of the figure describes the angles in question. Solid and dashed-line profiles represent the tilt of WL5 and the indole ring, respectively. Blue and red profiles depict the upper and lower leaflets, respectively. Data points are averaged over each ns of simulation.

If tilting is the result of a hydrophobic effect, what prevents the peptide from relaxing to a perpendicular conformation relative to the membrane plane (an angle of 0 degrees in Figure 8)? Such an orientation would result in maximizing the hydrophobic interactions of the leucine residues, thus resulting in a presumably more favorable system. We suggest that hydrogen bonding plays a critical role here. In the lower leaflet,

the peptide forms more hydrogen bonds with the membrane than in the upper leaflet (see Figure 7a). As a result, the tilt angle of the peptide in the lower leaflet is significantly greater, suggesting that the peptide is more parallel to the membrane plane. From these results, it appears that an increase in the number of hydrogen bonds causes the peptide to localize to the interface where it exhibits a parallel orientation.

Interestingly, the peptides acquire some secondary-structure characteristics as they insert and stabilize into the membrane (see Figure 9). The Ψ/Φ angles of the non-terminal residues of the peptides are localized in the upper left quadrant of the Ramachandran plot during the majority of the simulation. This quadrant is characteristic of β -sheet structure.⁹⁴ As averaged over 1 ns blocks during the entire simulation, the mean Φ of the internal residues is $-110.2 \pm 30.7^\circ$, while the mean Ψ is $+110.3 \pm 15.4^\circ$. These values contrast to those of the peptide in solution, prior to membrane insertion, during which we observe a broader distribution of Ψ/Φ values, varying by as much as 60° . These results suggest that the membrane host restricts the atoms of the peptide backbone, such that the Ψ/Φ angle distribution is narrow and centered on the values consistent with β -sheet structure.

Despite the evidence for β -sheet structure, the peptide is too small to form intramolecular secondary structure. However, such secondary structure can be achieved by the intermolecular interactions of several WL5 peptides. As observed by Wimley *et al.*, multiple units of this model peptide (WL5) can assemble to form a larger β -barrel.⁸¹ To probe the time scale of interaction between WL5 peptides, we examined their diffusion properties in the membrane plane. Figure 10 shows their displacement as a

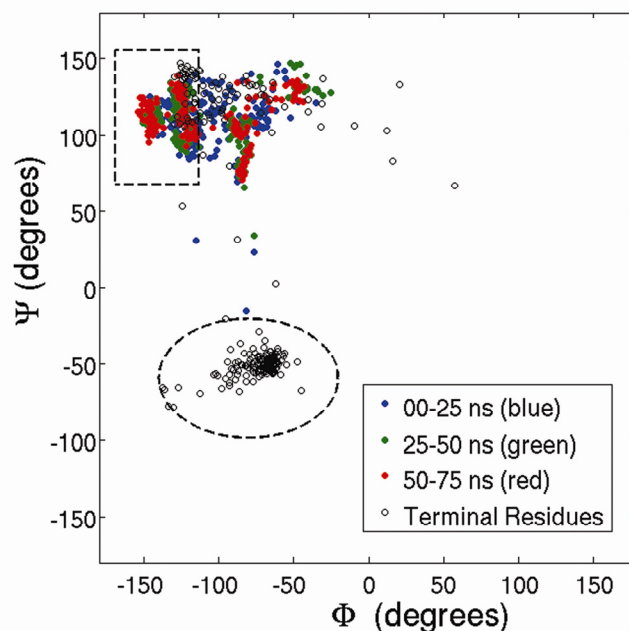


Figure 9: A Ramachandran plot, averaged over all of the non-terminal (colored dots) and terminal (open black circles) residues of both peptides and over 1 ns blocks. Blue, green, and red dots correspond to the beginning, middle, and end of the simulation, respectively. Terminal residues are shown over the entire simulation, clustering mostly in the region bound by the ellipse (non β -sheet conformations). The non-terminal residues explore the upper-left quadrant, which is characteristic of β -sheet conformations (in particular, the boxed area).

function of time. As a first approximation, the slope of the fit to these profiles (approximately $6 \text{ \AA}^2/\text{ns}$) yields information about the mobility of the peptides. Since the peptides do not significantly translate along the membrane normal after the insertion event, most of this displacement occurs in the membrane plane.

At a diffusion rate of approximately $6 \text{ \AA}^2/\text{ns}$, and with a cross-sectional membrane area of about 3624 \AA^2 , the peptide should sample the entire membrane surface in approximately 600 ns. To approximate the time scale of interaction between two

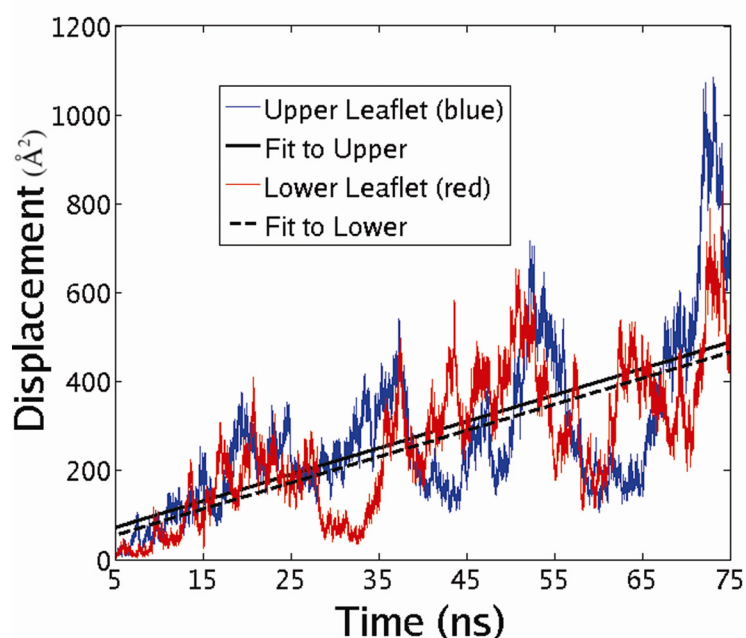


Figure 10: Displacement as a function of time, of the center of mass of the peptide in each leaflet. Reference coordinates are taken from a snapshot after 5 ns, when the peptides have inserted. Blue and red profiles correspond to the upper and lower leaflets of the membrane, respectively. Solid line is a linear fit to the blue profile, while the dashed line is a fit to the red profile. The slopes of both lines are approximately $6 \text{ \AA}^2/\text{ns}$, and this is taken to be an approximate diffusion rate.

peptides in the same leaflet (not simulated here), it is critical to know the experimental concentrations of WL5 in the membrane. In one experiment, Wimley *et al.* use a peptide:lipid ratio of 2:100.⁸² Extrapolating from our simulation here, a 100-lipid model membrane would occupy an area of 6000 \AA^2 . Two peptides migrating in this plane, at the aforementioned diffusion rate and assuming each peptide must cover only half of the area, could come into contact in approximately 0.5 \mu s . For this small model peptide to form a macromolecular assembly, the estimated time scale ($\sim 500 \text{ ns}$) is accessible by all-atom MD simulations, and we intend to study such associations in subsequent simulations.

The deuterium order parameters of the carbon atoms in the lipid tails provide insight into the physical properties of the membrane. Each order parameter, S_{CD} , is defined as:

$$S_{CD} = \frac{1}{2} \left\langle 3 \cos^2 \theta_n - 1 \right\rangle \quad (8)$$

where θ_n is the angle between a vector along the methylene/methyl hydrogens of the carbon atom in question and the vector normal to the membrane plane.⁷⁸ For a particular carbon atom in a lipid tail, a larger order parameter correlates to minimal fluctuation in atomic location.

When modeling the insertion of a peptide into a membrane, the order parameters change as the insertion and stabilization events proceed (see Figure 11). The order parameters of nearly every carbon increase as a function of time. The most dramatic change can be noted when comparing the profile at 1 ns vs. 75 ns. It appears that the most statistically significant increase of the order parameters occurs in the lipid carbon atoms that reside near the membrane core (carbons 8 to 13). Thus, the insertion and stabilization of these peptides in the membrane has a slight ordering effect on the lipids. The cross-sectional area of the membrane was fixed via the dimensions of the simulation box. The thickness of the membrane, defined as the distance between the phosphorus atoms in the upper and lower leaflets also exhibited minimal change (see Figure 5). Thus, the ordering observed here is likely to originate from packing and constricting of the lipid carbon atoms, and this increased constriction may be a direct consequence of peptide insertion into the membrane.

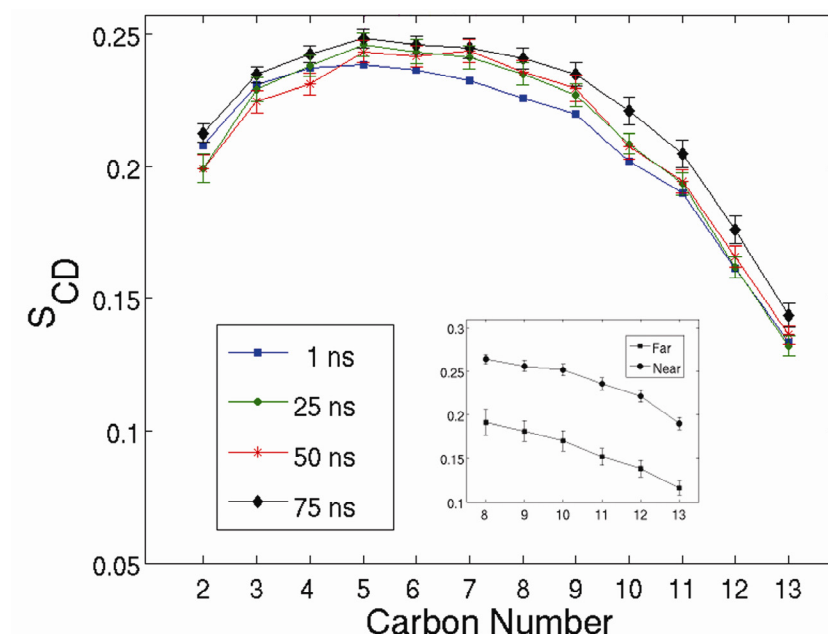


Figure 11: Deuterium lipid order parameters of the acyl chains in DMPC, shown at 1, 25, 50 and 75 ns of simulation (error bars are based on 1-ns block averages). Top and bottom leaflets were averaged together. Lower carbon numbers are those closer to the lipid head groups, while higher ones are those closer to the membrane core. The inset shows how the order parameters of the lipid carbon atoms differ near the peptide (within 10 Å, top curve, circles) and far from it (greater than 10 Å, bottom curve, squares).

The observed changes in membrane structure are likely local effects. In contrast, a global disruption of a biological membrane occurs primarily when numerous peptide units simultaneously insert and aggregate, as in the case of melittin.⁹⁵ We suggest that the observed ordering reported here is localized to the region surrounding the peptide. The inset of Figure 11 demonstrates this, where one can see that the lipid carbon atoms near the peptide (within 10 Å) are significantly raised. However, one should be careful in making any generalizations here; it is not always the case that a peptide raises order parameters in its vicinity. The exact effect of any membrane solute on the order

parameters is probably a function of that solute's chemical nature and position. In any case, one can note that there is a significant perturbation to the order parameters, and that the change is a local one occurring near the peptide. Moreover, as found in our previous study, such a local effect can perturb the lateral pressure profile in the membrane.⁹⁶ Specifically, we observed that an embedded peptide changes the lateral pressure and increases the surface tension in the membrane. In turn, these effects can alter the physical properties of other transmembrane proteins, such as channel gates.⁹⁷

In the discussion of transmembrane protein folding, it is often debated whether the transmembrane protein in question is shaped by the membrane, or whether the latter is perturbed by the former; indeed, there are several examples of both cases.^{98,99,100} It is not surprising that the model membrane presented here can induce specific conformational changes in such a small peptide. It is especially intriguing that this small peptide can in turn cause significant changes to the membrane. Thus, as peptides insert and stabilize, the effect of small solutes on the membrane structure should not be neglected and may play a significant role in many biological processes.

3.4 Conclusion

All-atom molecular dynamics simulation results of the insertion, positioning, and stabilization of a small model peptide into a membrane have been presented here. The spontaneous insertion event is followed by a stabilization phase which is characterized by increased hydrogen bonding, restricted side chain orientation, and tilting of the peptide. We demonstrate how the tryptophan residue plays a crucial role during both the insertion

and stabilization phases. Furthermore, we find that the membrane environment can induce significant secondary-structure conformations in the peptide WL5, while the peptide itself induces an ordering effect in the membrane. We also present a discussion about the mobility of the peptides in the membrane plane which affords a time scale for macromolecular assembly.

Interestingly, with respect to the tryptophan residue, a transmembrane protein does not always present its TRP residues at the membrane interface. Kelkar *et al.* discuss how some proteins—such as membrane channel or gating proteins—actually fluctuate their TRP residues from the interface to the membrane core. Such a fluctuation is related to their open and closed conformations and is thus not primarily driven by the interfacial preference of TRP. Although the interfacial location is likely the most thermodynamically stable position for TRP, the movement of the TRP residue away from the interface can have other structural and functional consequences.¹⁰¹

What then is the energetic cost of moving the TRP-containing segment of the protein (or in our case, just the entire model peptide) from the interface to the membrane core? This question has been addressed via simulation for just the indole side chain of TRP but not yet for an entire peptide.¹⁰² In subsequent studies, employing the simulation techniques of non-equilibrium molecular dynamics, we hope to calculate the energetics of WL5 movement across the membrane. Coupling these future simulation results with experimental data will allow us to further elucidate the details of transmembrane protein insertion, positioning, and stabilization.

3.5 Acknowledgements

Funding for this project was provided by the Howard Hughes Medical Institute, NSF, NIH, the Center for Theoretical Biological Physics and the National Biomedical Computation Resource.

Chapter 3, in full, is a near reprint of the material as it appears in *Biopolymers* 2007, Volume 85, Pages 490-497. This is a co-authored article. The dissertation author was the primary investigator and author of this paper. A. A. Gorfe, J. Gullingsrud, and J. E. Kim contributed in an advisory capacity. J. A. McCammon served as the head adviser and principal investigator.

CHAPTER 4: Thermodynamics of Peptide Insertion and Aggregation in a Lipid Bilayer

4.1 Introduction

The lipid bilayer plays critical roles in the biochemistry of cells, the most basic of which being its role in defining the shape of the cell and organelles. The unique arrangement of hydrophilic and hydrophobic groups at the membrane exterior and interior regions, respectively, allows for a selective inhibition of foreign agents and transport of essential molecules.^{103,104} As a consequence, the membrane plays vital immunological functions.^{105,106} The functional versatility of the cell membrane is also in tune with its highly inhomogeneous composition and structure, wherein receptors, channels, peptides and other molecules create a vast chemical mixture and diverse geometry.¹⁰⁷ The thermodynamics of adhesion and membrane insertion of biomolecules is therefore the subject of much research. In the context of protein folding, for instance, understanding how membrane proteins insert and simultaneously fold to assume their functional three-dimensional structure is of great interest.¹⁰⁸ This poorly-understood process can involve the cooperative action of several amino acid residues that work in concert towards both membrane penetration and organization to a particular shape.

Researchers are also studying how smaller biomolecules insert into the membrane and aggregate, and to what extent these processes affect the physical properties of the membrane.^{109,110} Several experimental methods have been employed to describe the

equilibrium properties of peptide insertion, that is, to describe the initial and final states and the associated thermodynamic properties.^{111,112,113} The most important thermodynamic parameter in this context is the free energy change, ΔG , defined here to be the energetic change upon the transfer of the peptide from its initial aqueous environment to its final state in membrane; $\Delta G < 0$ indicates a favorable insertion process. Wimley *et al.* studied the free energy of amino acid partitioning first in an octanol/water¹¹⁴ membrane mimic and later in a synthetic membrane.⁷⁵ In the latter study, they derived a thermodynamic scale for the partitioning of small model peptides between membrane and water. By altering a single residue in the test peptide, the contribution of each of the 20 amino acids to the transfer free energy was tabulated. For instance, in the case of the hydrophobic amino acid leucine, the free energy of transfer is -0.56 ± 0.04 kcal mol⁻¹. Wimley and White also contemplated how peptide aggregation or formation of higher order molecular assemblies might occur in membranes.^{82,115}

Concurrently, computational methods have played significant roles in elucidating the atomic-level details that are not always accessible by experiment. The advance of computational power and the development of faster algorithms enables modeling of increasingly larger membrane systems.^{116,117,118,119} For example, Aliste *et al.* used MD simulations to study the partitioning of the Wimley and White peptides in a model membrane, and the results provided the details of the peptide-membrane atomic interactions responsible for insertion.⁷⁴ The partitioning of the various amino acids into a model membrane host has also been studied.¹²⁰ A unique benefit of computation is its ability to shed light on the free energy of peptide-membrane binding, as well as to characterize the energetic landscape or the pathways of insertion and aggregation. One

such study examined the free energy profile (or the potential of mean force, PMF) of the chromophore indole ring as it traveled through the membrane.¹⁰² In this work, the authors explored how different parameterizations of the indole moiety can affect the free energy calculations; they also pinpointed some key properties of the reaction coordinate, including the locations of energetic barriers.

In this study, we employ a molecular dynamics (MD) technique known as ‘umbrella sampling’^{121,122} to simulate the insertion of a model hydrophobic peptide into a membrane. The model of choice is the small hexapeptide consisting of one tryptophan (TRP) and five leucine residues (WL5), the same model system used in the experiments of Wimley and White.⁸² We computed the PMF as the peptide moves from the solvent, inserts into, and completely traverses across the membrane. To our knowledge, this is the first attempt in computing the free energy profile of a full length peptide as it crosses a membrane. We analyzed the dynamical and structural properties of the peptide during this process. By coupling the computed free energy profile with the experimental results of Wimley and White, we propose a thermodynamic model for the insertion and aggregation of hydrophobic peptides in a membrane host.

4.2 Materials and Methods

The structure of the solvated peptide-membrane system was obtained from a previous study, in which we explored the properties of the system in a 75 ns MD simulation.¹²³ Snapshots at the end of this simulation—at which point, the peptides were embedded within the head group region of the membrane—were used as starting

configurations to initiate 50 different all-atom simulations each representing a window in an umbrella sampling scheme. Two different snapshots of the peptide were employed (one for each leaflet of the membrane); in other words, the 25 simulation windows within a leaflet were initiated with the same initial peptide conformation. These two snapshots are taken to be the equilibrated conformation of the peptide when embedded in the solvent-head group interfacial region of the membrane.

In total then, the 50 simulation windows consisted of a WL5 peptide (acetylated and amidated at its N- and C-Termini, respectively), a pre-constructed bilayer of 128 dimyristoylphosphatidylcholine (DMPC) lipids,⁷⁴ and 6631 water molecules, resulting in a ~25,000 atom system assembled in a simulation box of $60 \times 60 \times 95$ Å. The membrane was positioned at the center of the box, leaving approximately 23 Å for the solvent on either side.

Each simulation corresponds to a window of width 1.9 Å such that the position of WL5 was different in each simulation. In the first window, WL5 was constrained (along the z-axis) in the bulk solvent at the upper half of the box and well away from the membrane surface. In the next, WL5 was moved by 1.9 Å closer to the membrane and constrained at that position. In subsequent simulations, WL5 was moved closer to the center of the simulation box each time stepped along the z-axis by the increment of 1.9 Å. The constrained molecule thus spans the entire reaction coordinate (in the z-direction) of approximately 95 Å.

For organizational purposes, the simulation box is divided into two halves along the z-axis, representing the ‘upper’ (positive z) and ‘lower’ (negative z) leaflets with respect to the membrane center at $z = 0$. Among the 25 simulation windows in each

leaflet, 12 had the peptide constrained in solvent and 13 were carried out with the peptide constrained at various z-locations in the membrane. The initial configuration of the peptide differs between the two leaflets but is the same amongst the 25 simulation windows of each leaflet. The reaction coordinate was defined by the separation along the z-axis between the centers-of-mass of the indole chromophore—the tryptophan side chain—and the membrane. WL5 was constrained by a harmonic potential of force constant $500 \text{ kJ mol}^{-1} \text{ nm}^{-2}$ ($1.20 \text{ kcal mol}^{-1} \text{ \AA}^{-2}$).

The setup of the simulations was as follows. First, unfavorable contacts were relieved by two cycles of 5,000 steps steepest descent followed by 5,000 steps of conjugate-gradient energy minimizations, each with the peptide held fixed and set free. Second, except when the peptide is in bulk solvent, an annealing step was conducted to equilibrate the lipid tails around the peptide. With the peptide and lipid head groups restrained, the system was gradually heated (over 1 ns) from 310K (the temperature of the initial snapshot) to 410K, then gradually cooled back down to 310K. Third, adding pressure coupling, a restrained MD was performed on all 50 windows for 1 ns, with the restraint applied to non-solvent molecules. Fourth, with only the indole ring of tryptophan constrained to its selected position, production runs commenced. Those with the peptide located outside of the membrane were sampled for 5 ns, while those with the peptide somewhere in the membrane were sampled for 25 ns. In total, including all pre- and post production runs, approximately 850 ns of all-atom MD simulations have been carried out.

A time step of 2 fs was used while coordinates/velocities were recorded every 500 steps (1 ps). Constraints were imposed using the LINCS method. Full electrostatics were calculated using the particle mesh Ewald (PME) method, with coulombic and van der

Waals cut-offs of 0.9 and 1.4 nm, respectively. A sixth-order spline interpolation was used for PME along with a tolerance of 1×10^{-5} . Nearest neighbor lists were updated every 10 steps using the grid method and periodic boundary conditions (in xyz) were employed with a cut-off of 0.9 nm. Berendsen temperature coupling was used, with a reference temperature of 310 K and a coupling of 0.1 ps. A semi-isotropic pressure coupling scheme—in which the x-y dimensions are coupled together, while the z-direction is allowed to fluctuate independently—was used, with a reference pressure of 1.0 bar, a pressure coupling of 0.5 ps, and a compressibility of $4.5 \times 10^{-5} \text{ bar}^{-1}$.

The simulations were performed with the GROMACS MD package.¹⁹ The ffgmx force field was used for the peptide and the SPC water model was used as the solvent. The lipid parameters of Berger *et al.* were employed for the DMPC lipids.⁸⁶ The analysis of the simulation trajectories was completed using the various GROMACS tools. For further details regarding these tools and specific procedures in running GROMACS MD simulations, see the GROMACS manual at <http://www.gromacs.org/>. Visualization and rendering were done by the Visual Molecular Dynamics application (VMD).⁵¹

Given the construction of the simulation windows, one might expect the resulting profile in Figure 12 to be perfectly symmetric about the membrane center. In other words, the profile in one leaflet should be a mirror image of the other provided that the peptide exhibits the same orientation while penetrating through both leaflets of a homogenous membrane. As mentioned in the text, the free energy profile of Figure 12 is not exactly symmetric, and this was attributed mainly to the starting conformation of the peptide in the simulation windows of each leaflet. Yet, even if the peptide conformation was the same in each leaflet, it is doubtful that one could achieve great symmetry, simply due to

convergence limitations inherent in MD simulations. An exorbitant amount of computational time would be needed to achieve such a result. In fact, the asymmetric profile may be used as a convergence criterion with respect to certain free energy calculations.

For instance, the values of the computed $\Delta G_{\text{HG/C}}$ in the upper and lower leaflets are within 1 kcal mol⁻¹ of each other while the values of $\Delta G_{\text{S/HG}}$ differ more significantly. This could signify that the simulation of deep insertion (from bulk solvent into the deep interface) produces a more converged result than insertion into the solvent-head group (S/HG) interface. One could reason that this is the case because the S/HG interface is more chemically diverse and dynamic, thus requiring more sampling time for energetic calculations. In Figure 12, the symmetric profile was obtained by averaging the results of the two leaflets. About the center of the profile (at 0 Å), the average was taken between the two points on either side of the profile. For instance, if the free energy was 1.8 kcal mol⁻¹ at +10 Å (upper leaflet) and 1.5 kcal mol⁻¹ at -10 Å (lower leaflet), the free energy in the symmetric plot at ±10 Å is taken to be 1.65 kcal mol⁻¹. The asymmetric free energy profile in Figure 12 can also be used as a judge of error in these simulations. The differences at mirror sites along the reaction coordinate (for instance, at ±7 Å) reveal a sampling error on the order of 0.5 – 1.0 kcal mol⁻¹.

As reported by Wimley and White, the experimental concentration of the WL5 peptide is (at most) 100 μM.⁸² Using this concentration, and that of water to be 55.5 M (or 55.5×10^6 μM), we can calculate the mole fraction of the peptide in the experiment to be $\chi_{\text{exp,Peptide}} = 1.80 \times 10^{-6}$. In each simulation, we have one peptide, in either the upper or lower leaflet of the system. Because of periodic boundary conditions, the peptide is

solvated in the total solvent of 6631 water molecules. Thus, the mole fraction of the peptide in the simulation is $\chi_{\text{sim,Peptide}} = 1.51 \times 10^{-4}$. Substituting these mole fractions along with the simulation temperature (310K) into the expression for ΔG_{R} , we arrive at $+2.73 \text{ kcal mol}^{-1}$, which corrects for the differences in peptide concentration between simulation and experiment. To calculate the mole fractions of the lipids, a volumetric ratio is computed in a fashion similar to Grossfield *et al.*¹²⁸ Taking the average thickness of a DMPC membrane to be 36 \AA ¹²⁴ and the cross-sectional area to be $60 \times 60 \text{ \AA}$ (per simulation setup), we compute the volume occupied by the membrane to be $1.30 \times 10^5 \text{ \AA}^3$. When the ratio of the membrane volume to the box volume is computed, we obtain $\chi_{\text{sim,lipids}} = 0.38$; we also use $\chi_{\text{exp,lipids}} = 0.24$, for an experimental vesicle concentration of 4 mM.¹²⁷ These mole fractions result in $\Delta G_{\text{Mix}} = +0.28 \text{ kcal mol}^{-1}$, and this corrects for the differences in lipid concentration between simulation and experiment. The combined correction term is then the sum, $\Delta G_{\text{R}} + \Delta G_{\text{Mix}} = \Delta G_{\text{Corr}} \approx +3.0 \text{ kcal mol}^{-1}$.

4.3 Results and Discussion

Each leaflet of the membrane can be divided into three regions based on the polarity of the constituent atoms: the solvent-head group interface (S/HG), where the first two solvent shells ($\sim 6 \text{ \AA}$) merge with the choline and phosphate head groups of the phospholipids; the glycerol or head group-core interface (HG/C), where the lipid head groups mix with the hydrophobic fatty acid chains; and the core, the region occupied by the aliphatic lipid tails. Using these three regions as landmarks, the free energy profile of the peptide WL5 as it traverses across the membrane is shown in Figure 12. The extent of

convergence of this profile (in the allotted sampling time) is shown in Figure 13. The profile exhibits minima at both the S/HG and HG/C interfaces of each leaflet, the latter being the global minimum. Note that two peptide orientations (one per leaflet) were used to determine whether the initial orientation affects the energetics of insertion. The dashed line in Figure 12 clearly shows that the initial orientation does indeed affect the profile. Such an asymmetric profile implies that even for a rudimentary peptide such as WL5, there may be more than one possible path of membrane insertion.

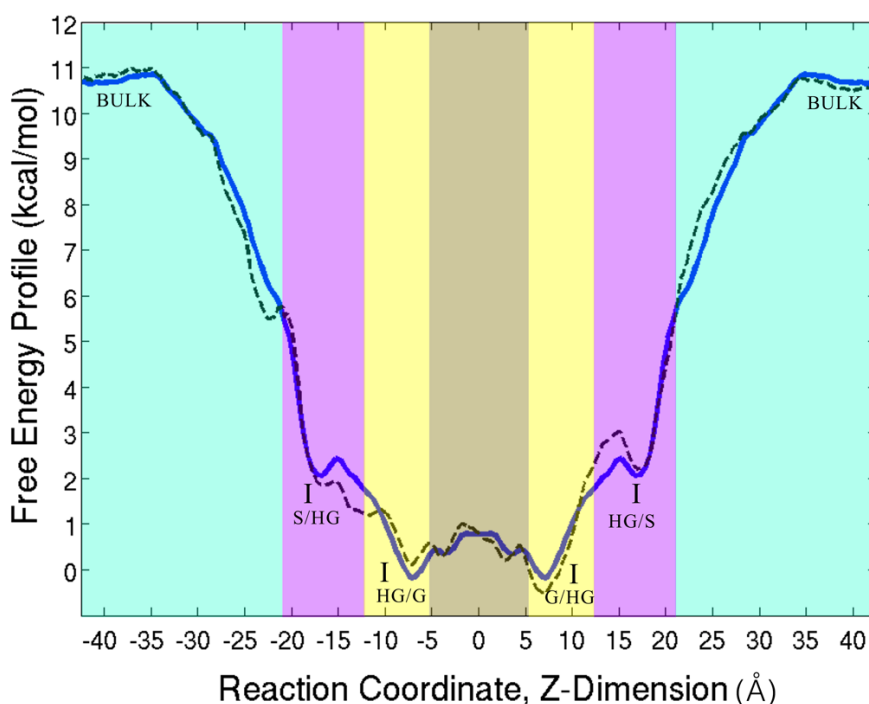


Figure 12: The free energy profile (symmetric-heavy blue line, asymmetric-dashed line) of the peptide as a function of position along the z-dimension (negative/positive values correspond to the lower/upper leaflets, respectively). Aqua green on either side of the simulation box denotes regions of bulk solvent. Pink marks the regions of the solvent/lipid head group interface (S/HG in the lower leaflet, HG/S in the upper). Beige indicates the head group/core interface (HG/C in the lower leaflet, C/HG in the upper). The light brown region centered on the zero depicts the membrane core. See the text for further discussion and the computed changes in free energy.

The conformation of the peptide—as judged by the distribution of Φ/Ψ angles—assumes that of a β -strand, especially when the peptide is positioned somewhere in the membrane; see Figure 14. Most noticeably, the distribution centers on the β -strand Φ/Ψ angles when the peptide is embedded in the HG/C region of the membrane (lower left panel of Figure 14). Such a conformational change may have some effect on the free energy profile of the peptide as it travels through the membrane. Yet, it is difficult to quantify this effect because we have not imposed any constraints on the Φ/Ψ angles of the peptide.

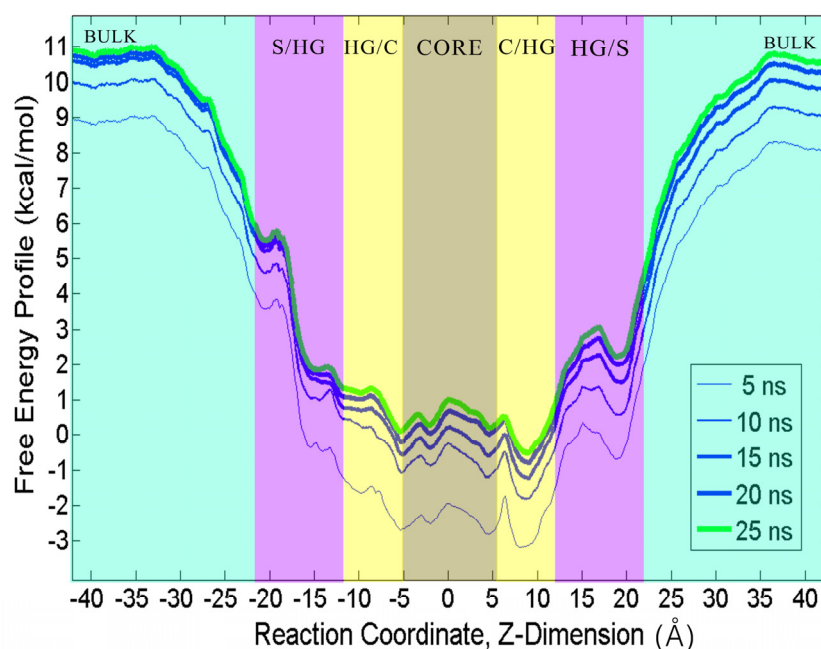


Figure 13: The extent of convergence of the free energy profile—as a function of peptide position along the z-dimension (negative/positive values correspond to the lower/upper leaflets, respectively)—at different sampling times. Aqua green on either side of the simulation box denotes regions of bulk solvent. Pink marks the regions of the solvent/lipid head group interface (S/HG in the lower leaflet, HG/S in the upper). Beige indicates the head group/core interface (HG/C in the lower leaflet, C/HG in the upper). The light brown region centered on the zero depicts the membrane core.

In the upper leaflet, the nitrogen heteroatom points towards the interfacial regions while the peptide moves through the membrane; while in the lower leaflet, the ring nitrogen consistently points towards the core of the membrane (see Figures 15a and 16). This preferential orientation results in distinct and deeper energy minima at the interfacial regions of the upper leaflet while the corresponding minima in the lower leaflet are shallow and less distinct (see Figures 12 and 15b). The location of the minima and the

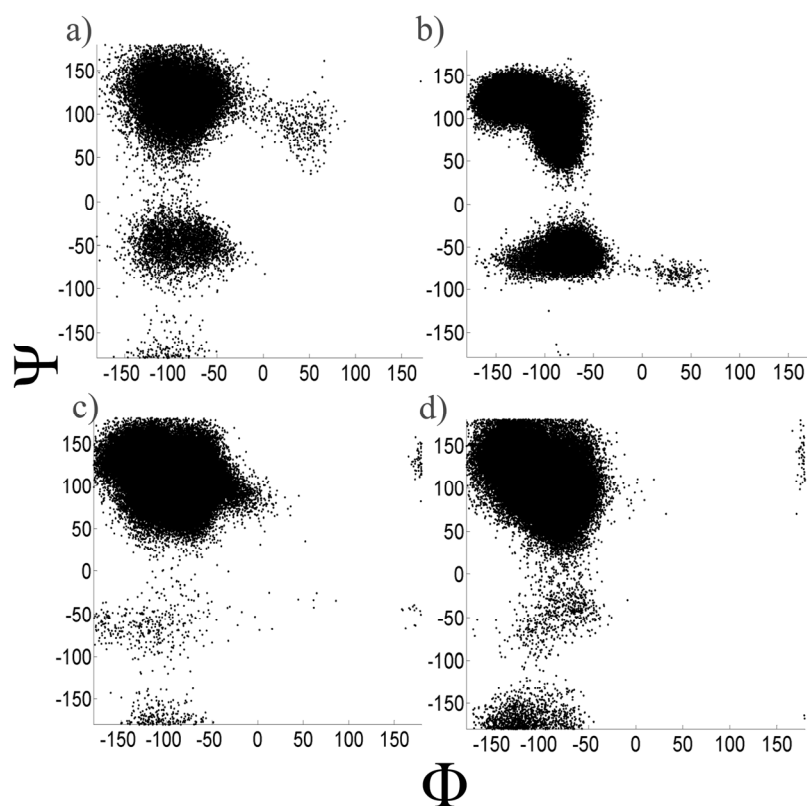


Figure 14: Ramachandran plots of the internal leucine residues in WL5, when the peptide is positioned in various parts of the simulation box: a) in Bulk Solvent ; b) in the solvent-lipid head group (S/HG) region ; c) in the head group-core (HG/C) region ; d) in the membrane core. The upper left corner of each plot is the β -strand conformational space. The peptide assumes the β -strand conformation most prominently in the HG/C region (plot c). See the text of the manuscript for further discussion.

orientation of the indole ring in the upper leaflet indicate that the ring is in a prime position to interact with the glycerol carbonyls and other hydrogen bonding elements of the lipid head groups. The importance and extent of hydrogen bonding between the indole ring and the membrane interfacial region has been addressed in a previous study.¹²³ Here, the nitrogen heteroatom forms a significant number of hydrogen bonds

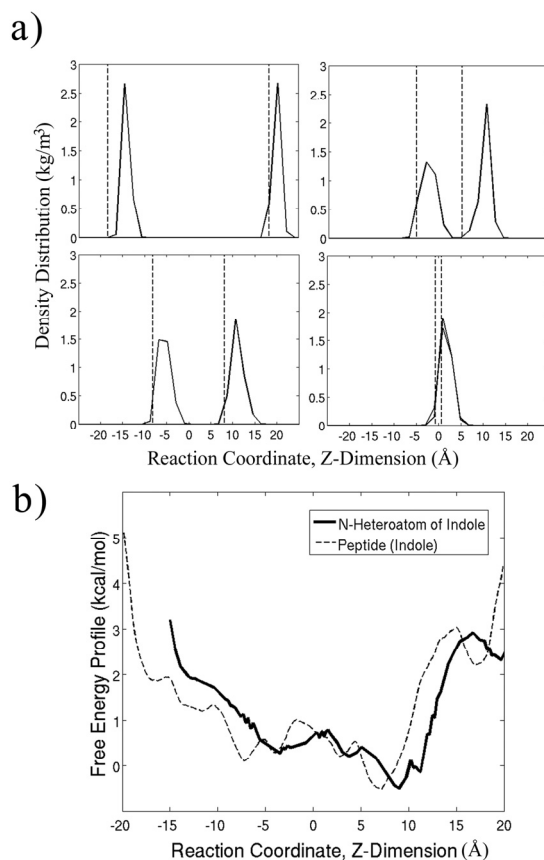


Figure 15: Nitrogen heteroatom distribution along the reaction coordinate. a) Density distributions of the tryptophan indole nitrogen in the upper and lower leaflets of four simulation windows. Dashed lines indicate where the peptide was constrained (via the indole ring) in that particular simulation. b) The asymmetric free energy profile in the membrane (dashed line) and the same profile shifted to reflect the nitrogen heteroatom position (dark heavy line). At each point, the nitrogen is distributed to the right (more positive z) of the indole center; but the magnitude of that shift is not equal in all parts of the profile.

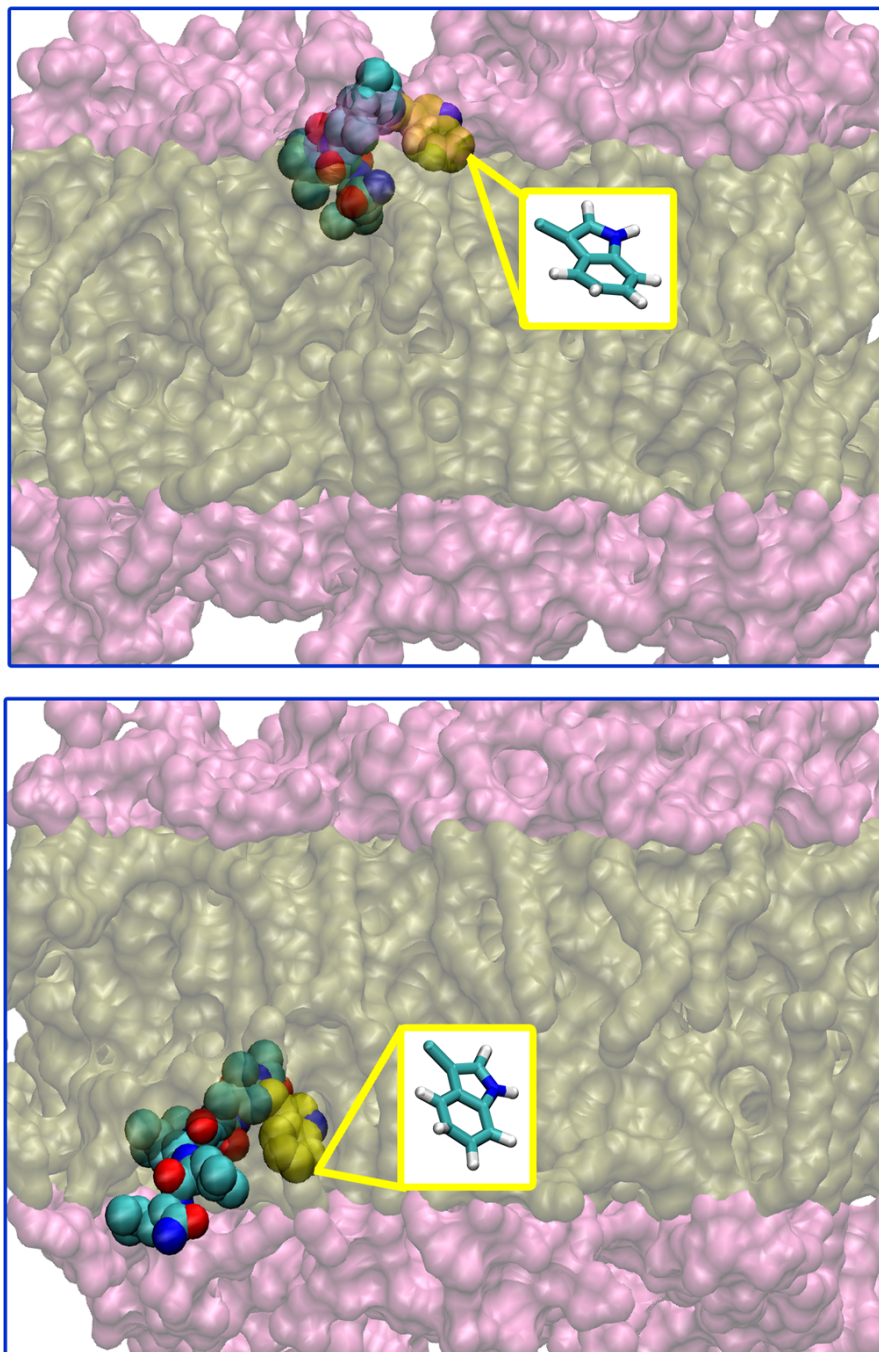


Figure 16: Snapshots of WL5 in the upper (above) and lower (below) leaflets of the membrane. The membrane is shown as a transparent surface with the lipid head groups colored pink and the tails brown. The peptide is shown as van der Waals spheres with the indole ring highlighted in yellow. The insets show a close-up of the indole ring orientation, with carbon, hydrogen, and nitrogen atoms colored in cyan, white, and blue, respectively.

with the membrane, and it does so to a greater extent where the minima occur along the reaction coordinate (see Figure 17). In the upper leaflet, where the minima are deeper and more distinct, a larger number of hydrogen bonds are formed as compared to the minima in the lower leaflet.

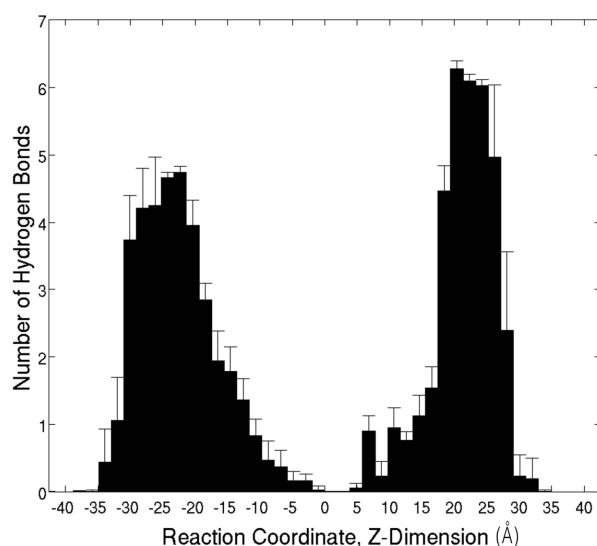


Figure 17: Average number of hydrogen bonds formed between the indole nitrogen and the hydrogen bonding elements of the lipids, as a function of the peptide's position along the reaction coordinate. The cut-off criterion was set to elements within 3 Å and hydrogen bonding angles of 40°.

Analysis with respect to orientation of the entire peptide reveals a tilt in the peptide axis (see Figure 18), an observation common in helical transmembrane-peptide systems.¹²⁵ As it adheres and inserts into the membrane, the peptide axis stabilizes at an angle near 70°, which is off parallel to the membrane plane (an angle of 90°). Such a tilt allows the leucine residues to interact with the hydrophobic part of the membrane while maintaining the indole ring position in the interfacial region. This appears to be the general strategy of transmembrane peptides, in that they are designed to exploit both the hydrophilic and hydrophobic parts of the membrane during the insertion process. The

orientations of the whole peptide and the tryptophan side chain argue that the PMF in the upper leaflet represents a more plausible path of peptide insertion. But in reality, the peptide could approach the membrane in a variety of orientations. Also, it may be the case that the peptide binds the membrane surface in a random initial orientation and then rearranges prior to further insertion and stabilization.

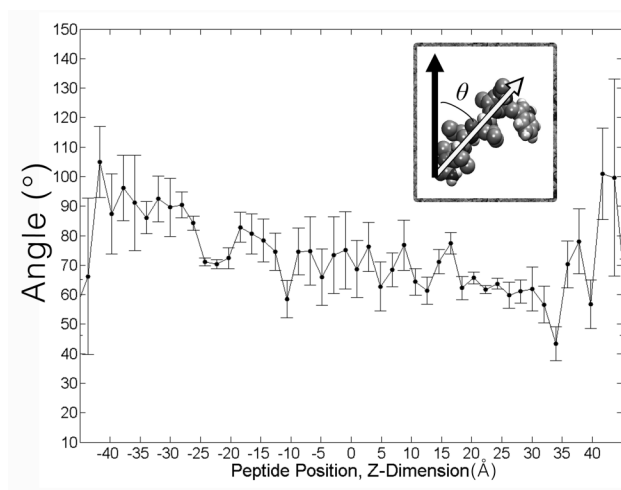


Figure 18: Peptide tilt as a function of position along the z-axis, with the membrane centered on 0. Each data point corresponds to one window. Error bars encompass one standard deviation. Inset shows how the angle is defined by the vector fitted to contain the alpha carbons of the peptide (light arrow) and the vector representing the membrane normal (dark arrow).

However, we do not have any a priori knowledge of the peptide orientation or information on its conformational dynamics at the solvent-membrane interface. Furthermore, the constraint applied at the TRP residue during the umbrella sampling does not allow for a spontaneous reorganization. It is therefore impossible to determine the relative weights of the two profiles and here we assume that the lower- and the upper-leaflet orientations are equally probable. In other words, because the molecular dynamics simulations in each leaflet are separate and independent, one can consider the data from

the upper and lower leaflets as twice the sampling of the same system. Thus, we symmetrize the free energy profile (heavy blue line in Figure 12) and allow this result to reflect the sampling of the entire system (see the Materials and Methods section). This symmetric profile is used for all further calculations and discussion, but we note that this symmetry is due purely to the homogeneity of the model membrane used in the simulations. In biological heterogeneous membranes, however, such symmetry may not exist.

The peptide begins its approach towards the membrane from a region of bulk solvent, where the PMF plateaus (± 35 Å). This plateau indicates that the peptide does not interact with the membrane and instead experiences a purely aqueous environment. The average PMF in this region (aqua-colored in Figure 12) is $10.1 \text{ kcal mol}^{-1}$. This value will be used as the reference point from which the change in free energy (ΔG) will be calculated. In other words, this bulk solvent environment is considered as the initial state of the peptide.

As the peptide travels closer to the membrane, at about 30 Å from the center, the free energy rapidly declines as the peptide encounters the solvent-head group (S/HG) interface. This steep descent can be attributed to a hydrophobic effect. Such a drop in the free energy is often encountered when a hydrophobic solute encounters a like environment.¹²⁶ Inside this S/HG region, the free energy profile continues to decline until it reaches a shallow minimum near ± 17 Å, and the barrier to escape this minimum is approximately $0.5 \text{ kcal mol}^{-1}$. [This barrier seems insignificant given the sampling error of this method (see the Materials and Methods section), and it should be greater. Nonetheless, we know from previous experiment and simulation that a minimum in the

free energy profile occurs here.] The computed free energy change as the peptide inserts into the S/HG interface is $\Delta G_{S/HG} = -8.3 \text{ kcal mol}^{-1}$. Thus the peptide has a tendency to localize in the S/HG region, and this can likely be attributed to the partial hydrophilic nature of the TRP residue.

The peptide descends further into the head group-core (HG/C) interface and encounters a global minimum at about $\pm 7 \text{ \AA}$ and gains a further 2 kcal mol^{-1} in free energy. The total free energy change from the bulk solvent to the HG/C region ($\Delta G_{HG/C}$) is $-10.2 \text{ kcal mol}^{-1}$. A local maximum occurs in the core of the membrane (0 \AA), and the energy barrier as measured from the HG/C region is approximately $1.0 \text{ kcal mol}^{-1}$.

The peptide exhibits considerable conformational changes as it travels through the membrane. The root mean square fluctuation (RMSF) demonstrates how much the peptide deviates from its average conformation and is plotted in Figure 19 as a function of the peptide location along the membrane normal. One can conclude that the peptide is more flexible and samples a wider region of conformational space (has a larger RMSF) as it travels deeper into the membrane core. This flexibility is also demonstrated by the root mean square deviation (RMSD) of the peptide structure, as seen in Figure 20.

An alternative view of the RMSF in Figure 19b further shows that the side chains of the peptide are predominantly responsible for this flexibility. In particular, the TRP side chain has the largest RMSF when deep in the membrane core. To the extent that peptide flexibility can be correlated with entropy,¹²⁷ one can infer that the peptide exhibits increased entropy as it inserts into the membrane. This results in a more negative (or favorable) contribution to the free energy change and explains why the energy barrier in the core is not greater in the calculated profile. Therefore, a small barrier seems to

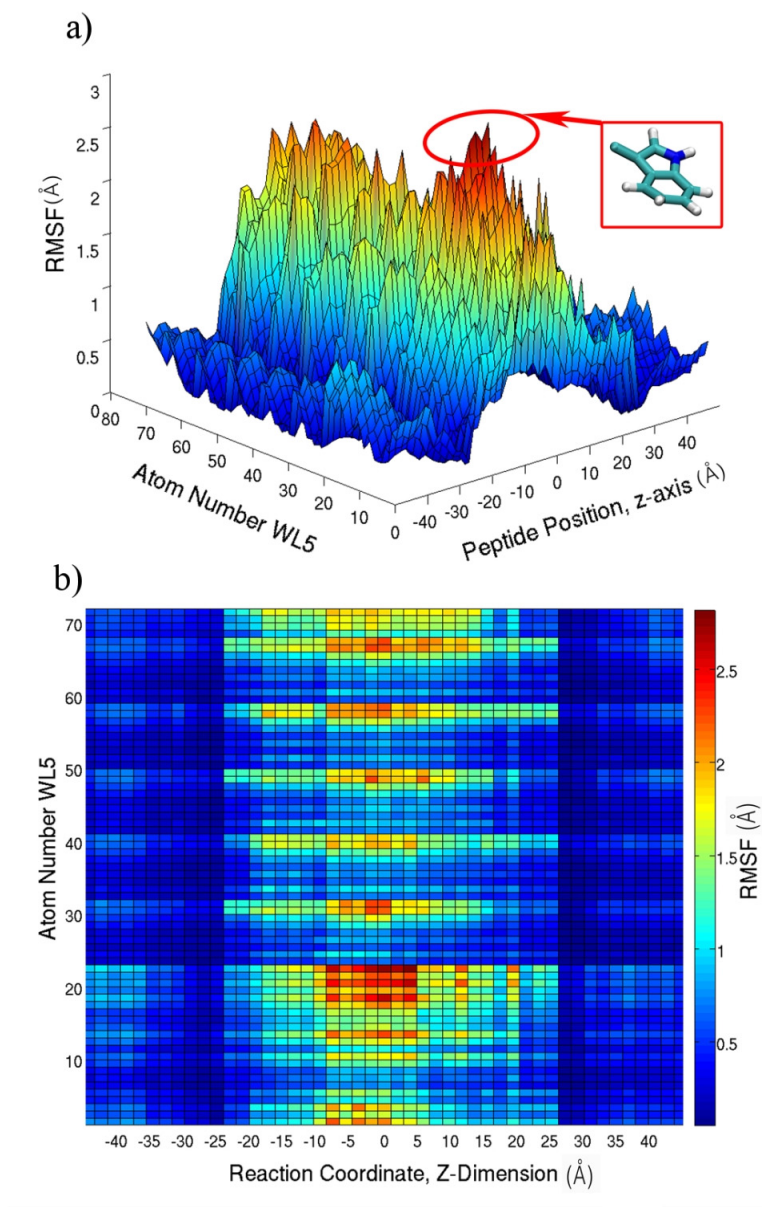


Figure 19: Root mean square fluctuation (RMSF) of the peptide by atom number and as a function of position along the z-axis of the simulation box. The membrane is centered on the zero mark of the z-axis. Atom numbers 1-3 correspond to the acetyl group on the N-Terminus; 4-24 correspond to the tryptophan residue; 25-69 correspond to the leucine residues; and 70-72 correspond to the amide group on the C-Terminus. a) Surface representation, where the red halo shows the maximum RMSF achieved by the indole ring near the core of the membrane. b) An alternative (color map) view of the RMSF data.

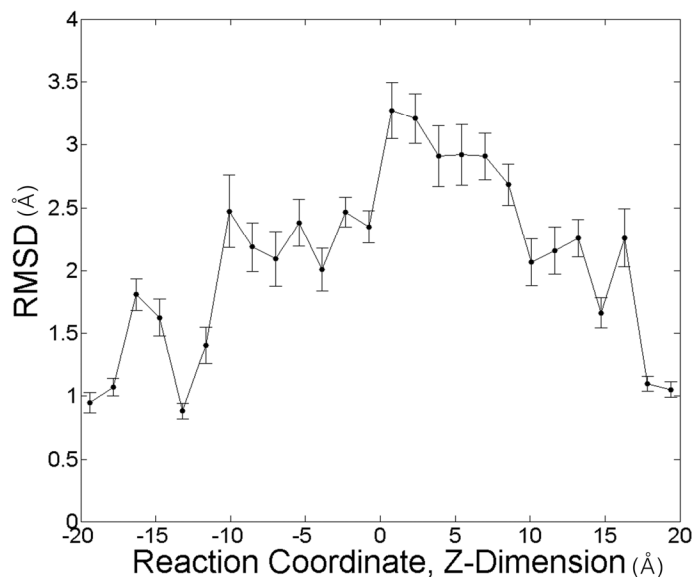


Figure 20: Average root mean square deviation (RMSD) of the peptide (non-hydrogen atoms) as a function of position along the z-dimension (inside the membrane). Error bars encompass one standard deviation.

suggest that the peptide can occasionally translate across the membrane center and shift positions between the two leaflets. Yet, as Wimley and White have demonstrated—and as we shall explore further below—individual units of this model peptide aggregate in the membrane and form a supramolecular structure, a process that can counteract the tendency of a lone peptide to transfer from leaflet to leaflet.⁸²

The free energy profile presented here is that of a single peptide traveling through the membrane and is thus not reflective of the entire biological process. If the final state of WL5 in the membrane is not monomeric but rather an aggregate form, then it behooves us to study this aggregation process and the pathways that lead to it. Although we have not simulated the actual aggregation, the presented work—coupled with previous simulations and experimental evidence—can shed some light on the mechanism and potential pathways of aggregation. Figure 21 shows a proposed thermodynamic cycle

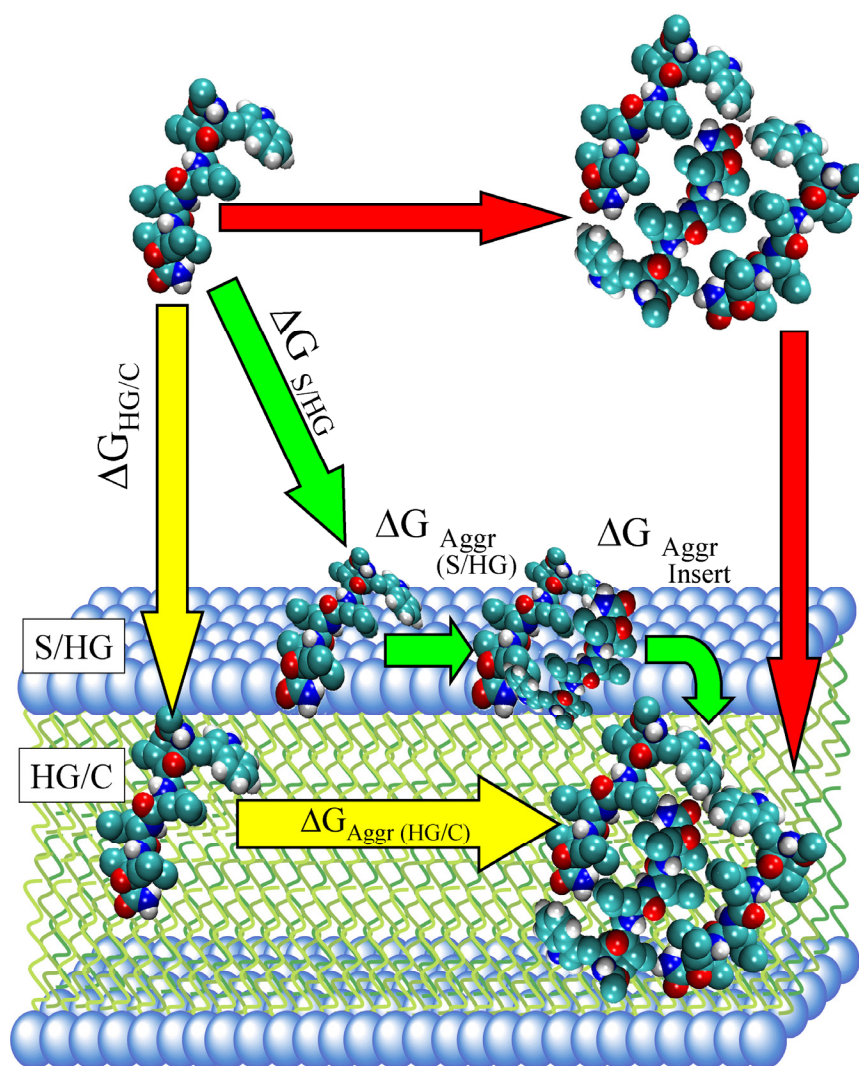


Figure 21: A proposed thermodynamic cycle of peptide insertion and supramolecular assembly inside a model membrane. The yellow arrows depict a pathway in which single peptides insert first into the deep head group-core (HG/C) interface and then aggregate to form the final structure. The red arrows mark a less likely (yet plausible) path, in which the peptide aggregates first in solution, and then the aggregate as a whole inserts into the membrane. The green arrows qualitatively describe an intermediary pathway, in which individual peptides insert first into the aqueous or solvent-head group (S/HG) interface, aggregate to some extent, and then insert deeper into the membrane. Each of these steps can be described by a free energy change (ΔG , Aggr = aggregation). See the text for further discussion.

for the insertion and assembly of WL5 in the membrane. In this model, the initial state of the peptide in an aqueous environment is monomeric and the final state in membrane is an assembly of several monomers (top left and bottom right of Figure 21, respectively). The difference in the free energy between these two states as obtained by Wimley and White is $\Delta G_{\text{Exp}} = -5.3 \text{ kcal mol}^{-1}$ (Exp = experimental). [This is assuming that the transfer from monomeric aqueous to membrane aggregate form is an equilibrium process, and that the experimental result is a reflection of this.] As suggested by Grossfield *et al.*, the computed free energy can be coupled to this experimental value via a correction term that accounts for the difference in the peptide and lipid concentrations between simulation and experiment.¹²⁸

The correction term is given by:

$$\Delta G_{\text{Corr}} = \Delta G_{\text{R}} + \Delta G_{\text{Mix}} \quad (9)$$

$$\Delta G_{\text{R}} = k_{\text{b}}T \ln (\chi_{\text{sim,Peptide}} / \chi_{\text{exp,Peptide}}) \quad (10)$$

$$\Delta G_{\text{Mix}} = k_{\text{b}}T \ln (\chi_{\text{sim,lipids}} / \chi_{\text{exp,lipids}}) \quad (11)$$

where $k_{\text{b}}T$ is the Boltzmann factor. Following the notation of Grossfield, ΔG_{R} and ΔG_{Mix} are the correction terms for the peptide and lipid (respectively) concentration differences between simulation (sim) and experiment (exp). χ is the mole fraction of the species in question (either peptide or lipids). This entire correction term, ΔG_{Corr} is calculated to be $+3.0 \text{ kcal mol}^{-1}$ (see the Materials and Methods section 3.2 for further information), and must be added to the computational results.

In terms of insertion and aggregation, Figure 21 shows two paths on opposite ends of the spectrum. In the yellow path, each peptide inserts individually into the deeper membrane interface. The aggregation step then follows:

$$\Delta G_{\text{HG/C}} + \Delta G_{\text{Aggr(HG/C)}} = \Delta G_{\text{YellowPath}} \quad (12)$$

$$(\Delta G_{\text{HG/C}} + \Delta G_{\text{Corr}}) + \Delta G_{\text{Aggr(HG/C)}} = \Delta G_{\text{YellowPath}} \quad (13)$$

Equation 13 is the corrected version of equation 12, where the correction term has been added to computational result $\Delta G_{\text{HG/C}} = -10.2 \text{ kcal mol}^{-1}$. The unknown term here is the aggregation one, $\Delta G_{\text{Aggr(HG/C)}}$. If we can set $\Delta G_{\text{YellowPath}}$ to be the experimental value determined by Wimley and White ($-5.3 \text{ kcal mol}^{-1}$), the aggregation term is then calculated to be $+1.9 \text{ kcal mol}^{-1}$.

The red path in Figure 21 illustrates the opposite approach, in which individual peptides in aqueous solution first assemble, and then the whole aggregate inserts into the membrane. The first leg of this pathway is plausible and has a negative free energy change, because hydrophobic peptides in an aqueous environment are energetically more stable in aggregate instead of monomeric form.¹²⁹ Yet, the stability and energetic gain of the aggregate in solution could deter the adhesion and insertion of the aggregate into the membrane, thus making the second leg of the red path less likely. Furthermore, if the orientation of each monomeric peptide can affect the thermodynamics of the insertion process (as discussed above), it may become energetically costly for the peptide units of the complex to reorganize and assume the correct orientation. Others have also shown that transmembrane proteins do not fold entirely or form complex structures before inserting into a membrane.¹³⁰

Instead, it is more likely that a transmembrane peptide adsorbs on the membrane surface, aggregates to some extent, and then inserts into the membrane. As the insertion event proceeds, it is likely that the membrane continues to shape the peptide aggregate structure until it achieves a final stable form in the membrane host. Note that membranes exhibit the mechanical properties to do just this.³² For our model system, this is depicted in the green path, in which the monomeric peptide first adheres to the S/HG interface, aggregates, and then inserts:

$$\Delta G_{S/HG} + \Delta G_{Aggr(S/HG)} + \Delta G_{Aggr(Insert)} = \Delta G_{GreenPath} \quad (14)$$

$$(\Delta G_{S/HG} + \Delta G_{Corr}) + \Delta G_{Aggr(S/HG)} + \Delta G_{Aggr(Insert)} = \Delta G_{GreenPath} \quad (15)$$

Equation 15 represents the corrected version, with the correction term added again to the computational result, $\Delta G_{S/HG} = -8.3 \text{ kcal mol}^{-1}$. The last two terms on the left hand side of equation 15 are the unknowns, and we cannot calculate the exact contribution from $\Delta G_{Aggr(S/HG)}$ nor $\Delta G_{Aggr(Insert)}$. Again, if we equate $\Delta G_{GreenPath}$ to the experimental value of $-5.3 \text{ kcal mol}^{-1}$, the sum of these unknown terms can be calculated, $\Delta G_{Aggr(S/HG)} + \Delta G_{Aggr(Insert)} = 0 \text{ kcal mol}^{-1}$.

Thus, in the yellow path, the aggregation free energy change is positive and indicative of an unfavorable process. In other words, if the monomeric form of the peptide were to insert deep into the HG/C region of the membrane, aggregation would not be likely. In the green path however, the collective aggregation term is 0, indicating an equilibrium (and more likely) process. We have shown the following relation:

$$\{\Delta G_{Aggr(S/HG)} + \Delta G_{Aggr(Insert)}\}_{GreenPath} < \{\Delta G_{Aggr(HG/C)}\}_{YellowPath} \quad (16)$$

where the braces group the unknown terms of each path, as described above. The results suggest that the green path in Figure 21—where the peptide first adheres to the solvent-head group interface, aggregates and then inserts—more closely represents the *in vitro* mechanism of insertion and organization of WL5. Furthermore, following the previous discussion of the red path in which we stated that a formed aggregate would have difficulty inserting into the membrane, we can speculate that $\Delta G_{\text{Aggr(Insert)}} > 0$ and thus $\Delta G_{\text{Aggr(S/HG)}} < 0$. In other words, aggregation occurs immediately upon peptide binding to the membrane, in the solvent-head group region.

4.4 Conclusion

In summary, in this paper we have examined the biologically important process of peptide insertion into a membrane host, followed by aggregation and supramolecular assembly. The calculated PMF of the insertion process shows two minima, one each at the solvent-head group and hydrophilic-hydrophobic interfaces. The energetics show that aggregation and supramolecular assembly can begin immediately when the peptide makes contacts with the membrane at the first solvent-head group interfacial region. In other words, the peptide need not insert deeply and stabilize before taking on higher order structure; if it does insert deeply, the aggregation process is thermodynamically unfavorable. This implies that the membrane environment plays a direct and significant role in shaping transmembrane protein/peptide structures and is not a passive medium. Even initial contacts with the membrane can induce tertiary configuration in the protein

sequence; this induction can be attributed to the fluidity and chemical diversity of the solvent-membrane interface.

4.5 Acknowledgements

This work was supported in part by the National Science Foundation, the National Institutes of Health (GM34921), the Howard Hughes Medical Institute, the National Biomedical Computing Resource, the Keck Foundation, and the Center for Theoretical and Biological Physics.

Chapter 4, in full, is a near reprint of the material as it appears in the Journal of Physical Chemistry B 2008, Volume 112, Pages 10528-10534. This is a co-authored article. The dissertation author was the primary investigator and author of this paper. A. A. Gorfe and J. E. Kim contributed in an advisory capacity. J. A. McCammon served as the head adviser and principal investigator.

CHAPTER 5: A Virtual Screening Study of the Acetylcholine Binding Protein using a Relaxed-complex Approach

5.1 Introduction

The ligand-gated ion channels (LGIC) constitute a class of membrane proteins that function in a variety of biological processes. For instance, in signal transduction, they play a key role in the transfer of information across neurological networks.¹³¹ In the realm of disorders, these ion channels have been implicated in the onset of Alzheimer's disease and drug-addiction.^{132,133} As such, these proteins and the ligands that bind to them are of great interest in the pharmacological communities. If a binding ligand affects the activity of the channel in question, that ligand is labeled as either an agonist or antagonist. In the former case, ligand binding enhances the neurological phenomena associated with the particular ion channel. On the other hand, if an antagonist, the ligand can hinder the neurological event.¹³⁴

The nicotinic acetylcholine receptors (nAChRs) are members of the LGIC family. Upon acetylcholine (ACh) binding, the receptors assume the open-state and allow the influx of ions into the cell. This is the chemical basis of neuronal response and muscle activity.¹³⁵ As its name suggests, nicotine binds nAChR, and it does so in an agonistic

fashion, leading to increased ion flow and neuronal stimulation. This agonistic behavior of nicotine leads to patient addiction by increasing the number of high-affinity nAChR in the membrane of neurons.¹³⁶ Other drugs, such as cocaine, also bind nAChR and stimulate the receptor.¹³⁷ Thus, nAChR serves as a great pharmacological target in research on smoking-cessation and drug addiction.

Yet, to be employed in pharmacology and particularly in structure-based drug discovery, the structure of the target protein must be known to a high degree of confidence. This is usually afforded by x-ray crystallography. Yet, achieving a high resolution structure is an especially difficult feat when working with membrane proteins, whose crystallization does not occur as easily as their aqueous counterparts. The lipid environment in the membrane can greatly affect the structure of the membrane protein,¹³⁸ and it is difficult to capture this final structure via crystallography. To date, the highest resolution achieved for nAChR is a 4 Å result obtained by cryo-electron microscopy, by Unwin *et al.*¹³⁹ In this work, the pentameric structure of nAChR and the distinctive extra-cellular and transmembrane domains are resolved clearly. However, from a pharmacological standpoint, much is left to be desired regarding side chain orientations and other important conformational details.

Rather fortunately, there exists an aqueous protein that mimics the extra-cellular half of nAChR, where ligand binding occurs. This protein, the acetylcholine binding protein (AChBP), comes from three species of sea snails: *Lymnaea stagnalis* (Ls); *Aplysia californica* (Ac); and *Bulinus truncatus* (Bt).¹⁴⁰ The exact function of AChBP is unknown, although it is thought to play a role in modulating neuronal response by binding acetylcholine in synaptic clefts.¹⁴¹ Experimentally, AChBP is significantly easier

to work with in terms of expression and crystallization. To date, over a dozen structures of AChBP (with and without ligands) have been solved with high resolution.^{142,143,144,145} Although its sequence identity to the extra-cellular domain of nAChR is only roughly 30%, AChBP bears a great resemblance with respect to its secondary structure. As shown by Brejc *et al.*, the general shape of AChBP is that of a hollow cylinder with an outer, inner diameter and height of 80, 18, and 62 Å, respectively. AChBP is a homopentamer, each subunit consisting of 210 residues.

As in the extra-cellular domain of nAChR, ligands bind to AChBP at the interface between subunits; thus, with 5 subunits arranged in a cylinder, the maximum ratio of ligand:protein is 5:1.¹⁴⁶ The ligand binds in the approximate middle region of this interfacial axis, typically behind a characteristic loop extending from one of the subunits, known as the ‘C-loop’.¹⁴¹ The chemical nature of this binding site is discussed in greater detail below. Because of its great structural similarity to the ligand-binding extra-cellular domain of nAChR, AChBP has been deemed a surrogate structure of the receptor.¹⁴⁷ By targeting and identifying binders of AChBP, researchers hope to gain more understanding about nAChR. Common research themes about AChBP/nAChR focus on which ligands act as agonists or antagonists, which bind universally across all subtypes of nAChR and all species of AChBP, which ligands can distinguish between the various forms, and which can serve as leads for drug discovery efforts. Although there are marked differences between the AChBP and nAChR—most obviously, the presence of the transmembrane domain in the latter—the two proteins have enough chemical and physical similarities to warrant using AChBP as a template structure of the receptor.¹⁴⁸ Thus, only the three species of AChBP are targeted in this study, but the implications can

be far-reaching on the entire class of nicotinic acetylcholine receptors. Furthermore, what is unclear is whether or not ligand binding can occur in regions along this interfacial unit but away from the C-loop region. Can the virtual screening protocol presented here position the ligands in the traditional C-loop region as well as in novel potential binding sites? We will see that this is indeed the case.

The known ligands and various derivatives of the AChBP/nAChR systems have been extensively studied; unfortunately, many would fail as medicinal drug candidates because of their poor pharmacological properties.¹⁴⁶ The known small molecule ligands that do succeed in this light are harmful because of their addictive and abusive nature; these include cocaine, heroine, morphine and nicotine.¹⁴⁹ Thus, we are in search of new ligands that can bind AChBP and possibly play pharmacological roles in the AChBP/nAChR systems. The set through which we explore comes from the National Cancer Institute (NCI), which harbors a database of nearly 250,000 drug-like compounds. In the computational work presented here, we conduct a virtual screening study of AChBP using (as the ligand set) the National Cancer Institute Diversity Set (NCIDS)—consisting of approximately 2,000 molecules—which serves as a representative subset of the entire NCI database.¹⁵⁰ Indeed, the NCIDS ligands are novel to the AChBP/nAChR system (to the best of our knowledge) and they exhibit the desired pharmacological properties of small molecule drugs (low molecular weight, high solubility).

In any virtual screening or docking protocol, one must first determine how to obtain protein structures to dock against. One can readily employ crystal structures from the Protein Data Bank (PDB), but these static structures do not adequately depict the flexibility of the protein. Thus, docking against them does not usually reflect the true

dynamical nature of most protein-ligand interactions. Various docking protocols exist that attempt to surmount this hurdle of protein flexibility. One recent application, FLIPDOCK,¹⁵¹ attempts to achieve protein flexibility by toggling the positions of various side chains in the active site during the docking runs. This is a useful and quick way of capturing the local protein flexibility in the binding site. Yet, because of computational expense, one can only toggle a few (3 to 5) side chains, and this can be very limiting if there are many side chains implicated in ligand binding. The technique is also unfeasible if the exact binding site is unknown, or if the user intends to explore larger sites within the protein. Moreover, the application does not capture global conformational changes of the protein, and such changes could dramatically affect the binding pocket.

An alternative method in capturing protein flexibility is the relaxed-complex method, in which a molecular dynamics (MD) simulation of the target protein is first conducted.^{152,153} If the time scale of the simulation coincides with that of the protein's functional dynamics, one can capture local (and sometimes global) conformational changes in the protein. Snapshot structures can be taken from the MD simulation and employed in the screening of the ligand set using a computational docking tool. The results from these different receptor snapshots can be compared to ascertain if/how the conformational changes in the protein affect ligand binding. In the relaxed-complex scheme, there are various simulation and post-simulation processing methods that one can employ for capturing the receptor (protein) structures. As detailed by Amaro *et al.*, the simulation can consist of standard equilibrium MD or even non-equilibrium methods, such as steered MD. A variety of techniques such as principal component or root mean square deviation (RMSD) analysis can then be used to pick out snapshots. Exactly which

simulation and analysis techniques afford the best structures for docking is the subject of much debate. The ideal method probably varies from system to system; it is thus crucial to verify any technique against experimental evidence before pursuing novel endeavors. In our case, for the AChBP, we first provide such a comparison to experimental data for validation before employing the relaxed-complex scheme on the novel set (NCIDS).

Using the relaxed-complex method, we conducted MD simulations of all three species of AChBP, selected 5 snapshots from each simulation, and screened through the NCIDS for each snapshot. Given the aforementioned knowledge of the AChBP binding site, the RMSD of the characteristic C-loop that covers the binding site was chosen as the metric for snapshot selection. Specifically, through the presented work here, we address the following questions: 1. Can our relaxed-complex scheme—focusing on just one loop region—produce comparable results with previous experimental evidence (thus implicating the usage of this technique in other AChBP/nAChR systems)? 2. Can we identify new ligand binding regions within the interface of AChBP? 3. Can the NCIDS serve as a novel source of small molecule drugs targeting AChBP (and thus possibly the entire genre of AChBP/nAChR proteins)?

The results from this virtual screening protocol agree well with previous experimental evidence, particularly with respect to the predicted poses and energetic trends of the known ligand binders of AChBP. Thus, the dynamical C-loop does serve as a sufficient metric for conformational selection. The NCIDS ligands explore almost the entire subunit interface and demonstrate their propensity to bind both the C-loop and non-C-loop regions. A good number of them dock reasonably across all species and all snapshots of AChBP, and their binding interactions resemble those of known binders. All

of this suggests that the NCIDS could serve as a good set from which to pick novel ligands against AChBP/nAChR. Even more interesting is that some of the NCIDS ligands dock differently into the three species of AChBP, and these ligands could serve to distinguish between them and possibly between the various subtypes of nAChR.

5.2 Materials and Methods

From the PDB, structures for the Ls (1I9B),¹⁴¹ Ac (2BYN),¹⁴⁴ and Bt (2BJ0)¹⁵⁴ species of AChBP were obtained. All non-protein atoms were stripped from these structures. The GROMACS MD package was then used to place each protein in its own simulation box of dimensions $100 \times 100 \times 82 \text{ \AA}$, to solvate and neutralize the system with counterions, and then to carry out all subsequent MD simulations.¹⁹ Each system (3 in total) consisted of one of the AChBP species (the complete protein, as a pentamer), approximately 22,000 simple-point charge (SPC) model water molecules, and approximately 45 sodium ions. Each system totaled approximately 82,000 atoms.

Unfavorable contacts in each system were relieved by two cycles (5,000 steps each) of conjugate-gradient and steepest-descent minimizations. With the backbone of the protein restrained, each system was then heated to a temperature of 300K over a short 50 ps simulation. Pressure coupling was then added and a simulation was carried out for 1 ns with the alpha carbons of the protein restrained. The restraints were removed, and each equilibrated protein was simulated for 20 ns of production. The OPLSAA force field parameters were used for each AChBP system.¹⁵⁵ The simulation parameters consisted of the following: a 2 fs time-step; coordinates and velocities recorded at every 500 and

1,000 steps, respectively; bond length constraints were imposed using the LINCS method; full electrostatics were calculated using the particle mesh Ewald technique, with coulombic and van der Waals cut-offs of 9 and 14 Å, respectively; Ewald tolerance was set to 1×10^{-5} ; nearest-neighbor lists were updated every 10 steps, with a cut-off of 9 Å; periodic boundary conditions were employed in all directions; Berendsen temperature coupling was used across the entire system, with a coupling constant of 0.1 ps, to maintain a temperature of 300K; Berendsen isotropic pressure coupling was used across the entire system, with a reference pressure of 1.0 bar, a pressure coupling of 0.5 ps, and a compressibility of $4.5 \times 10^{-5} \text{ bar}^{-1}$. Analysis of the MD simulations was conducted using the various GROMACS tools.

For each species of AChBP, each subunit interface (there are 5 in AChBP) was examined for the greatest flexibility in the C-loop region. To reflect this flexibility, 5 snapshots of a pair of subunits forming an interface, from each species, were taken at approximately 0 (just before the production run), 5, 10, 15, and 20 ns. Thus, screening was done with $3 \text{ (species)} \times 5 \text{ (snapshots)} = 15$ AChBP receptor structures. These structures were screened against using Autodock 4.0^{156,157} and 1,834 ligands from the NCIDS, which were previously parameterized for usage in Autodock by Chang *et al.*¹⁵⁸ These $15 \times 1,834 = 27,510$ Autodock jobs were performed on a cluster of 128 processors—each 3.2 GHz EM64T with hyper threading capability, 2GB RAM—at the National Biomedical Computational Resource (NBCR).¹⁵⁹ Each receptor structure, consisting of 2 subunits that meet to make the binding interface, was prepared for docking using a script from the AutoDockTools kit that adds Gasteiger charges to the structure. Grid maps were generated, with the center of the grid placed in the middle of

the subunit interfacial axis, at a spacing of 0.375 Å and with grid dimensions of 70 × 70 × 70 points. For each Autodock job, default parameters were used with the following exceptions: the number of energy evaluations (ga_num_evals) was set to 5 × 10⁶; the root mean square deviation tolerance (rmstol) for clustering was set to 1.5 Å; and the number of dockings (ga_run) was set to 100. This scheme was used for both the NCIDS ligands and the experimental ligands discussed below. In the latter case, the ligand structures were obtained from the PDB codes indicated in Table 2 and docked back into their crystal structures. In the work presented here, the NCIDS ligands are referred to by their name (if available) or by their NCI index number (also known as the NSC number). The structure and pharmacological data of the NCIDS ligands were obtained using this NCI/NSC number, via the NCI Query system.¹⁶⁰

For any ligand, from the Autodock result, the conformation from the most populated cluster was selected as the docked ‘pose’ for that ligand; this conformation may or may not exhibit the most negative free energy of binding. Because the pose is from the most populous cluster, we take it to be the statistically-probable result. The calculated binding energy for this pose was taken to be the ‘calculated’ or ‘predicted’ free energy of binding for the ligand in question. Analysis of the Autodock results was performed using common Autodock shell scripts and several scripts written by the authors. Data was plotted using MATLAB[®]. Visualization and rendering of AChBP and AChBP-ligand complexes were completed using the Visual Molecular Dynamics (VMD) software.⁵¹ Structural alignment of the AChBP species was performed using the MultiSeq module in VMD.

5.3 Results and Discussion

We first explore the dynamics of the binding site in AChBP, which (as mentioned above) occurs in each interfacial region between any two subunits. Following previous work, the subunit depicted on the left is known as the ‘plus’ (+) face and its characteristic feature is the ‘C-loop’, a loop in the protein consisting of residues 180-190, including the characteristic vicinal cysteine residues.¹⁶¹ The subunit depicted on the right is termed the ‘minus’ (–) face. Most known binders of AChBP bind behind the C-loop in the middle of the axis in between the subunits. It has been suggested that the C-loop acts as a sort of flexible gate that covers the binding site; when a ligand binds, the C-loop becomes less flexible and covers the ligand-site complex.^{162,163} The C-loop flexibility is indeed observed in our molecular dynamics simulation as shown in Figure 22. At 5 ns intervals, one can readily observe the various positions of the C-loop. It should be noted though that this flexibility does not result in a complete opening of the subunit, for such an event does not occur on the present timescale of the simulation.¹⁶⁴ Nonetheless, one can observe that the C-loop takes on different conformations during the simulation, and the exact position of the C-loop may impact ligand binding.

Oftentimes, the accuracy of any computational docking protocol is measured against known binding ligands of a protein. Such validation is crucial for justifying the current docking method. In our case, we seek to ensure the validity of selecting conformations based on the flexibility of one simple loop (the C-loop) in a rather large protein. Fortunately, for AChBP, there are many solved structures of ligand-receptor complexes in the PDB. The ligands of these complexes were docked back into AChBP;

the results are shown in Table 2 and Figure 23. In most cases, Autodock is fairly accurate in predicting the pose of the ligand, especially in the case of the well-known binders epibatidine and nicotine, whose docked poses exhibit less than a 1 Å RMSD from the crystal structure. It is well-documented that the smaller ligands of AChBP bind more rigidly behind the C-loop in between the two interfaces.¹⁶⁵

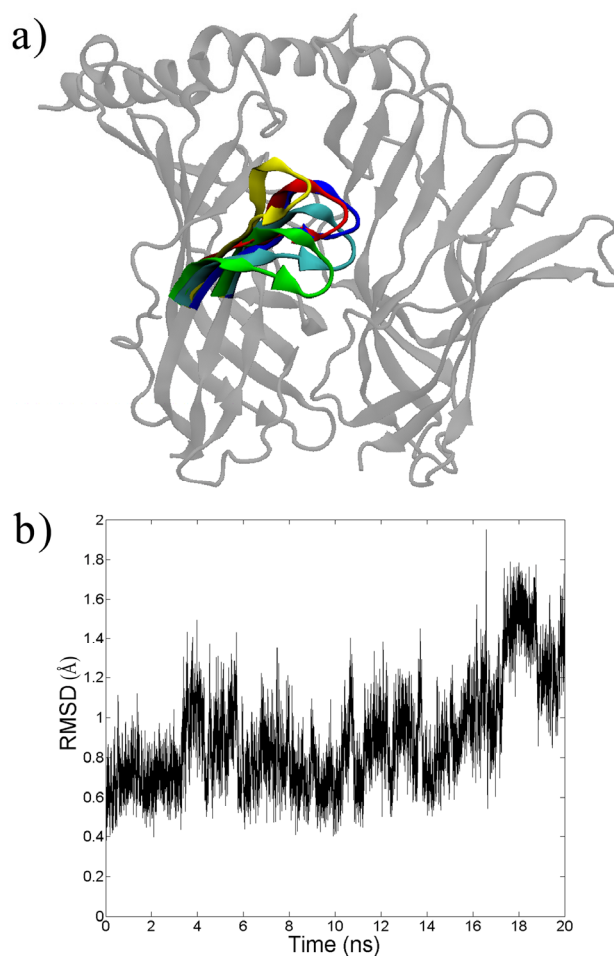


Figure 22: a) Snapshots from the molecular dynamics simulation of the acetylcholine binding protein (species *Aplysia Californica*, PDB: 2BYN). Only 1 of the 5 interfaces is shown here for clarity. The C-loop is colored in 5 ns increments. b) The average root mean square deviation (RMSD) of the C-loop (C_α carbons only) as a function of simulation time.

As the ligands increase in size and in the number of rotatable bonds, the RMSD between docked and crystal structures increases, as can be seen in the cases of lobeline and cocaine. One suspects that the lobeline result is more accurate than the cocaine because the former exhibits a more symmetrical (or ‘butterfly’) structure, which possibly aids the lobeline in fitting along the interfacial axis between the subunits of AChBP. We discuss below ligands from the NCIDS that exhibit this same behavior. In the case of cocaine, its bulkiness and size possibly preclude a better predicted pose. In the case of the even larger ligands—pentaethylene glycol (several rotatable bonds) and methyllycaconitine (a macrocyclic structure)—the pose accuracy is even worse ($> 5 \text{ \AA}$ RMSD).

Table 2: A comparison of the docked and experimental results, with respect to the pose accuracy of the ligand. The first column is the PDB ID of the ligand-AChBP complex, the second column is the full name of the ligand, followed by the ligand code (in the third column) as found in the PDB. The last column of the table shows the root mean square deviation (RMSD, in \AA) of the docked ligand as compared to the crystal structure.

PDB	Ligand Name	Code	RMSD
2BYQ	Epibatidine	EPJ	0.5
1UW6	Nicotine	NCT	0.7
2UZ6	Alpha-Conotoxin	-	0.9
2BJ0	3-Cyclohexyl-1-propylsulfonic Acid	CXS	1.1
2BYS	Lobeline	LOB	1.3
1UV6	2-[(Aminocarbonyl)oxy]-N,N,N-Trimethylethanaminium	CCE	1.4
2BR7	4-(2-Hydroxyethyl)-1-Piperazine Ethanesulfonic Acid	EPE	1.9
1I9B	"	EPE	2.8
1UX2	"	EPE	7.7
2PGZ	Cocaine	COC	3.8
2BYN	Pentaethylene Glycol	1PE	6.0
2BYR	Methyllycaconitine	MLK	8.0

Such problems in dealing with large rotatable ligands are common when using Autodock and other docking codes.¹⁶⁶ Nonetheless, though the exact poses are off for these ligands, Autodock does place them in the general vicinity of binding (behind the C-loop) along the subunit interface, and this placement agrees well with previous experimental evidence.¹⁶⁷

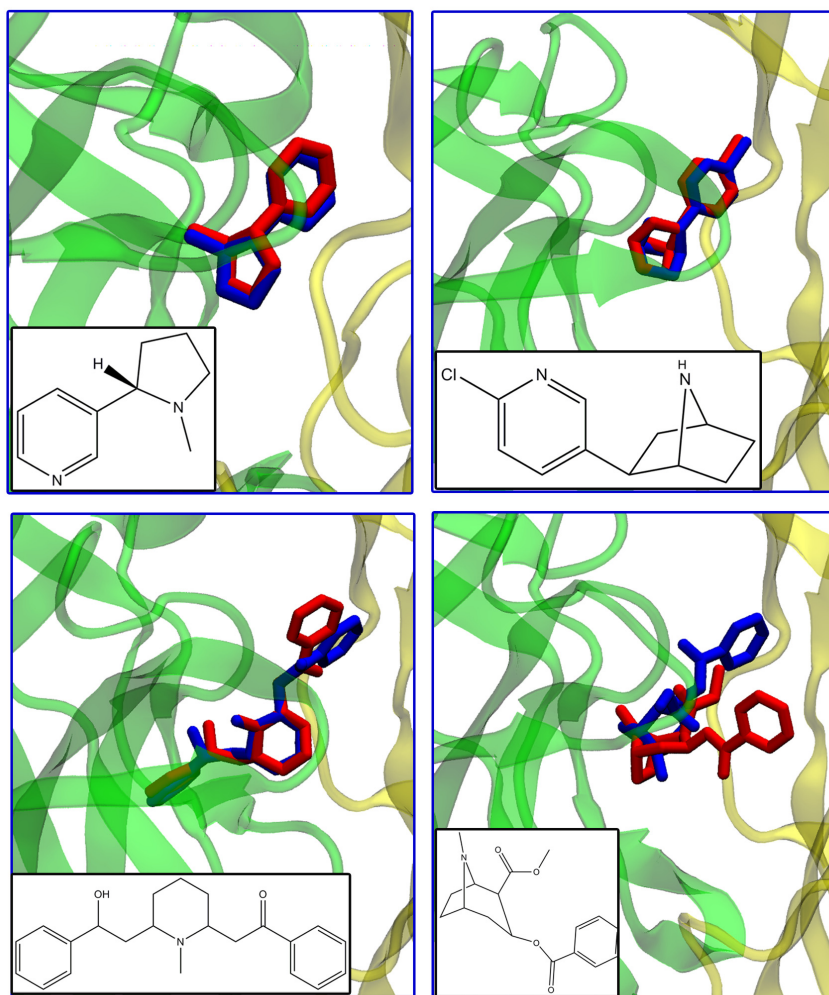


Figure 23: Docked (blue) vs. crystal (red) structures of some common ligands that bind the acetylcholine binding protein. Top Left: Nicotine, Top Right: Epibatidine, Bottom Left: Lobeline, Bottom Right: Cocaine.

Regarding the accuracy of the calculated free energy of binding, the current docking protocol does not predict with great accuracy the actual free energy as compared to experimental evidence,^{144,146,147,168} but it does pick up on some key trends; see Figure 24. For instance, both experimental and computational results show nicotine binding better (a more negative free energy change) than the natural ligand of AChBP, acetylcholine. Although the docking does not show epibatidine to be the best binder, it does correctly show that epibatidine binds better than nicotine. The predicted free energy of binding seems to be more accurate in the larger ligands (cocaine, D-Tubocurarine, metocurine). A slight trend is also observed between the molecular weight and the calculated free energy of binding, in the sense that the larger ligands tend to bind more favorably (see Figure 25). Given the large binding space afforded by the subunit interface, it is not surprising that the calculated energies for the larger ligands are more accurate. In any case, it stands to reason that more emphasis should be placed on the predicted trends rather than the absolute binding energy numbers. Thus, because the energetic trends and docked poses agree fairly well with previous experimental results, we have confidence that the relaxed-complex scheme presented here—where we select and dock against various conformations of the C-loop—can be employed in the search for novel ligands.

It is interesting to note that the predicted binding energies of the NCIDS ligands cluster in the same key range as the known ligands of AChBP; see Figure 26. For the purposes of this study and because of the known calculated noise associated with Autodock,¹⁵⁸ we will focus on those ligands with a predicted binding energy near or less than $-7.0 \text{ kcal mol}^{-1}$. Although we do not yet have experimental results of the NCIDS

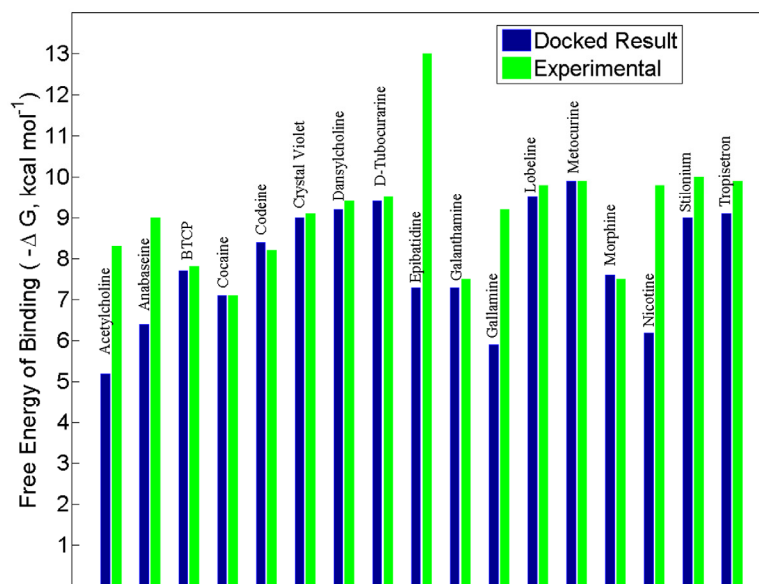


Figure 24: A comparison of the Autodock calculated free energies of binding with experimental values, of known binders to the acetylcholine binding protein (Ls species). For the docked value, the best result was selected from the snapshots afforded by the relaxed-complex method. Experimental values for BTCP (N-[1-(2-benzothiophenyl)cyclohexyl]piperidine), codeine, crystal violet, morphine, stilonium, and tropisetron were obtained via personal correspondence with Talley. All other experimental values were obtained from references 144, 146, 147, 168.

ligands against AChBP, the computational work presented here is very promising, in the sense that the novel set mimics the binding of known compounds. Furthermore, because the docking was conducted throughout the entire interfacial region, the NCIDS ligands bound to several residues along the axis between the two AChBP subunits; see Figures 27 and 28. While many docked into the traditional C-loop binding region, what is striking is that many of the NCIDS ligands explored the remaining interfacial space, suggesting the prevalence of new binding sites and modes. We discuss below both the C-loop and non-C-loop binding regions.

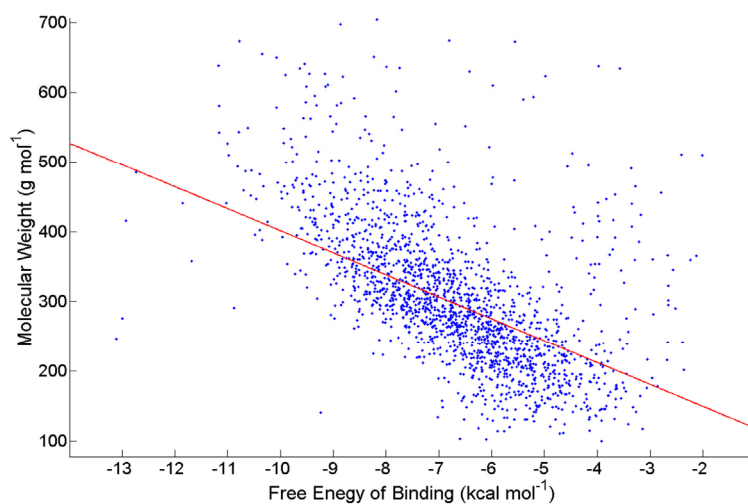


Figure 25: Molecular weight vs. the calculated free energy of binding, of the NCIDS ligands against the 10 ns snapshot of Ls AChBP.

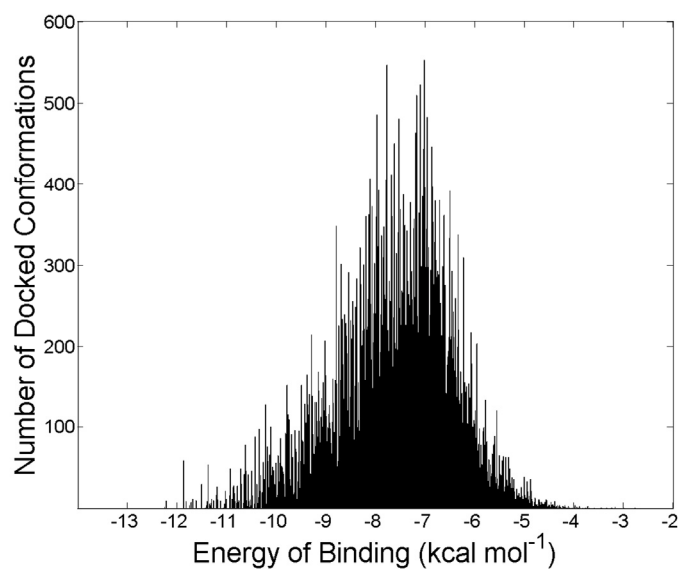


Figure 26: Free energies of binding of all docked conformations of the NCI Diversity Set against the 0 ns snapshot of the Ls AChBP.

As expected, the ligands make a significant number of contacts with and around the C-loop region of the plus face (residues 180-200). Those ligands that bind well in this region do so with respect to all three species of AChBP. Appendix A-1 displays a list of

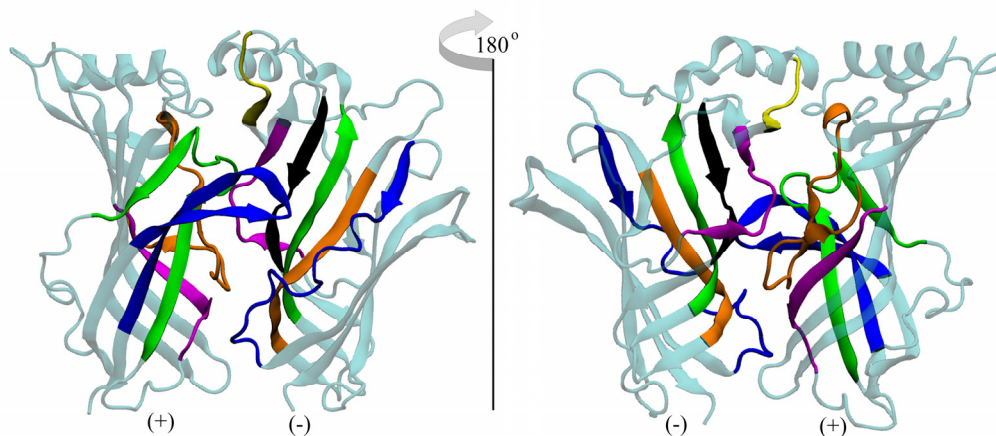


Figure 27: Front and rear views of the binding (interfacial) site. The subunit containing the C-loop is often termed the ‘plus’ (+) face, while the adjacent subunit is the ‘minus’ (-) face. All colored regions show significant contact with the ligands of the NCI Diversity Set. The frequency profile of contacts can be seen in Figure 28. Plus face: orange corresponds to residues 80-100, pink to 115-125, green to 135-155, blue to 180-200. Minus face: orange corresponds to residues 30-40, green to 50-60, yellow to 70-75, pink to 95-105, black to 110-118, and blue to residues 150-170.

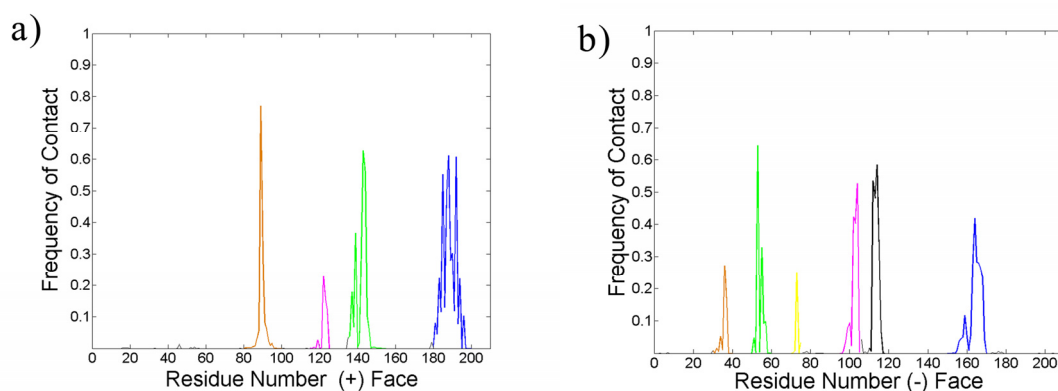


Figure 28: The frequency of contacts (within 5 Å of a residue) between all of the ligands of the NCI Diversity Set and the acetylcholine binding protein. Coloring scheme matches that of Figure 27.

compounds from the NCIDS that bind to all three species and across all snapshots of the protein. These ligands should not distinguish between the three species of AChBP because they all bind in a similar fashion behind the C-loop. The 50 compounds listed in Appendix A-1 that dock across all three species and behind the C-loop exhibit the same characteristics of previous known binders of AChBP. 19 of them (almost half) bear a tryptophan-like moiety, and this structure provides a key point of stabilization in the C-loop region. In this region of the protein, an ‘aromatic cage’ stabilizes ligands that contain aromatic functionalities.¹⁶⁹ This cage consists of several key tryptophan and tyrosine residues, and they are observed to make stabilizing contacts with the docked NCIDS ligands as well. An example of this interaction can be seen in Figure 29. Several of the NCIDS compounds that bind all three species and snapshots of AChBP contain amines that can bear a charge depending on the pH of the environment. In turn, these charged amines can interact with the electronic π networks of the aromatic amino acids, and these cation- π interactions also serve to stabilize the ligand in the AChBP binding pocket.^{145,170} That a significant number of the NCIDS ligands exhibit groups that can hold a charge and contain aromatic functionalities that can interact with the aromatic cage makes the NCIDS a practical pool from which to pick novel ligands against all species of AChBP.

Hydrogen bonds also play a role in stabilizing the AChBP-ligand complex.¹⁶³ Backbone atoms on the protein and key side chains (such as tryptophan and tyrosine) can make hydrogen bonds with the ligand.¹⁵⁴ The NCIDS compounds also exhibit several hydrogen bonding moieties. Along with amines, many bear several hydroxyl groups in key positions that can help stabilize the ligand in the binding site. A prime example is

NCI 108608, as shown in Figure 30. This ligand contains all of the aforementioned characteristics, including a tryptophan-like structure, amines, and several hydroxyl groups. It forms close contacts with at least two residues of the C-loop region on the plus face (CYS187 and TYR192), a third residue characteristic of the aromatic cage (TRP143), and a residue on the minus face (LEU102). These interactions coupled together could make this ligand a strong binder against all three species of AChBP.

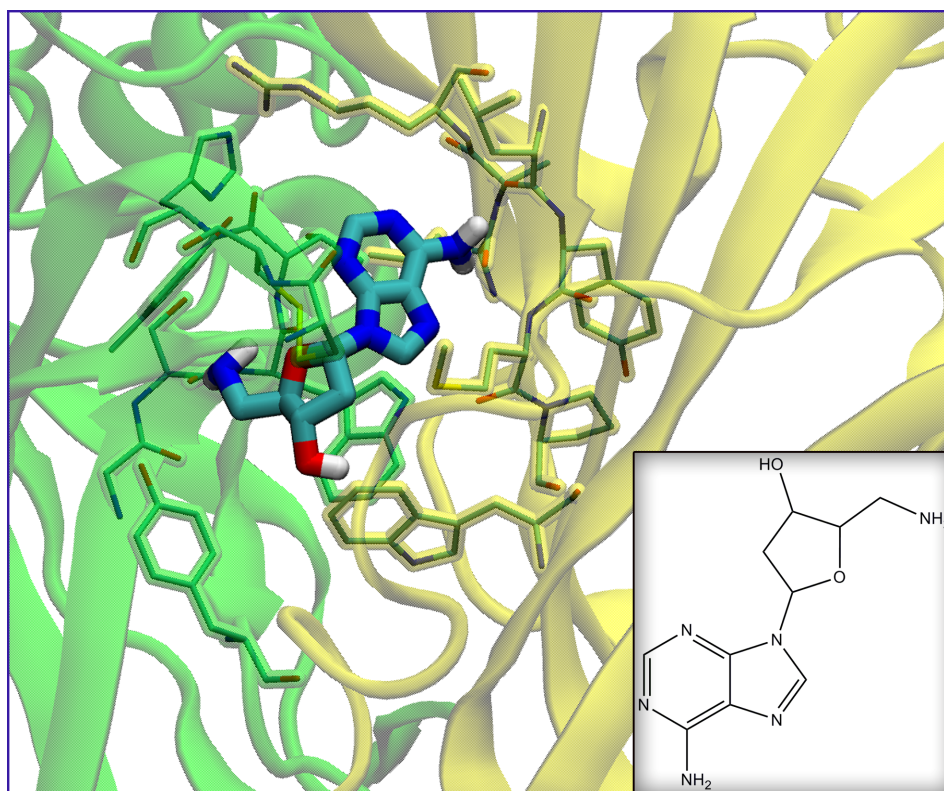


Figure 29: NCI 105017, binding against Ls AChBP. The plus/minus faces of the binding site are colored green/yellow, respectively, and shown in the cartoon representation. Some of the protein residues from each face that make up the 'aromatic cage' are shown in a highlighted stick representation. The ligand is shown in the licorice model, where the atoms of the ligand are colored cyan, red, white, and blue, for carbon, oxygen, hydrogen, and nitrogen, respectively. Inset shows the 2D structure of the ligand.

If the ligand binds behind the C-loop in the interfacial region of AChBP, then the C-loop conformation itself plays a significant role in stabilization. For instance, in the binding of large ligands such as the conotoxins, the C-loop is usually extended outward and away from the cylindrical space of AChBP. On the other hand, when binding smaller ligands such as epibatidine, the C-loop is bent inwards and more towards the central axis of the protein.¹⁶⁸ Based on this knowledge and the various poses of the C-loop afforded by the relaxed-complex scheme presented here, we can qualitatively judge the fidelity of a pose for a new ligand. We see that for the NCIDS ligands that do bind in the C-loop

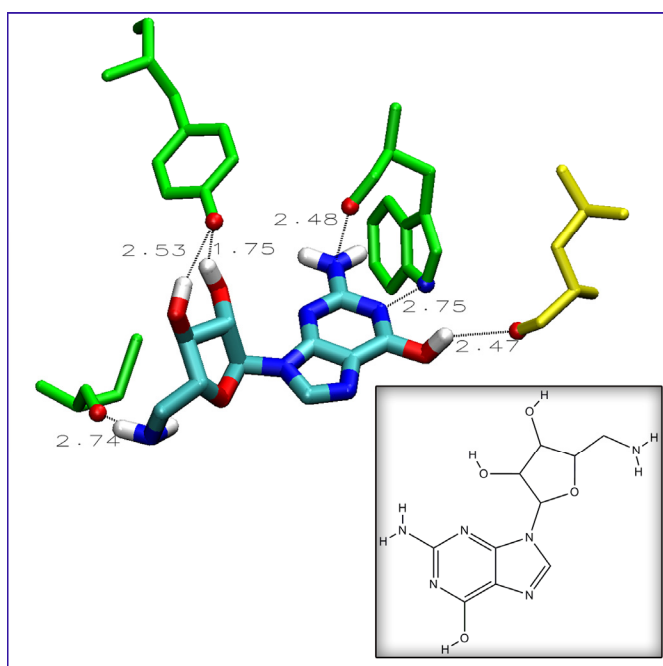


Figure 30: The extensive hydrogen-bonding character of NCI 108608, to the *Lymnaea stagnalis* species of AChBP. Numbers indicate distances in angstroms. Residues from the plus face of AChBP are shown in green, and they are (from the left) CYS187, TYR192, and TRP143. The yellow residue is LEU102 and from the minus face. The hydrogen bonding atoms on the protein residues as well as the atoms of the ligand are colored cyan, red, white, and blue, for carbon, oxygen, hydrogen, and nitrogen, respectively. Inset shows the 2D structure of the ligand.

region, the ligand pose depends significantly on the position of the C-loop; see Figure 31. It appears that as the C-loop moves away from its characteristic position, the conformation of the ligand is altered (middle and bottom panels of Figure 31a). We have not explicitly explored such dynamics here, but recent computational work by Liu *et al.* has shown that the dynamics of the C-loop and the ligand position are inherently tied to each other.¹⁶⁴ For ligands that bind well across all three species of AChBP, we take the predicted pose with the C-loop in the traditional position (as shown in the crystal structure) to be the most probable pose of that ligand.

Some of the NCIDS compounds are also reminiscent of the recently-studied neonicotinoids that bind well to AChBP.¹⁷¹ NCI 348401 (shown in Figure 31), 118208, and 116805 bear a resemblance to the neonicotinoid imidacloprid, in the sense that they harbor nitro groups that can form hydrogen bonds with key residues in the C-loop of the plus face. Similar to desnitroimidacloprid, NCI 22959 contains imines and amines that can stabilize the ligand in the C-loop region. As Talley *et al.* point out, these nitrogenous functionalities form key hydrogen bonds and (if charged) cation- π interactions with the residues of the binding site.¹⁷¹ Thus, the ligands from the NCIDS that contain these imines and amines—as well as those that exhibit properties of typical C-loop binders—may become novel AChBP-binding ligands.

As mentioned above, a significant number of the NCIDS compounds consistently bind away from the C-loop region, in all three AChBP species. By visual inspection, these compounds seem to be ‘butterfly’ structures, in the sense that they exhibit identical (or near-identical) structures on either side of a point of symmetry. Of the list in

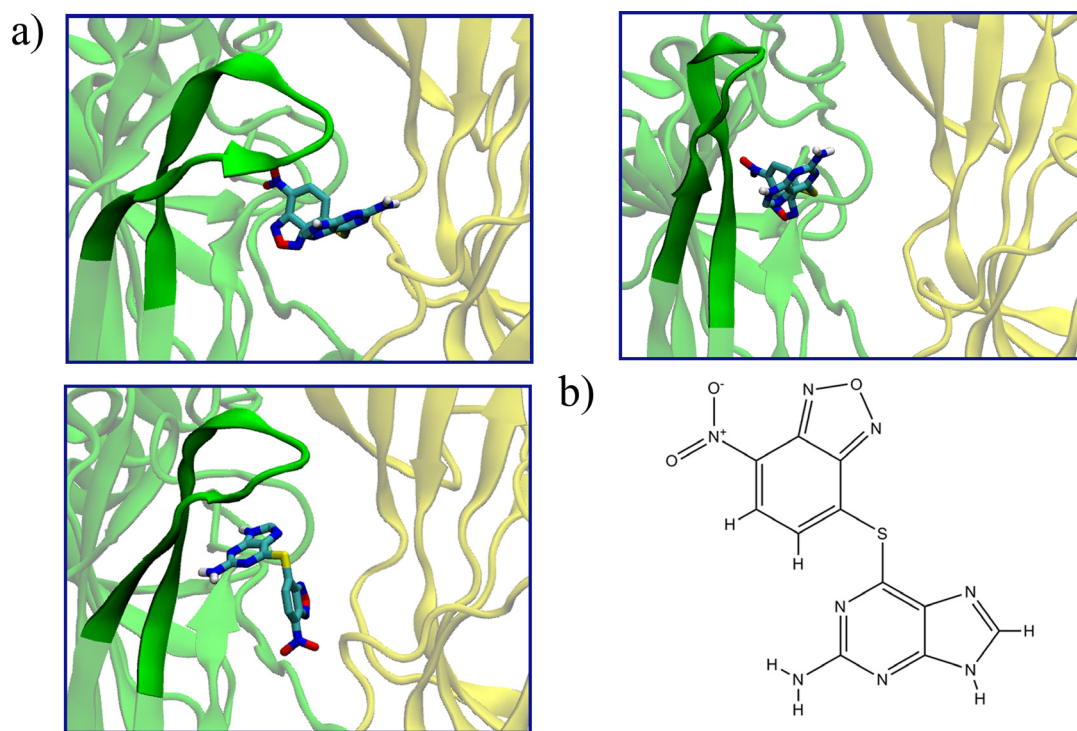


Figure 31: a) Binding of 2-amino-6-((7-(hydroxy(oxido)amino)-2,1,3-benzoxa-diazol-4-yl)thio)-9H-purine (NCIDS 348401) to the *Aplysia californica* species of AChBP, at different conformations of the C-loop. The plus/minus faces of the protein are shown in a cartoon representation in green/yellow, respectively, and in a transparent fashion except in the region of the C-loop (opaque). Ligand is shown in the licorice representations, with atoms colored cyan, red, white, and blue, for carbon, oxygen, hydrogen, and nitrogen, respectively. b) The 2D structure of the ligand.

Appendix A-1, a handful of compounds (NCI 54671, 54672, 116805, and 282034) exhibit this property. As can be seen in Figure 32, 5-(2-(1H-tetrazol-5-yl)ethyl)-1H-

tetraazole (NCI 282034) docks in a deeper pocket on the plus face, too distant to form significant contacts with the C-loop residues. These butterfly compounds can bind into other crevices along the plus/minus interface, but their effect on either the conformation or chemistry of AChBP is unclear and warrants further work. In general, such butterfly compounds are versatile and have proven of interest in other pharmacological targets, such as HIV Integrase.¹⁷² Given the large interfacial area between the subunits of AChBP, the present docking method utilizes these butterfly compounds from the NCIDS to explore the binding space.

That the NCIDS ligands make significant contacts (see Figures 27 and 28) with parts of the plus/minus faces away from C-loop region suggests that parts of the interface above and below the C-loop may play a role in ligand binding. From the plus face, these other regions of binding are the A-loop region (residues 80 to 100), the β -strand (residues 115 to 125) following the E-loop region, and the B-loop region with accompanying β -strands (residues 135 to 155). The letter designations of the loops comes from previous work.¹⁶¹ On the minus face, the various β -strands (residues 30 to 40, 50 to 60, and 110 to 118) stabilize the ligand when in the traditional binding site, behind the C-loop. Yet, we observe that some other parts of the minus face—in particular the F-loop region (residues 150 to 170)—may also provide binding residues.

Work by Hibbs *et al.* demonstrated that agonists and antagonists of AChBP have different effects on the flexibility of the F-loop upon ligand binding, and that this flexibility may result in a conformational change that is translated down the membrane portion in the actual acetylcholine receptor.¹⁷³ Given the significant frequency of contacts with the F-loop region (see Figure 28b), the NCIDS ligands may elucidate this point

further. The strands preceding the A-loop region (residues 95-105) and even a piece of the interface at the top (residues 70-75) of the minus face may also be implicated in

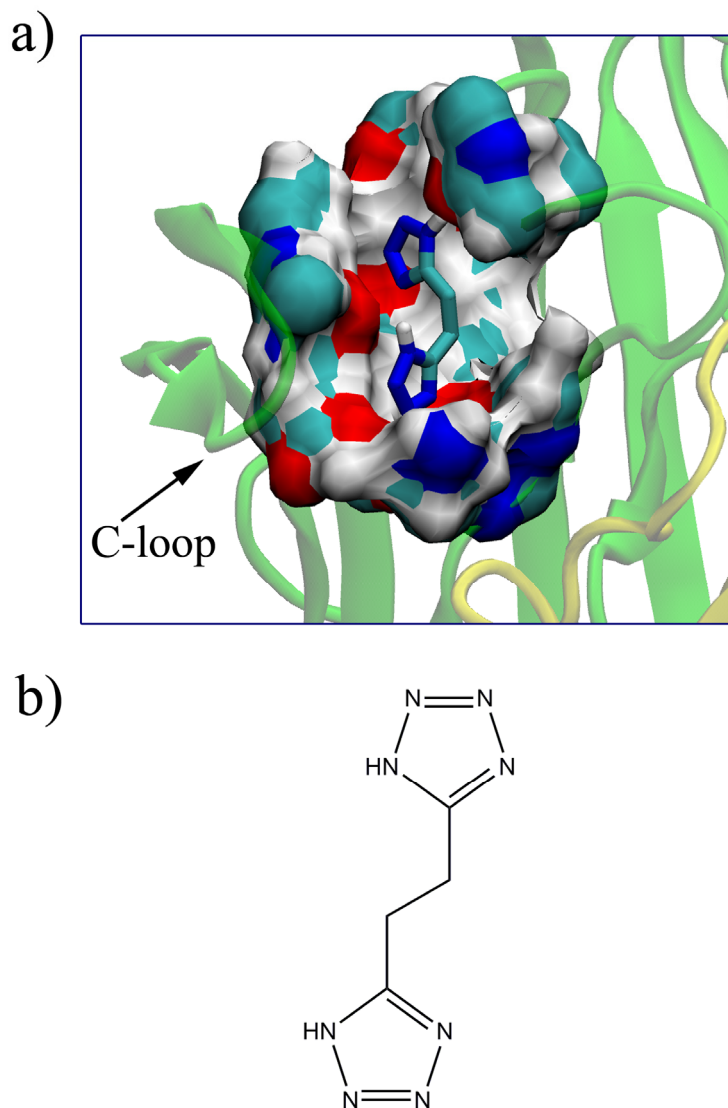


Figure 32: a) 5-(2-(1H-tetraazol-5-yl)ethyl)-1H-tetrazole (NCI 282034) docked in Ac AChBP. Binding pocket of the protein is shown in a space-filling representation while the ligand is shown in the licorice mode. The coloring scheme for the atoms is cyan, red, white, and blue, for carbon, oxygen, hydrogen, and nitrogen, respectively. b) The 2D structure of the same ligand.

binding. Because of the vast work on the binding in the traditional C-loop region, it is debatable how strongly ligands may bind to these other regions of the plus/minus interface. Yet, computationally, there is no reason to exclude these other interfacial regions. In fact, the work presented here suggests that it would be erroneous to discount the binding to the non-C-loop regions. Furthermore, recent experimental (unpublished) data by Talley also implicates these non-C-loop regions in ligand binding (although the exact properties of such ligands have yet to be determined).

It is also interesting to note that the NCIDS ligands that do bind to other parts of the plus/minus interface bind differently amongst the three species of AChBP. Appendix A-2 shows a subset of the NCIDS that bind differently across the 15 snapshots of AChBP (5 from each species). One such ligand, Tolypomycin (NCI 117383) is shown in Figure 33. It is a macrocyclic molecule, bearing some resemblance to the curariform antagonists that bind to AChBP in a variety of orientations.¹⁷⁰ In the three species, the Tolypomycin docks in the interfacial regions below, behind, and above the C-loop in the Ls, Ac, and Bt forms of AChBP, respectively. As discussed previously, because binding behind the C-loop region is the most stable form of binding, it is likely that Tolypomycin would bind better to Ac AChBP than to the other two species. In this sense, some of the ligands of the NCIDS could possibly be used to differentiate between the three species of AChBP and between the different subtypes of nAChR.

Some interesting characteristics of the Tolypomycin binding are revealed by comparing the sequences of the plus/minus faces in the three species. In the plus face (Figure 34a), the sequence conservation of the C-loop region is great across all three

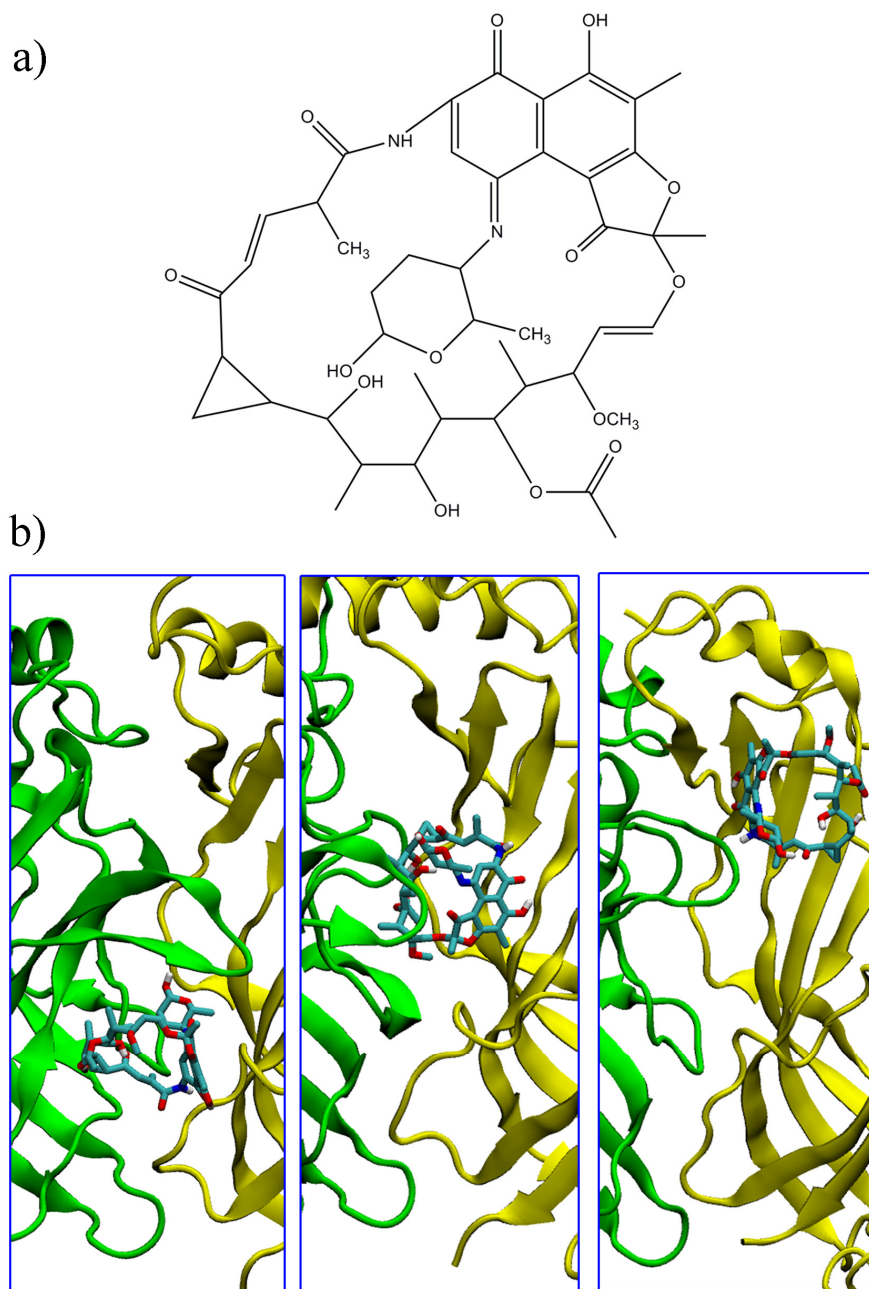


Figure 33: a) 2D Structure of Tolypomycin (NCI 177383). b) Binding of Tolypomycin to the three species of AChBP. From left to right: *Lymnaea stagnalis*; *Aplysia californica*; *Bulinus truncates*. In each case, the plus/minus faces are shown in a cartoon representation in green/yellow, respectively. Ligand is shown in the licorice representations, with atoms colored cyan, red, white, and blue, for carbon, oxygen, hydrogen, and nitrogen, respectively.

species of AChBP. Tolypomycin makes contacts here with the conserved tyrosine-serine-cysteine-cysteine (YSCC) sequence in all three species. This again demonstrates that the C-loop region of the plus face is the ideal location for binding, and many of the NCIDS ligands resolve this point. Just upstream from the C-loop region, Tolypomycin makes contact with conserved tyrosine and aspartic acid residues.

a) (+) Face

```

Ls... (84) PDLAAY*N*AI*SKPEVLT*PQL(102) ..... (120) RF*SC*DV*SGVDTE*SGATC*R*I*IG*ST*THHSRE(149) ...
Bt... (83) PDL*SFYNAIAAPE*L*L*SAD(100) ..... (115) SQRV*RF*TC*DLINVDTE*PGATC*R*IKV*GSW*THDNKQ(148) ...
Ac... (93) TP*D*ITA*SS*TRPV*QV*LS*PQI(112) ..... (127) QRLS*FMCDPTG*VDSEEGATCAV*FG*SW*VY*SG*FF(159) ...

Ls... (172) EILD*V*TQ*K*NS*VTY*SC*PEAYE*D*VE*VSLN*FRK(203) ...
Bt... (171) DLL*SATQ*SLN*RK*K*Y*SC*EN*MY*DD*IE*ITFA*FRK(203) ...
Ac... (180) YEIL*SATQ*TRQ*VQH*Y*SC*PE*PI*I*VN*LV*VK*FRER(213) ..

```

b) (-) Face

```

Ls..... (25) R-PVA*VS*VSL*K*FI*N*I*LEV*NEIT*NEVD*VVF*W*Q*TT*WSD*R*T*LA--WNSSHS--PDQ*VS*VP*ISS*LW*V*PD(85) ...
Bt..... (25) LN*V*SL*N*FK*LMN*I*VEAD*TEK*DQ*EV*V*L*WT*Q*AS*WK*VE*YY*SL*IS-S-S-SL*DQ*V*SL*PV*SK*M*W*TP*DL(85) ...
Ac(25) YPG*PT*KDD*PL*TV*TI*G*FT*LC*DIV*KAD*SS*TNE*V*DL*VY*EQ*QR*W*KL*NS*LM--WDP*NEY*GN*IT*DF*IT(85) .....

Ls..... (95) PEV*L*TP*QLAR*VV*SD*GE*VLY*PS*IR*QR(120) ..... (155) TTE--NS*D--SEY*FS*OY*S*RF*E*I*LD*V*TQ*KK(180) ...
Bt..... (95) ELL*SADR*V*V*SK*DG*SV*IY*V*PS*QR*VR*F(120) ..... (150) AL*IT*CE*EG*V*VNI*-AEY*FD*SP*-KFD*LL*SAT*Q*SLN(180) ..
Ac... (100) STR*PV*QV*LS*EQ*IA*V*TH*DG*SV*MF*IPA*Q*RL*SF(130) ..... (160) DLK*T*DT*D--Q*VD*L*SS*Y*ASS*KYEIL*SAT*Q*TR(188) ...

```

Figure 34: Structural sequence alignments of the AChBP in the a) plus face and b) minus face. The top, middle and bottom rows correspond to the species *Lymnaea stagnalis* (Ls), *Bulinus truncatus* (Bt) and *Aplysia californica* (Ac), respectively. Asterisks delineate points of structural sequence conservation throughout all three species. Highlighted residues are those that make contacts (within 7.5 Å) with the ligand Tolypomycin, shown in Figure 33.

Contacts occur at some other conserved sites as well but not always across all three species of AChBP. For instance, Tolypomycin makes contact with TYR89 and TYR99 of Ls and Ac AChBP, respectively; but no such contact is made with the conserved TYR88 of Bt AChBP. The ligand also makes contacts with the conserved cysteine and aspartic acid residues of Ls AChBP but not with Bt or Ac AChBP. Slight differences in secondary structure at these conserved sites may result in differences in binding for a particular ligand. Moreover, certain strands of contact occur in some species but not in the others, such as the contacts from SER152 to GLU159 in Ac AChBP. This is even more the case in the minus face (Figure 34b), where the contact pattern differs greatly from one species to the next. Here one can see that the strands of contacts are not always aligned, and sometimes a long strand of contacts occurs in one species but to a lesser degree in the other two. These points of contact differentiation between the three species could explain the differential binding of Tolypomycin (as well as the other ligands in Appendix A-2) to AChBP.

5.4 Conclusion

We have presented here a virtual screening study of the acetylcholine binding protein using the relaxed-complex method which involves a combination of MD simulation (to sample receptor structures) and docking. Regarding the ligands that bind AChBP—although the exact binding energies and poses are not always predicted—the relaxed-complex method does provide accurate results for many of the known binders and highlights key binding trends. Even the simple method of receptor structure selection

based on the RMSD of a single loop can afford these results; this is likely the case for the entire realm of AChBP/nAChR proteins.

The ligands of the National Cancer Institute Diversity Set were screened through, and the results show that a number could serve as potential binders of AChBP. Like the known binders of AChBP, many of the NCIDS ligands dock behind the C-loop along the interface formed between the plus and minus subunits. This is the traditional location of ligand-binding in AChBP. The NCIDS ligands that possess aromatic functionalities are stabilized in the C-loop region by an aromatic cage. Hydrogen bonding interactions are prevalent; the ligands also feature chemical moieties that can bear a charge and thus form cation- π interactions with the residues in the binding site. Although many of the NCIDS ligands dock well across all three species and snapshots of AChBP, some appear to distinguish between the various structures. When this is the case, the ligands dock away from the C-loop region, and these molecules could serve to distinguish between the three species of AChBP. In this way, the NCIDS ligands have identified potentially-novel binding regions in the interfacial space of the protein.

Thus, the chemical space of the NCIDS provides valuable insight into ligand-binding in the acetylcholine binding protein. Because of its functional and structural similarity to the extra-cellular domain of the nicotinic acetylcholine receptor, AChBP serves as a surrogate structure in the study of the receptor. The ligands that interact significantly with AChBP could in turn bind the receptor. If this is the case, the NCIDS could be probed for ligands that bind across all of the receptor subtypes as well as those that distinguish between different structures. Such novel ligands could be helpful in pharmaceutical research on various neurological processes and disorders.

5.5 Acknowledgements

This work was supported in part by the National Science Foundation (Grants MCB-0506593 and MCA93S013), the National Institutes of Health (GM34921), the Howard Hughes Medical Institute, the National Biomedical Computing Resource, the Keck Foundation, and the Center for Theoretical and Biological Physics. We thank Dr. Rommie Amaro for assistance in setting up the virtual screening protocol. We also thank Dr. Wes Goodman and Dr. Wilfred Li at NBCR for their invaluable computing support.

Chapter 5, in full, is a near reprint of the material as it appears in *Computational Biology and Chemistry* 2009, Volume 33, Pages 160-170. This is a co-authored article. The dissertation author was the primary investigator and author of this paper. T. T. Talley and P. Taylor contributed in an advisory capacity. J. A. McCammon served as the head adviser and principal investigator.

CHAPTER 6: Inhibitor Binding of Group IVA Phospholipase A₂ Probed by Molecular Dynamics and Deuterium Exchange Mass Spectrometry

6.1 Introduction

The Group IVA phospholipase A₂ (GIVA PLA₂) is a member of the superfamily of phospholipase A₂ enzymes that cleave a fatty acid from the sn-2 position of phospholipids.^{174,175} The products of this reaction, a free fatty acid and a lysophospholipid play important roles as lipid second messengers. GIVA PLA₂ was isolated in 1990 from U937 cells,¹⁷⁶ and was discovered to be composed of a C2 domain, and a α/β hydrolase domain containing the active site.¹⁷⁷ The GIVA PLA₂ is specific for phospholipids with arachidonic acid in the sn-2 position, and the release of arachidonic acid is the first step in the production of eicosanoids and leukotrienes which play important roles in many inflammatory diseases.¹⁷⁸ Experiments performed using mice deficient in the GIVA PLA₂ enzyme have proven that GIVA PLA₂ is the critical PLA₂ enzyme for eicosanoid generation in many inflammatory disease models.^{179,180,181}

The enzyme was shown through site directed mutagenesis to contain an active site dyad composed of Ser-228 and Asp-549,¹⁸² and this was later confirmed through x-ray crystallography of the enzyme.¹⁸³ The enzyme contains an amphipathic lid region from 415-432 that prevents accession of phospholipid into the active site.¹⁸³ The lid region has

two disordered regions from 408-412, and 433-457 that may act as hinges that allow the lid region to open. It has been shown that this lid is in the open conformation when the enzyme is in the presence of lipid vesicles (its natural substrate) or when inhibitor is bound in the active site.

The knowledge that GIVA PLA₂ plays an important functional role in many inflammatory diseases has sparked an interest in the production of specific inhibitors against this enzyme. The first inhibitors of this enzyme were based around the specificity of the enzyme for phospholipids with arachidonic acid in the sn-2 position, and as such arachidonyl trifluoromethyl ketones (ATK) and methyl arachidonyl fluoro phosphonate (MAFP) (**1**) were synthesized and found to inhibit the enzyme in platelet models of eicosanoid generation.^{184,185,186} In recent years many different strategies have been pursued to create effective and specific GIVA PLA₂ inhibitors. These have included indole derivatives developed by Wyeth Pharmaceuticals (**2**),^{187,188,189,190} pyrrolidine based inhibitors by Shinogi Pharmaceuticals (**3**),^{191,192,193,194} substituted propan-2-ones by the Lehr group,^{195,196,197} as well as 2-oxoamide compounds by the Kokotos and Dennis groups (**4**) as shown in Figure 35.^{198,199,200,201} Of these inhibitors, there exist two docked structures in the GIVA PLA₂ active site, generated through computer modeling,^{187,202} but there are no in depth examinations of the binding pocket contacts between inhibitor and enzyme.

The pyrrolidine derived inhibitor pyrrophenone displays some of the best inhibition but (due to chemical properties) is not useful as a drug.¹⁹⁰ We have previously shown that the 2-oxoamide compounds show an antihyperalgesic effect in rat models.²⁰³ The invention of better 2-oxoamide inhibitors is a promising drug strategy, and to such

end, we set out to model the 2-oxoamide inhibitor AX007, as well as the pyrrolidine derived inhibitor pyrrophenone, bound in the active site. This required a technique to monitor changes in protein structure upon inhibitor binding.

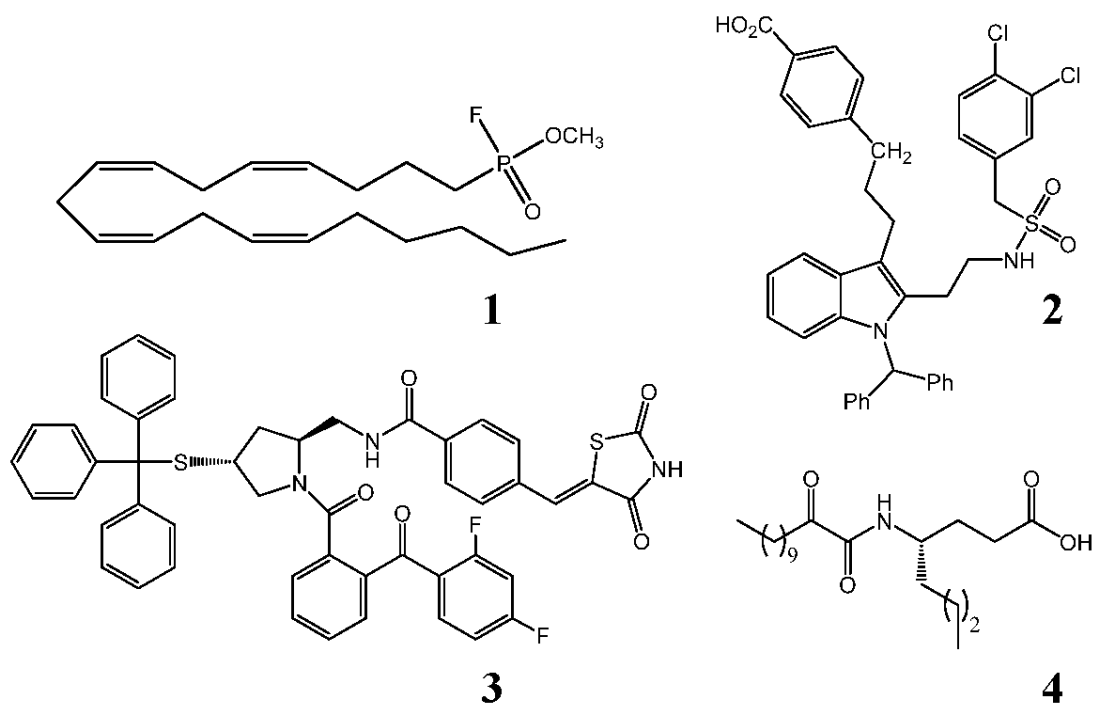


Figure 35: Inhibitors of GIVA PLA₂. 1. MAFP. 2. Efipladib. 3. Pyrrophenone. 4. AX007

Peptide amide hydrogen deuterium exchange analyzed via liquid chromatography-mass spectrometry has been widely used to analyze protein-protein interactions,^{204,205} protein conformational changes,^{206,207} and protein dynamics.²⁰⁸ We have previously used this technique to explore changes in lipid binding with the GIVA PLA₂ and discovered changes in exchange profiles in the presence of the irreversible inhibitor MAFP.²⁰⁹ The DXMS technique, in conjunction with site-directed mutagenesis, has recently been used to identify regions interacting with different inhibitors.^{210,211}

Coupled with these experimental techniques, computational methods can be employed to study the atomic-level details in the GIVA PLA₂-Inhibitor complex. Extensive simulations of the phospholipase A₂ system have been carried out. Most notably, Wee *et al.* recently conducted a coarse-grained simulation of the pancreatic phospholipase A₂, in which they demonstrate how the enzyme adheres to the lipid bilayer.²¹² Quantum mechanical methodologies have also been applied to the phospholipase system.²¹³ This work has proven vital to the understanding of phospholipase A₂ chemistry and dynamics.

In turn, by running molecular dynamics (MD) simulations of GIVA PLA₂ with inhibitor, one can observe how the latter docks into and stabilizes itself in the enzyme. Contacts between the inhibitor and specific residues of GIVA PLA₂ can also be identified. This information augments the results from the deuterium exchange technique which at this time lacks the resolution to achieve single-residue data. In lieu of known crystal structures depicting the enzyme-inhibitor complex, this computational work affords working models of the complexes and characterizes key enzyme-inhibitor interactions. The MD simulations and subsequent analysis aid in drawing comparisons between the oxoamide and pyrrophenone complexes.

The study of these two very different inhibitors provides an excellent model for generalized GIVA PLA₂ inhibition. The dual techniques of deuterium exchange mass spectrometry and MD simulation are excellent methods to probe the dynamical changes induced by binding of inhibitors to any enzyme. This study also represents a continuation of our deuterium exchange studies on the PLA₂ family of enzymes.^{209,214} We have identified specific regions of the protein that interact with the oxoamide and

pyrrophenone inhibitors, and we have carried out extensive computer simulations to create a model of inhibitor binding in the active site. We have also identified significant differences in the way pyrrophenone and oxoamide bind GIVA PLA₂. This work leads to the possibilities of enhanced rational drug design through the powerful combination of experimental and computational work.

6.2 Materials and Methods

All reagents were analytical reagent grade or better. Pyrrophenone was the generous gift from Shinogi, and the 2-oxoamide AX007 was synthesized as described.¹⁹⁹

Protein Expression and Purification: C-terminal His6-tagged GIVA PLA₂, and the C2 and catalytic domains were expressed using recombinant baculovirus in a suspension culture of Sf9 insect cells. The cell pellet was lysed in 25 mM Tris-HCl pH 8.0, 150 mM NaCl, 2 mM β-mercaptoethanol, and 2 mM EGTA and then the insoluble portion was removed by centrifugation at 12,000 x g for 30 min. The supernatant was passed through a column comprised of 6 ml nickel-nitrilotriacetic acid agarose (Qiagen, Valencia, CA). The protein in the native state was eluted in the “protein buffer” (25 mM Tris-HCl pH 8.0, 100 mM NaCl, 125 mM imidazole and 2 mM dithiothreitol). The protein concentration was measured using the Bradford assay (Bio-rad) to manufacturer’s standards, and the activity was assayed using mixed micelles in a modified Dole assay.²¹⁵ Purified GIVA PLA₂ (2 mg/ml) was stored in the protein buffer on ice for DXMS experiments. Experiments were performed immediately after elution from the nickel column.

Preparation of Deuterated samples for On-exchange Experiments: D₂O buffer contained 10 mM Tris (pD 7.5), 50 mM NaCl in 98% D₂O. Hydrogen/deuterium exchange experiments were initiated by mixing 20 µl of GIVA PLA₂ (containing 40 µg) in protein buffer with 60 µl of D₂O buffer to a final concentration of 73% D₂O at pH 7.5. In inhibitor binding experiments, the GIVA PLA₂ in protein buffer was pre-incubated in the presence of 40 µM pyrrophenone, 40 µM oxoamide AX007, or DMSO control. The inhibitors were added from 600 µM stock dissolved in DMSO. The final concentration of DMSO was 1.5% for all experiments. The inhibitors were allowed to preincubate with the enzyme for 10 minutes at 23°C before addition of D₂O buffer. The D₂O buffer was added and the samples were incubated at 23°C for an additional 10, 30, 100, 300, 1000, 3000 or 10000 seconds. The deuterium exchange was quenched by adding 120 µl of ice-cold quench solution (0.96% formic acid, 1.66 M guanidine hydrochloride (GdHCl)) that acidified the sample to a final pH = 2.5 and concentrations of formic acid of 0.58%, and 1 M GdHCl. The samples were placed on ice for 10 min to partially denature the protein and obtain optimal peptide maps. Vials with frozen samples were stored at -80 °C until analysis, usually within three days.

Proteolysis-liquid-chromatography-mass spectrometry analysis of samples: All steps were performed at 0°C as previously described.^{204,206} The samples were hand-thawed on melting ice and injected onto and passed through a protease column (66 µl bed volume) filled with porcine pepsin (Sigma); immobilized on Poros 20 AL medium (Applied Biosystems) at 30 mg/ml following the manufacturer's instructions, at a flow rate of 100 µl/min with 0.05% trifluoroacetic acid (TFA). The eluate from the pepsin column was directly loaded onto a C18 column (Vydac cat #218MS5150). The peptides

were eluted at 50 μ l/min with a linear gradient of 0.046% TFA, 6.4% (v/v) acetonitrile to 0.03% TFA, 38.4% acetonitrile for 30 min. The eluate from the C18 column was directed to a Finnigan Classic LCQ mass spectrometer via its ESI probe operated with a capillary temperature of 200 °C as previously described.^{204,206}

Data processing: SEQUEST software (Thermo Finnigan Inc.) was used to identify the sequence of the peptide ions. DXMS Explorer (Sierra Analytics Inc, Modesto CA) was used for the analysis of the mass spectra as previously described.^{204,206} All selected peptides had first passed the quality-control threshold of the software and were then manually checked to insure that the observed mass envelope agreed with the calculated mass envelope. The highest signal/noise ion was picked if multiple ionization charges (1, 2 or 3) of a peptide were detected. Incorporated deuterium number was obtained by measuring the centroid shift between the non-deuterated and the partially-deuterated mass envelope.

The deuteration level of each peptide was calculated by the ratio of the incorporated deuterium number to the maximum possible deuteration number. Peptide deuteration levels in replicate samples, measured by our DXMS methods, have been found to vary by less than 10%, and we therefore regard changes greater than 10% as significant.²⁰⁴ All experiments were performed at least twice, and representative data is shown. Trends in the data were similar from experiment to experiment, but total deuterium content varied by roughly 5-10% in similar experiments carried out weeks apart. For all peptides shown in the Figures, different peptides that cover the same region are included in Figure 36.

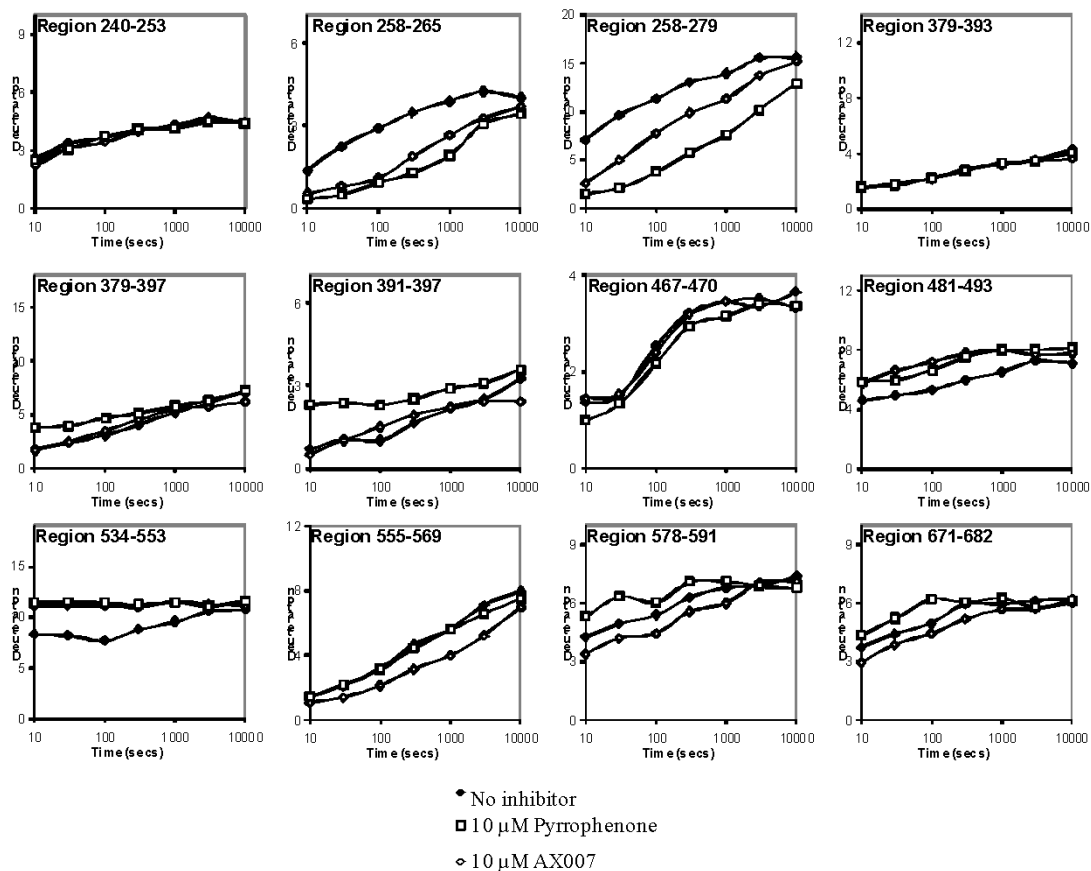


Figure 36: Deuterium exchange upon binding of 10 μ M Pyrrophenone or AX007. The number of incorporated deuterons at seven time points are displayed. Peptides 240-253, and 379-393 are given as examples of peptides with no change in exchange upon inhibitor binding.

Molecular Dynamics Simulations: In total, three systems were simulated: the apo form of GIVA PLA₂; GIVA PLA₂ with pyrrophenone bound; and GIVA PLA₂ with oxoamide bound. The structure of GIVA PLA₂ was obtained from the Protein Data Bank (code 1CJY).¹⁸³ In this reported structure, several segments were missing including residues 407-414, 431-462, 498-538, and 626-632. These apparently flexible regions were modeled into chain B of 1CJY using SWISS MODEL (Figure 37).²¹⁶ The resulting

complete structure of GIVA PLA₂ was optimized by 500 steps each of steepest decent and conjugate gradient energy minimizations and used in all three systems.

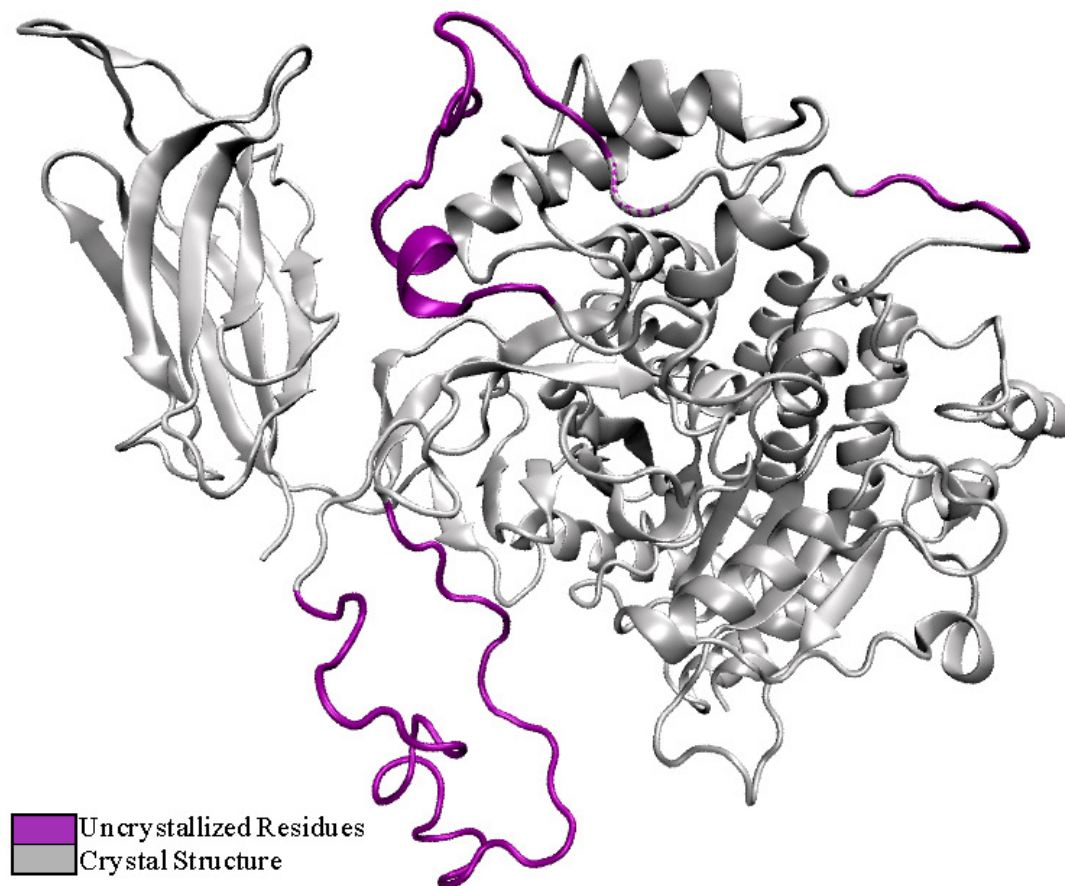


Figure 37: Modeling uncrystallized residues. The residues without defined electron density in the crystallographic structure were modeled and are shown in purple.

The inhibitors pyrrophenone and oxoamide were constructed using the Accelrys[®] Discovery Studio package, in which they were built and energy minimized to obtain their initial conformations. Each inhibitor was manually placed in the active site of GIVA PLA₂ using the aforementioned knowledge of the active site and residues implicated in binding. This was carried out using the Visual Molecular Dynamics (VMD) package,⁵¹

which was also used for further construction of all 3 systems. The protein (or the protein-inhibitor complex) was placed in a simulation box of dimensions $127 \times 73 \times 91 \text{ \AA}$, solvated with approximately 22,750 TIP3P water molecules, and neutralized with 28 sodium counterions (~80,000 atoms total for each system).

The minimization steps and all subsequent simulations were carried out using the NAMD molecular dynamics package.²¹ For the apo structure, an energy minimization was performed on the system first with the protein backbone atoms fixed—for 25,000 steps, to allow the water/ions to conform to the shape of the protein—and then with no such constraint—for another 25,000 steps, to relieve any unfavorable contacts in the entire system. For the inhibitor-bound systems, a similar energy minimization scheme was performed, with the addition of an extra minimization holding the inhibitor coordinates fixed, to relieve unfavorable contacts between the inhibitor and protein. For all three systems, a heating step was performed, in which the system was gradually heated (~50 ps) to a temperature of 300 K. During this heating and then the equilibration phase, the protein backbone and inhibitor atoms were restrained with a force constant of $5 \text{ kcal mol}^{-1} \text{ \AA}^{-2}$. In the equilibration phase, pressure coupling was added and a series of restrained MD simulations were conducted. The restraints were gradually relieved and the free, un-restrained system was equilibrated for 1 ns further. The production runs for each system commenced; each protein (or protein-inhibitor complex) was simulated for 50 ns.

For each of the production runs, the temperature was maintained at 300K using the Langevin thermostat, with a coupling constant of 2 ps^{-1} . Pressure was maintained at 1.01325 kPa using the Langevin piston method, with the ‘GroupPressure’ and

'FlexibleCell' parameters turned on. Bonds to hydrogen atoms were held fixed while using a 2 fs timestep. Non-bonded interactions and full electrostatics was calculated every 1 and 2 steps, respectively. Non-bonded interactions were smoothly switched off between 8.5 and 10 Å, while the cut-off for pairlist distance was set to 12 Å. Long-range electrostatic forces were evaluated using the particle mesh Ewald (PME) method.⁵⁶ The CHARMM22/27 all-hydrogen parameter files were used for protein and inhibitors in all three simulations.⁵⁴ The standard protein/amino acid parameters were used for GIVA PLA₂ and pyrrophenone (by analogy to various amino acid side chain structures). The oxoamide was parameterized according to the lipid parameters provided in CHARMM27.

6.3 Results and Discussion

GIVA PLA₂ Digestion Map: The protein digestion procedure was optimized to produce a peptide map that yielded the best coverage of GIVA PLA₂ as described previously.^{209,214} The optimized condition identified 185 distinct peptides that gave 94% coverage of the GIVA PLA₂ sequence (Figure 38). From this group, the 71 peptides with the best signal to noise ratio with the least amount of redundant data were used to generate the Figures in the manuscript as described previously.^{209,214} All peptides were analyzed for deuterium content as a comparison, but only the ones with non-redundant data were used in the analysis.

GIVA PLA₂ Protein Digest Map

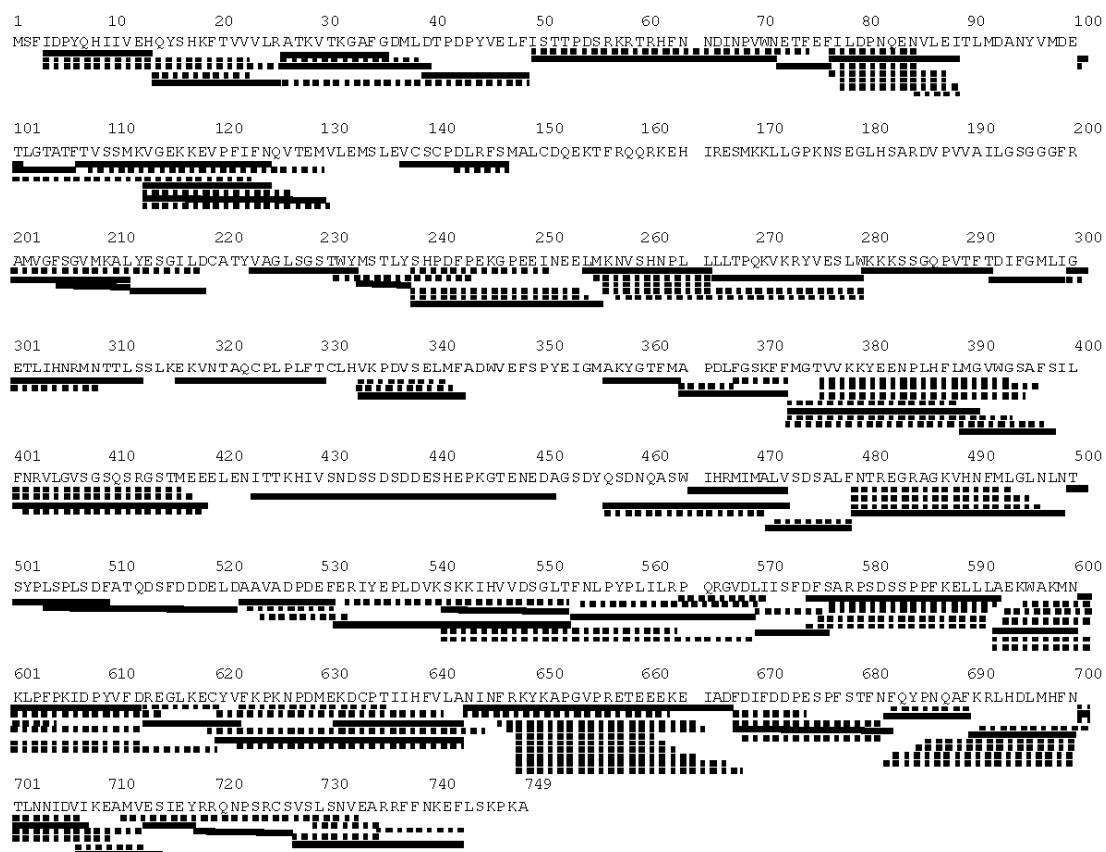


Figure 38: Peptide digest map of GIVA PLA₂. Identified and analyzed peptides resulting from pepsin-digestion are shown below the primary sequence of GIVA PLA₂. Only the peptides shown as solid lines were used in this study.

Modeling and Simulation: The overall structure of the protein remained close to the crystal structure in all three simulations (Figure 39). The regions missing in the X-ray structure, but model-built in the simulations, exhibited large fluctuations throughout the simulations, which is consistent with their being disordered in the crystals. However, the majority of the modeled regions remained solvated, without making significant contact with the rest of the protein. As a result, their motion did not affect the active site region of

the enzyme. In the apo form, GIVA PLA₂ shows no significant conformational changes, as expected. In the inhibitor-bound forms, both pyrrophenone and the oxoamide show considerable movement in the first half of simulation but settle to a converged conformation and location in the last 25 ns, as judged by the root mean square deviation (RMSD) of the inhibitors (Figure 39). Thus, the last 25 ns of each simulation were used in all subsequent simulation analysis.

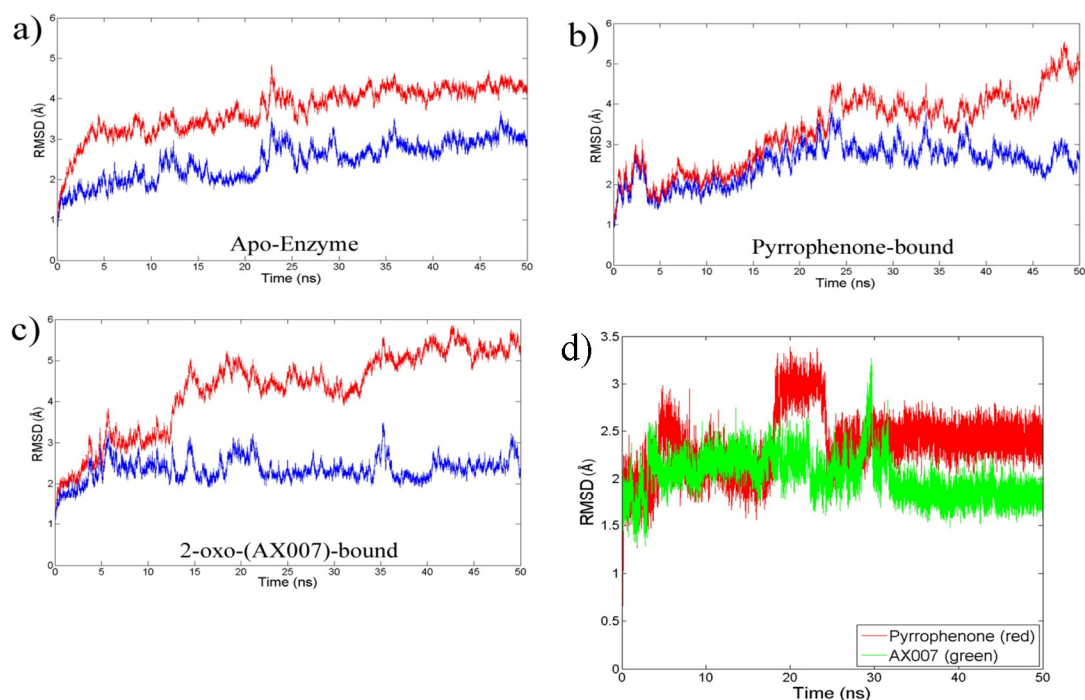


Figure 39: Root mean square deviation of protein and inhibitor. For all C_{α} RMSD measurements the red represents the RMSD of all residues, with crystallized residues RMSD shown in blue (excluding 407-414, 431-462, 498-538, and 626-632). A. The RMSD of the C_{α} in the apoenzyme over the simulation time course (50 ns). B. The RMSD of the C_{α} in the pyrrophenone bound enzyme. C. The RMSD of the C_{α} in the oxoamide bound enzyme. D. The RMSD values of both the oxoamide (green) and pyrrophenone (red) over the simulation time course is plotted.

GIVA PLA₂ Pyrrophenone Binding Experiments: We examined both the pyrrolidine derived inhibitor pyrrophenone as well as the 2-oxoamide derived inhibitor AX007. These compounds are structurally quite different and target different functionalities of the GIVA PLA₂. Therefore, determining exactly how these inhibitors bind is an important goal, because it allows the possibility of combining the best parts of each inhibitor to form new, more effective inhibitors to allow for further structure-activity studies. On-exchange experiments were performed on the intact GIVA PLA₂ enzyme in the presence of both 10 μ M pyrrophenone and 10 μ M of the 2-oxoamide inhibitor AX007 to determine if inhibitor binding caused changes in deuterium exchange rates. The experiments were carried out at relatively low ratios of protein to inhibitor (1:2) in 1.5% DMSO to prevent possible complications from inhibitor aggregation and misleading deuterium exchange results. Experiments were carried out at seven time points varying from 10 to 10,000 seconds. Both inhibitors showed multiple regions of the protein with greater than 10% change in the on-exchange rates between the inhibitor-bound and apo forms at all time points. These percent increases and decreases in on-exchange rates showed a strong correlation with computational data mapping percent chance of contact per residue number (Figure 40). The residues from 292-298 and 401-417 predicted to be in contact with the inhibitor (within 5 Å) from modeling and that show no changes in deuterium exchange are all located in regions with either extremely slow or rapid exchange, and hence there is no significant difference in exchange between apo- and halo- forms (Figure 41). The difference in on-exchange at the 100 second time point captured all of the major changes, and was used to generate the data shown in Figure 40.

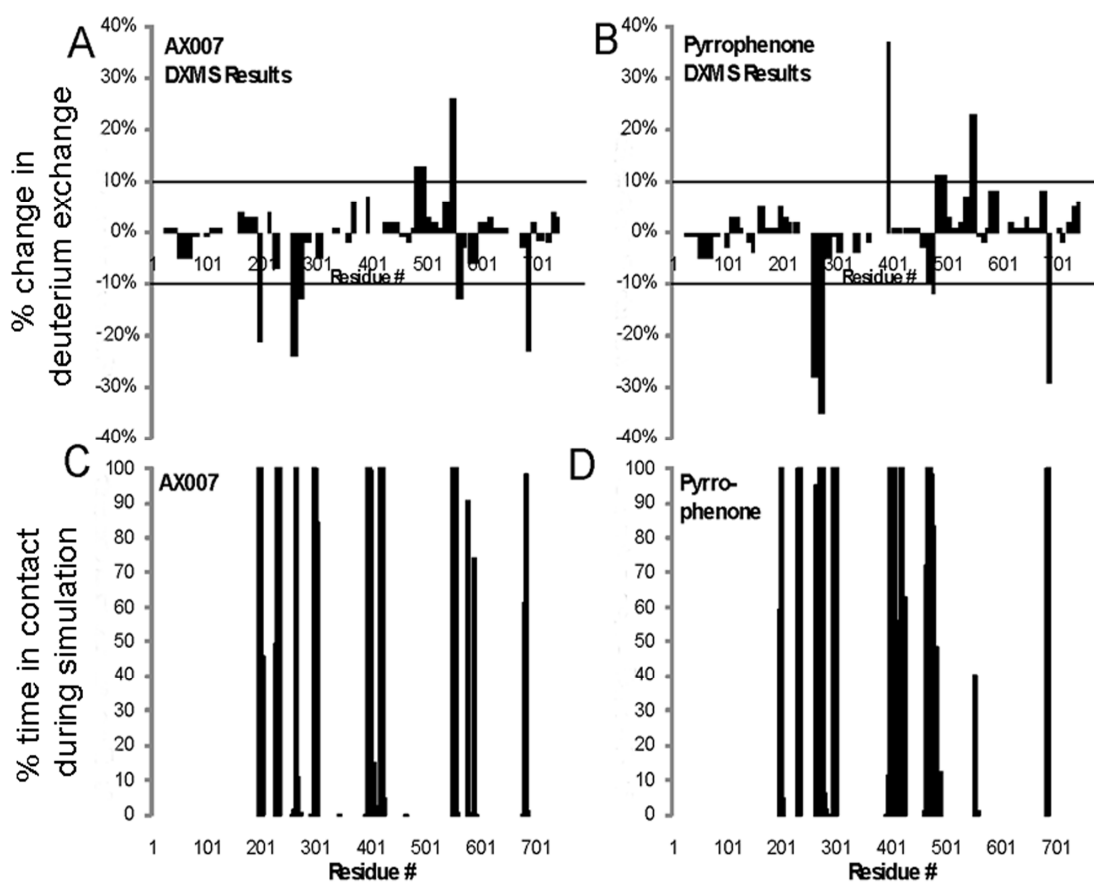


Figure 40: Deuterium exchange information compared to computer simulation results. Panels A and B: The percent change in deuterium exchange between inhibitor free GIVA PLA₂ and oxoamide-bound (panel A) or pyrrophenone-bound (panel B) GIVA PLA₂ at 100 seconds of on-exchange is shown. Each bar represents a region that deuterium exchange was quantified. All changes greater than 10% are considered significant. Panels C and D: The percent chance of specific residues being within 5 Å of the docked inhibitor in the molecular dynamics simulation are plotted for oxoamide-bound (panel C) and pyrrophenone-bound (panel D).

The inhibitor pyrrophenone was synthesized in 2001;¹⁹² and contains a thiazolidinedione ring postulated to target Arg-200 and a carbonyl group bridging the two benzoyl groups that is expected to target the active site Ser-228. This class of inhibitors was also shown, through structure-activity work, to have large increases in

inhibitory potency with the addition of large bulky lipophilic substituents, suggesting the presence of a hydrophobic binding pocket in the enzyme.¹⁹¹ Using deuterium exchange and modeling we planned to test this hypothesis based on structure-activity work.

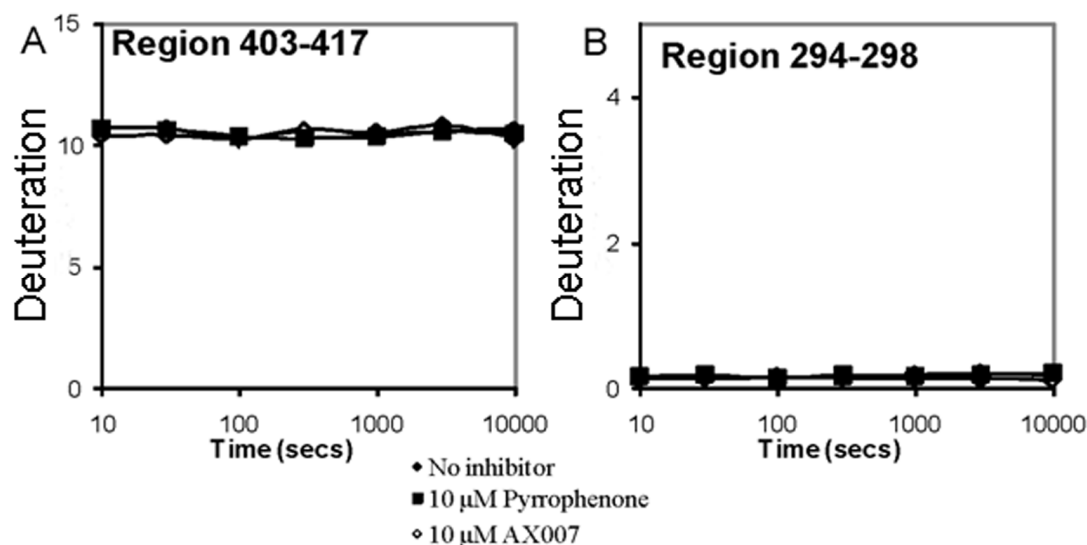


Figure 41: Regions in contact with inhibitors with extremely fast or slow rates of exchange. Region 403-417 (A) and 294-298 (B) are plotted showing extremely fast rates of exchange (region 403-417), or extremely slow rates (region 294-298), with or without pyrrophenone or oxoamide present.

Eight regions of the GIVA PLA₂ exhibited significant changes in deuterium exchange in the presence of pyrrophenone. Figure 42 shows these results both quantitatively and visually imposed on snapshots from the MD simulations. Three regions of the protein, residues 393-397, 481-495, and 543-553 exhibited increased rates of exchange in the presence of pyrrophenone. Regions 393-397 and 543-553 had greater differences in on-exchange rates (between apo- and pyrrophenone-bound enzymes) at early time points of roughly 20-30%, with the difference going to zero at later time

points. Region 393-397 contains Ala-396 and Phe-397 in contact with pyrrophenone. Region 481-495 had a constant 10-15% increase in exchange at all time points. These are the exact regions that we have previously shown had increases in on-exchange rates in the presence of the potent irreversible GIVA PLA₂ inhibitor MAFP, as well as natural phospholipid substrate vesicles.²⁰⁹ We have hypothesized that these regions show an increase in exchange due to the opening of the lid region from 415-432, and that pyrrophenone also causes an opening of the lid region upon binding in the active site. In turn, this opening event induces an increase in the solvent accessibility and results in higher on-exchange rates. This lid opening was not seen in our simulations, and this is most likely a time dependent process that is too slow to view with molecular dynamics.

Five regions of the protein, residues 256-265, 268-279, 466-470, 473-478, and 684-689 demonstrated decreases in exchange between apo- and pyrrophenone-bound enzymes (Figure 42). Region 268-279 exhibits greater than 30% decreases in exchange at all time points. Correlating with the MD simulation, this region harbors multiple residues that are in constant contact with the pyrrophenone. Regions 256-265 and 684-689 exhibit 20-30% decreases at early time points and drop to less than 10% at later time points. These regions also contain multiple hydrophobic residues demonstrated by simulation to be in contact with pyrrophenone; yet, this is to a lesser extent (and thus less of a decrease in exchange) as compared to region 268-279. Regions 466-470 and 473-478 showed 10-15% decreases in on-exchange rates from 30 to 300 seconds but no differences in exchange at earlier or later time points.

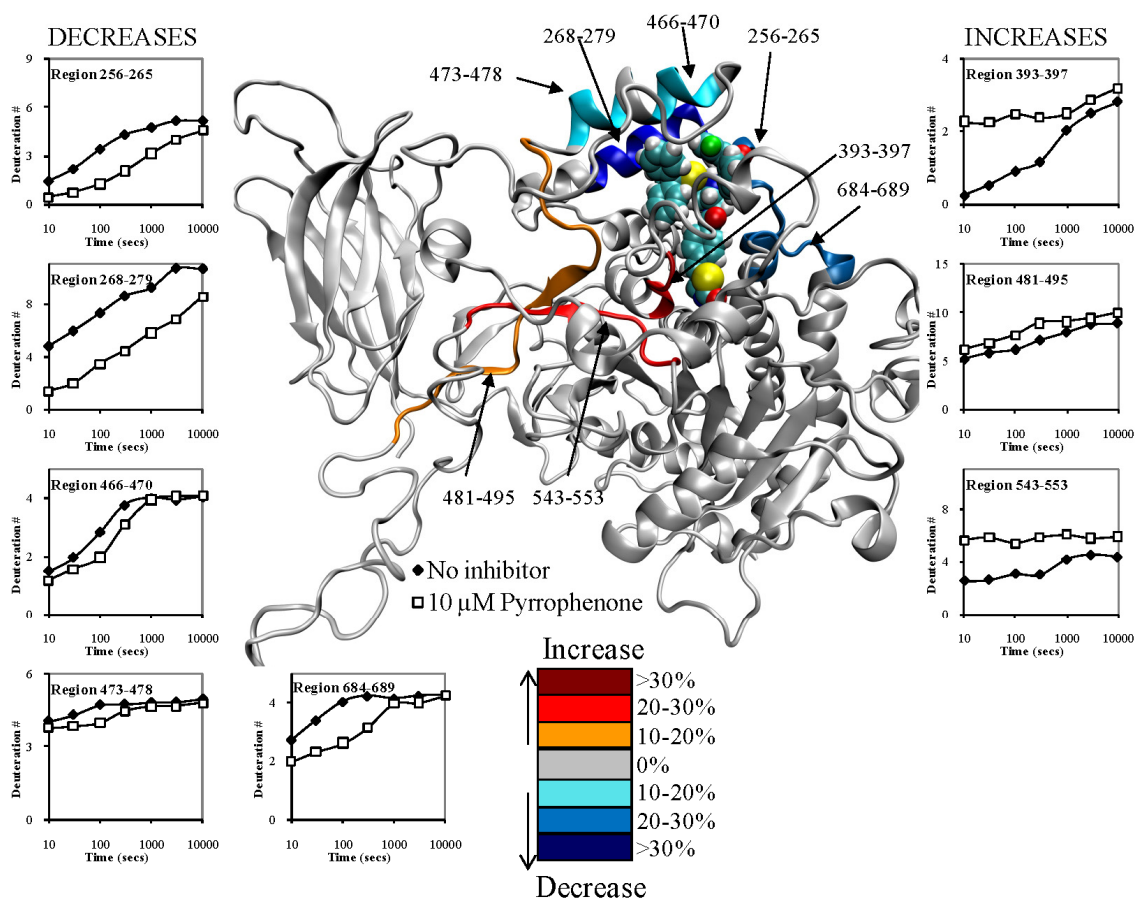


Figure 42: Deuterium exchange upon binding of 10 μM Pyrrophenone. A. The number of incorporated deuterons at seven time points in eight different regions, 256-265, 268-279, 393-397, 466-470, 473-478, 481-495, 543-553, and 684-689 in GIVA PLA2 are plotted onto the docked model of pyrrophenone binding at 50 ns of simulation time (the inhibitor is shown in space filled form). Decreases or increases in deuteriation greater than 10% are represented by the color scheme in the legend.

Our deuterium exchange results show decreases in exchange in numerous regions containing hydrophobic regions and this matches our modeling work as shown in Figure 43, where Pro-263, Leu-264, Leu -267, Val-272, Tyr-275, Trp-464, Ile-465, Ile-469, Met-470, and Phe-683 all make contact with the numerous phenyl groups in pyrrophenone. These residues most likely are acting as the hydrophobic pocket postulated through

structure activity work with pyrrophenone, and our results correlate with recent data from Wyeth showing that GIVA PLA₂ inhibitors become more potent when the steric bulk of the inhibitor is increased in functionally allowed regions.¹⁹⁰ However we find that the thiazoloidinedione functionality targets Ser-228, rather than targeting Arg-200, as originally suggested by Shinogi,^{191,192} with the carbonyl bridging the two phenyl groups in pyrrophenone being located at a large distance from the active site serine.

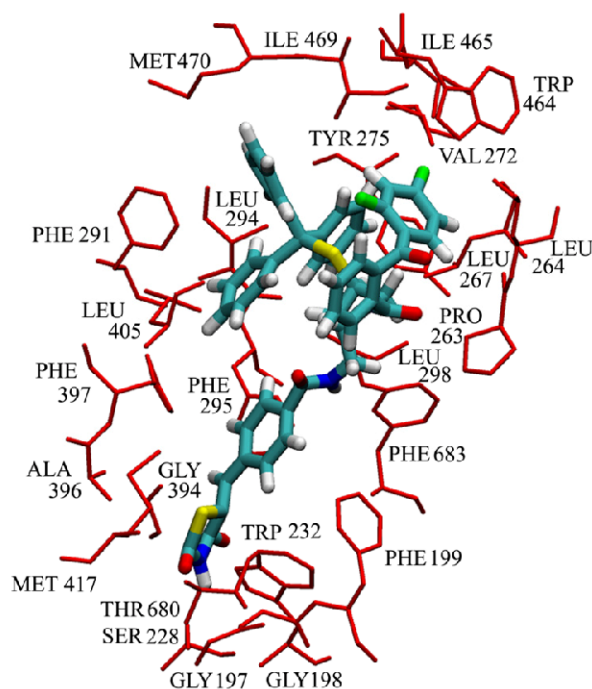


Figure 43: Residues involved in the binding of pyrrophenone. The residues that have contact with pyrrophenone greater than 90% of the time in the molecular dynamics simulation are represented as red sticks and labeled on the figure. The inhibitor is shown in the licorice representation, with carbon, hydrogen, oxygen, nitrogen and phosphorus atoms colored cyan, white, red, blue and yellow, respectively.

GIVA PLA₂ Oxoamide Binding Experiments: The 2-oxoamide inhibitor AX007 was originally synthesized and shown to be an effective GIVA PLA₂ inhibitor in 2002.¹⁹⁸

It was postulated to target GIVA PLA₂ via an interaction between its 2-oxo amide functionality and the active site Ser-228. Also, the carboxylic acid moiety of the oxoamide was designed to target Arg-200, while the inhibitor's long fatty acyl tail positions itself in the hydrophobic binding pocket.¹⁹⁹ Using deuterium exchange and modeling we planned to test these hypothesis based on structure-activity work.

Seven regions of the GIVA PLA₂ exhibited significant changes in deuterium exchange in the presence of the oxoamide (Figure 44). Two regions of the protein, residues 481-495, and 543-553 exhibit an increase in exchange in the presence of the oxoamide. These regions show the exact same deuterium on-exchange profile as the pyrrophenone-bound enzyme. However, the region 393-397 does not show any difference in exchange in the presence of the oxoamide. This result allows for multiple interpretations; perhaps the lid region is opened in a different way (as compared to the enzyme-pyrrophenone complex), thus only increasing solvent accessibility for regions 481-495 and 543-553, but not for region 393-397. Or, the lid region may be opened in the same way, but increased contacts between region 393-397 and the oxoamide cause a comparative decrease in exchange rates between the two inhibitor-bound structures.

Five regions of the protein, residues 196-201, 256-265, 268-279, 555-564, and 684-689 exhibit decreases in exchange in the presence of the oxoamide. Regions 256-265 and 684-689 reveal the same on-exchange pattern in the presence of both the oxoamide and pyrrophenone. Simulation shows that along these regions, both inhibitors make similar hydrophobic contacts with Pro-263, Leu-264, and Phe-683 as shown in Figures 43 and 45. Region 268-279 has a 10-15% decrease in exchange at all time points, which is

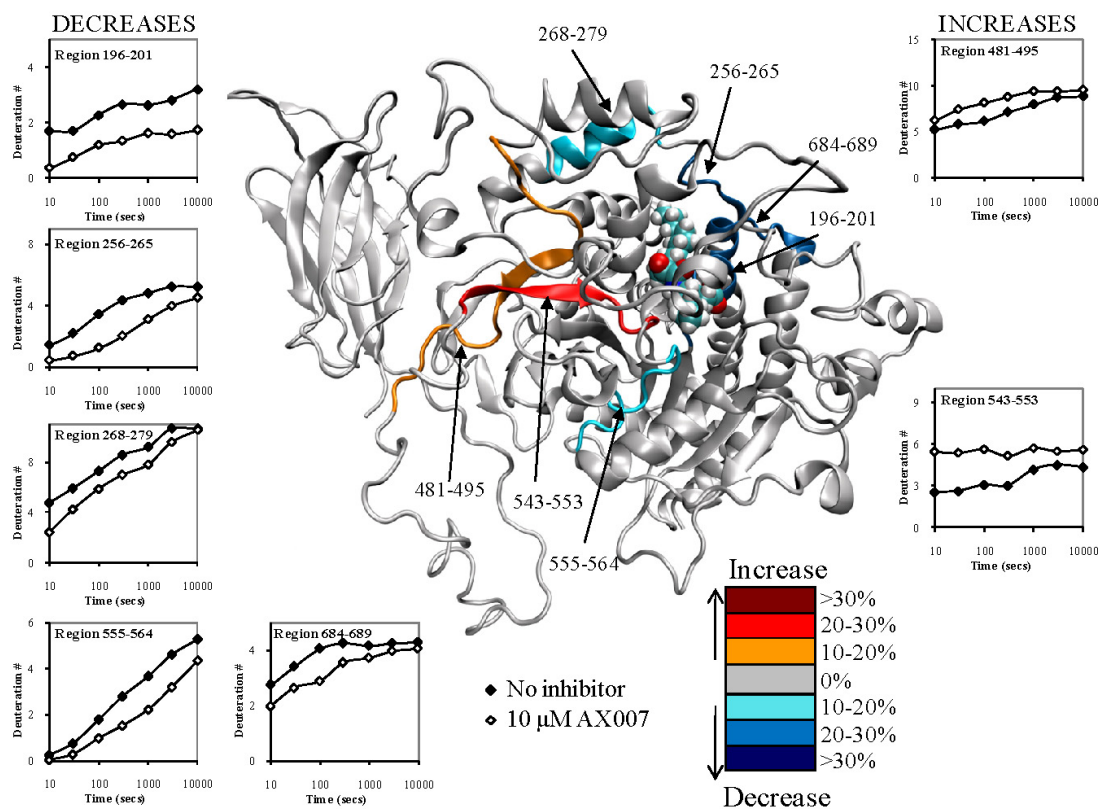


Figure 44: Deuterium exchange upon binding of 10 μ M AX007. A. The number of incorporated deuterons at seven time points in seven different regions, 196-201, 256-265, 268-279, 555-564, 481-495, 543-553, and 684-689 in GIVA PLA2 are plotted onto the docked model of the oxoamide AX007 binding at 50 ns of simulation time (the inhibitor is shown in space filled form) Decreases or increases in deuteriation greater than 10% are represented by the color scheme in the legend.

much lower than the corresponding differences in this region in the pyrrophenone-enzyme complex. This much smaller decrease in exchange in the oxoamide-enzyme complex correlates well with the simulation, which shows no residues in 268-279 making contacts with the inhibitor. Region 555-564 displays a 10-20% decrease in exchange at all time points in the presence of the oxoamide. This region contains Asp-555 and neighbors Gly-551/Leu-552, all of which are in constant contact with the oxoamide during the simulation. Recent work by us has shown that the short, nonpolar, aliphatic R-

group substituent on the oxoamide AX007 (residing on the linker between the 2-oxo and carboxylic acid) increased potency. We postulated that this is facilitated by a hydrophobic pocket in the enzyme that can accommodate this particular group.²⁰¹ The residues in and around 555-564 appear to constitute this pocket, as shown here by both on-exchange results and simulation. Region 196-201 exhibits a 20-30% decrease in exchange at all time points in the presence of the oxoamide. This region contains the proposed oxy-anion hole—residues Gly-196, Gly-197, Gly-198, Gly-229, and Arg-200—required for catalytic activity, as well as Phe-199, which is part of the hydrophobic pocket for the substrate. The modeling data shows an interaction between the carboxylic acid of the oxoamide and Arg-200, as well as the carbonyl of the 2-oxoamide in contact with the oxyanion hole composed of the numerous glycine residues.

Differences in Oxoamide and Pyrrophenone Binding: Numerous regions of the protein show the same decreases or increases in exchange with both pyrrophenone and the oxoamide AX007. These regions include 256-265, 481-495, 543-553, and 684-689, and they all show similar contacts in these regions between both AX007 and pyrrophenone as shown in Figures 43 and 45. There are also regions such as 466-470, 473-478, and 555-564 which show changes only in the presence of one or the other inhibitor, and this is explained by specific contacts only seen between pyrrophenone or the oxoamide and the protein.

However region 196-201 acts as an interesting example of the differences between pyrrophenone and oxoamide inhibitor binding. There are four different regions in the enzyme 196-201, 225-232, 577-591, and 670-682 that show an increase in exchange with pyrrophenone and a decrease in exchange with the oxoamide (Figure 46).

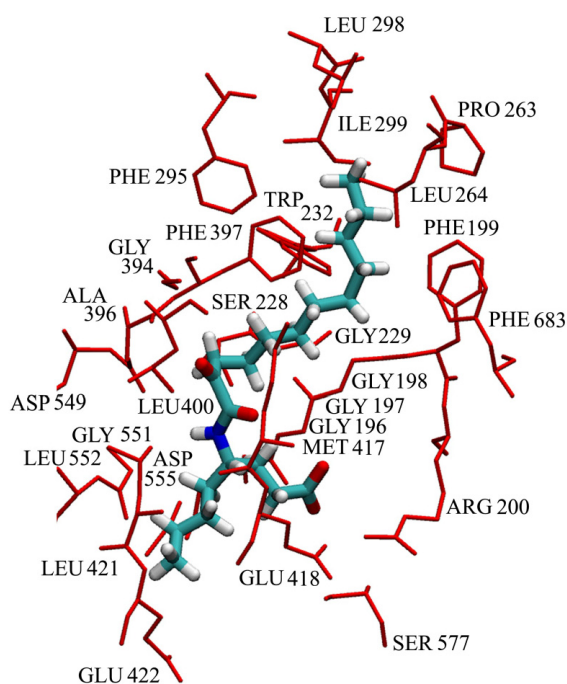


Figure 45: Residues involved in the binding of the Oxoamide AX007. The residues that have contact with the oxoamide greater than 90% of the time in the molecular dynamics simulation are represented as red sticks and labeled on the figure. The inhibitor is shown in the licorice representation, with carbon, hydrogen, oxygen, nitrogen and phosphorus atoms colored cyan, white, red, blue and yellow, respectively.

Many of these peptides do not show a change in deuterium exchange greater than 10% as compared to the apo structure. However, the comparison between pyrrophenone and the oxoamide does show a greater than 10% change in exchange. These peptide regions are all in or near the active site of the enzyme. Region 225-232, which contains the active site residue Ser-228, never exchanges greater than 25% at any time point. Yet, there is a greater than 10% change in exchange between the oxoamide and pyrrophenone-bound studies, with the oxoamide-enzyme complex showing less exchange than the pyrrophenone-bound sample. For regions 577-591 and 670-682, the main effects are most

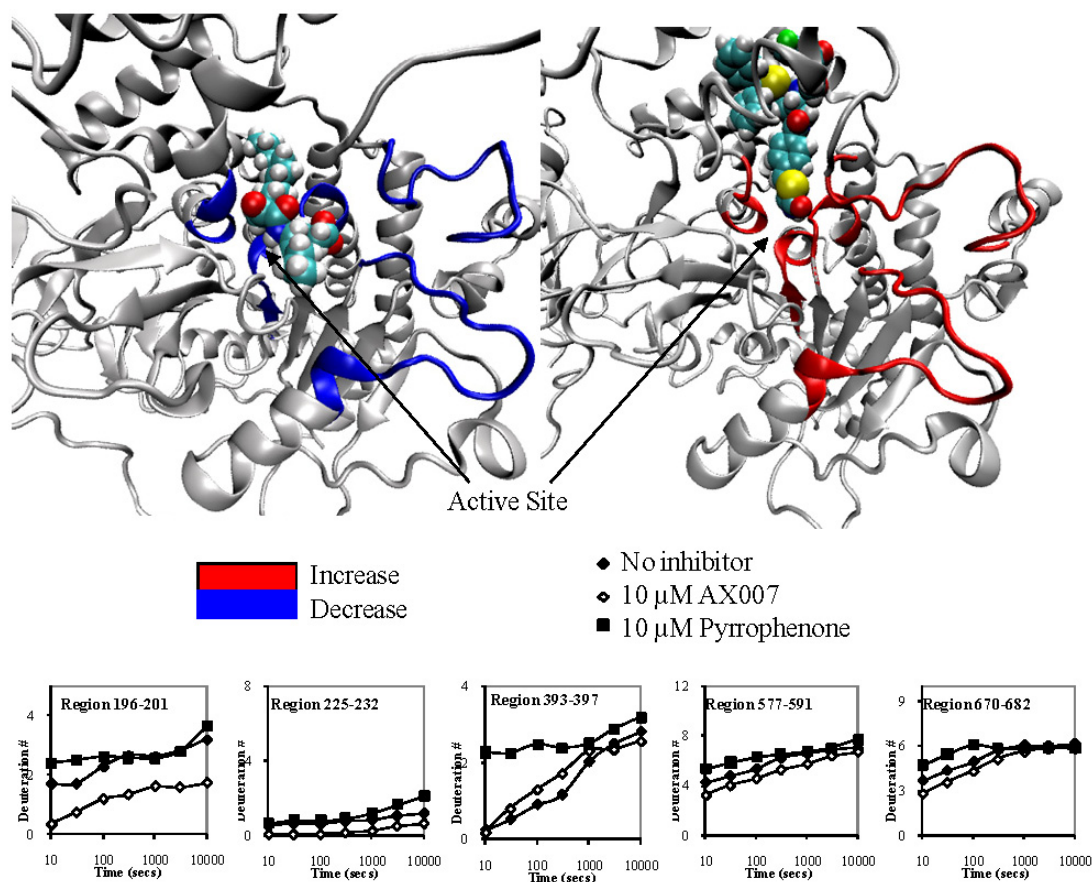


Figure 46: Different inhibitors cause different rates of exchange of the active site residues of GIVA PLA₂. The number of incorporated deuterons at seven time points in five different regions, 196-201, 225-232, 393-397, 577-591, and 670-682 in GIVA PLA₂ are plotted onto the docked models. Areas that show less exchange with the oxoamide AX007 and more exchange with pyrrophenone are colored onto the respective structures.

likely localized to 577-580 and 680-682, respectively, which are located within 5 Å of the active site. These results show that the 2-oxoamide inhibitor AX007 decreases the solvent accessibility of the active site while pyrrophenone has the opposite effect (an increase). These results help to explain why region 393-397 has an increase in exchange with pyrrophenone and not with the oxoamide. This region is located near the active site, and

increases in exchange are seen with the presence of pyrrophenone, MAFP, and natural phospholipid substrate,²⁰⁹ but not the oxoamide. The decreased solvent accessibility of the active site in the presence of the oxoamide would explain the lack of exchange increases in region 393-397. From viewing Figure 46, it is also apparent that the oxoamide mainly occupies the active site area, while pyrrophenone is mainly bound in the cap region near the interfacial binding surface of the enzyme.

6.4 Conclusion

These results have greatly enhanced our knowledge of how these two different inhibitors bind GIVA PLA₂ and have allowed us to model all the residues contacting both inhibitors. This will allow us to create new inhibitors combining the 2-oxoamide functionality with a bulky lipophilic substituent in place of the acyl fatty acid tail to mimic how pyrrophenone binds GIVA PLA₂ through multiple hydrophobic contacts located on or near the cap region. This study is the first to combine deuterium exchange mass spectrometry with molecular dynamics simulations for the determination of inhibitor binding. This methodology is an exciting new tool in developing better inhibitors, and we plan to continue this work through the synthesis and testing of new GIVA PLA₂ inhibitors based on our results.

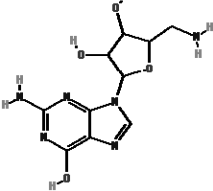
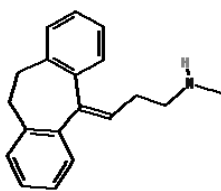
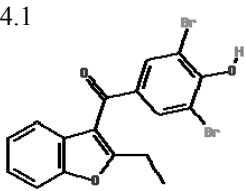
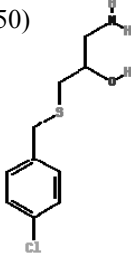
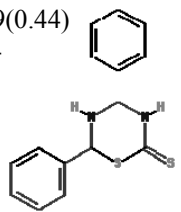
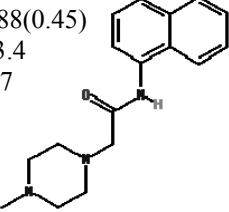
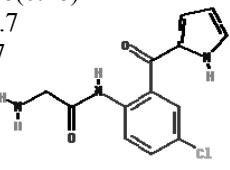
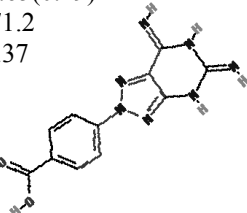
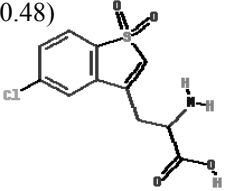
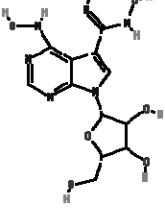
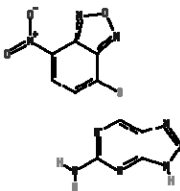
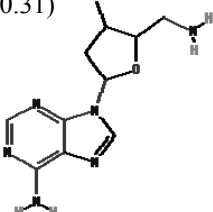
6.5 Acknowledgements

The authors thank Dr Howard Hsu for constructive reviews of this manuscript. We also thank the following agencies for funding: NIH GM20501 (E.A.D.), and

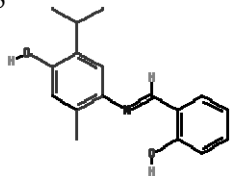
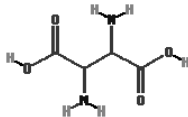
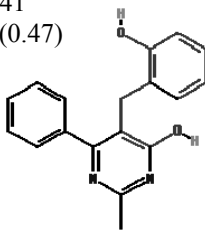
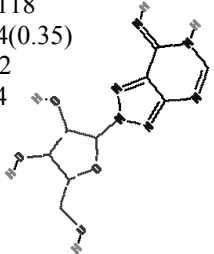
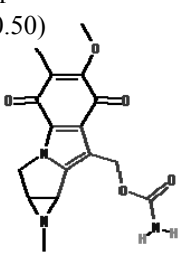
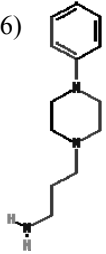
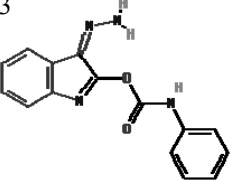
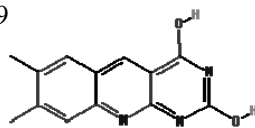
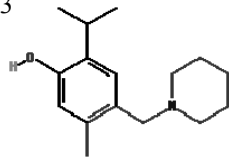
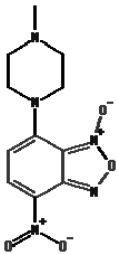
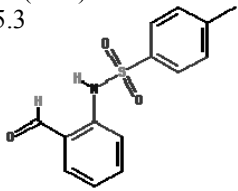
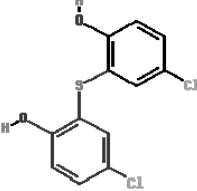
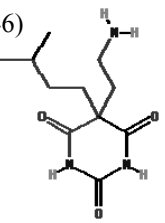
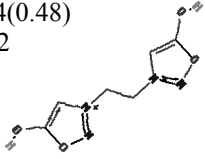
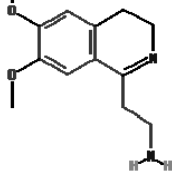
CA099835, CA118595, GM037684, AI0220221, AI022160 (V.L.W); a Discovery Grant (UC10591) from the University of California Industry-University Cooperative Research Program (V.L.W); NIH GM31749 and NSF Grants MCB-0506593 and MCA93S013 (J.A.M.). This work was also supported by the Howard Hughes Medical Institute, San Diego Supercomputing Center, the W.M. Keck Foundation, Accelrys, Inc., the National Biomedical Computational Resource, and the Center for Theoretical Biological Physics.

Chapter 6, in full, is a near reprint of the material as it appears in a submission to the Journal of the American Chemical Society 2009. This is a co-authored article. The dissertation author and J. Burke were the primary co-contributors to this work. A. A. Gorfe, G. Kokotos, S. Li, and V. Woods contributed in an advisory capacity. J. A. McCammon and E. Dennis served as the head advisers/principal investigators of the computational and experimental components (respectively) of the work.

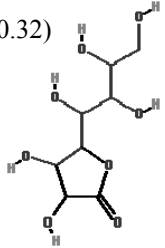
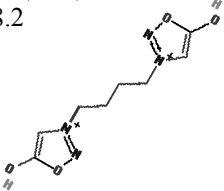
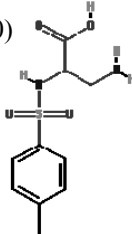
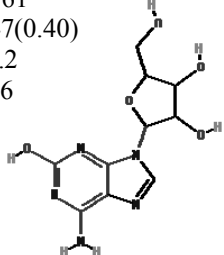
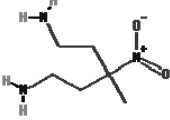
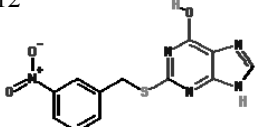
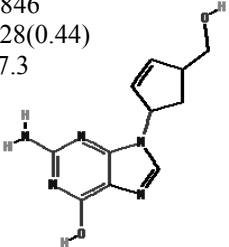
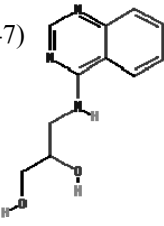
Appendix A-1: Ligands from the NCIDS that bind well across all three species and snapshots of AChBP, as judged by a standard deviation ≤ 0.50 kcal mol⁻¹. ‘NCI’ is the National Cancer Institute’s identifying number, also known as the NSC number. ‘ ΔG ’ is the calculated free energy of binding, in kcal mol⁻¹ along with the standard deviation (in parentheses) across all 15 receptor complexes. ‘MW’ is the molecular weight of the compound in g mol⁻¹. ‘log P’ is the solubility (octanol/water partitioning), ‘HA’ and ‘HD’ are the numbers of hydrogen bond acceptors and donors (respectively) on the ligand. See reference 160 for further pharmacological data.

NCI: 108608 ΔG : -8.89(0.50) MW: 282.3 logP: -2.68 HA: 10 HD: 5 	NCI: 169453 ΔG : -8.23(0.44) MW: 263.4 logP: 4.74 HA: 1 HD: 1 	NCI: 85433 ΔG : -8.15(0.45) MW: 424.1 logP: --- HA: 3 HD: 1 
NCI: 24915 ΔG : -7.90(0.50) MW: 231.7 logP: 1.24 HA: 2 HD: 2 	NCI: 150554 ΔG : -7.89(0.44) MW: 286.4 logP: 3.78 HA: 1 HD: 2 	NCI: 674348 ΔG : -7.88(0.45) MW: 283.4 logP: 1.47 HA: 3 HD: 1 
NCI: 140873 ΔG : -7.66(0.46) MW: 277.7 logP: 1.47 HA: 4 HD: 3 	NCI: 115883 ΔG : -7.65(0.49) MW: 271.2 logP: 0.37 HA: 9 HD: 5 	NCI: 206601 ΔG : -7.61(0.48) MW: 287.7 logP: -1.85 HA: 5 HD: 2 
NCI: 154829 ΔG : -8.15(0.47) MW: 340.3 logP: -1.97 HA: 12 HD: 8 	NCI: 348401 ΔG : -8.01(0.49) MW: 330.3 logP: --- HA: 10 HD: 2 	NCI: 105017 ΔG : -7.76(0.31) MW: 250.3 logP: -2.19 HA: 8 HD: 3 

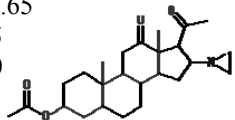
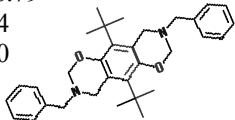
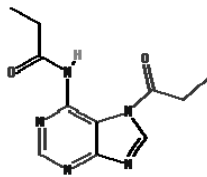
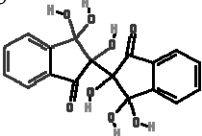
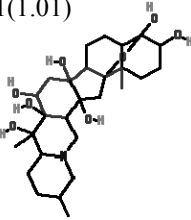
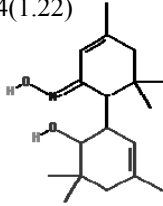
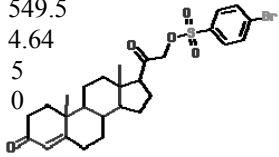
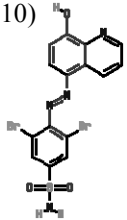
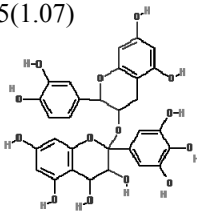
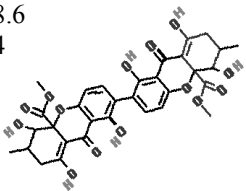

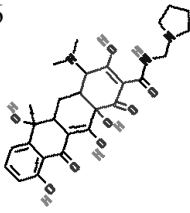
Appendix A-1 (continued):

<p>NCI: 30712 ΔG: -7.70(0.47) MW: 269.3 logP: 4.24 HA: 3 HD: 2</p> 	<p>NCI: 146876 ΔG: -7.59(0.44) MW: 148.1 logP: -5.87 HA: 6 HD: 4</p> 	<p>NCI: 112541 ΔG: -7.57(0.47) MW: 292.3 logP: 4.3 HA: 4 HD: 2</p> 
<p>NCI: 133118 ΔG: -7.54(0.35) MW: 268.2 logP: -2.54 HA: 10 HD: 5</p> 	<p>NCI: 123111 ΔG: -7.49(0.50) MW: 331.3 logP: -0.84 HA: 7 HD: 1</p> 	<p>NCI: 93277 ΔG: -7.54(0.46) MW: 219.3 logP: 1.27 HA: 3 HD: 1</p> 
<p>NCI: 329070 ΔG: -7.36(0.47) MW: 280.3 logP: 2.58 HA: 5 HD: 2</p> 	<p>NCI: 109174 ΔG: -7.36(0.48) MW: 241.3 logP: 2.9 HA: 5 HD: 2</p> 	<p>NCI: 10776 ΔG: -7.37(0.38) MW: 247.4 logP: 4.63 HA: 2 HD: 1</p> 
<p>NCI: 207895 ΔG: -7.29(0.36) MW: 279.3 logP: --- HA: 7 HD: 0</p> 	<p>NCI: 120186 ΔG: -7.28(0.42) MW: 275.3 logP: 2.9 HA: 4 HD: 1</p> 	<p>NCI: 55636 ΔG: -7.32(0.46) MW: 287.2 logP: 4.62 HA: 2 HD: 2</p> 
<p>NCI: 85260 ΔG: -7.20(0.46) MW: 241.3 logP: 0.53 HA: 4 HD: 3</p> 	<p>NCI: 54671 ΔG: -7.14(0.48) MW: 200.2 logP: --- HA: 6 HD: 2</p> 	<p>NCI: 153533 ΔG: -7.26(0.41) MW: 234.3 logP: 3.16 HA: 4 HD: 1</p> 

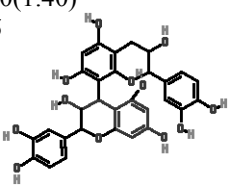
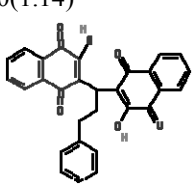
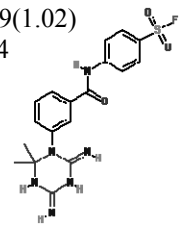
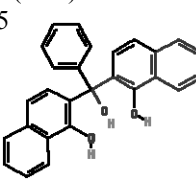
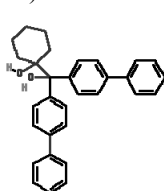
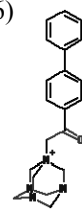
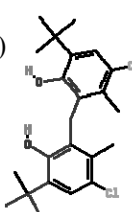
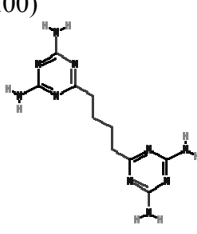
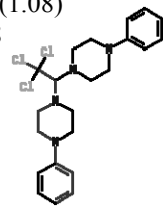
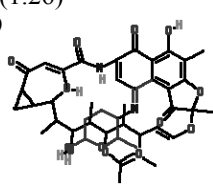
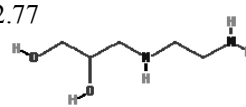
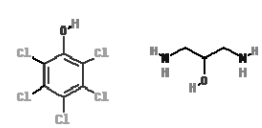
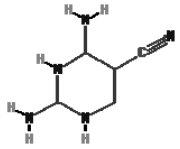
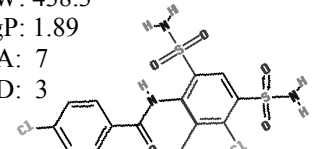
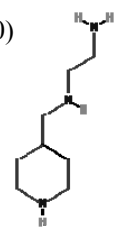
Appendix A-1 (continued):

<p>NCI: 1684 ΔG: -7.56(0.32) MW: 238.2 logP: -3.48 HA: 8 HD: 6</p> 	<p>NCI: 54672 ΔG: -7.54(0.46) MW: 228.2 logP: --- HA: 6 HD: 2</p> 	<p>NCI: 85420 ΔG: -7.48(0.40) MW: 258.3 logP: -3.62 HA: 6 HD: 3</p> 
<p>NCI: 12161 ΔG: -7.47(0.40) MW: 283.2 logP: -1.46 HA: 10 HD: 5</p> 	<p>NCI: 116805 ΔG: -7.34(0.44) MW: 161.2 logP: -0.63 HA: 4 HD: 2</p> 	<p>NCI: 118208 ΔG: -7.34(0.49) MW: 303.3 logP: 2.12 HA: 7 HD: 2</p> 
<p>NCI: 614846 ΔG: -7.28(0.44) MW: 247.3 logP: 0.1 HA: 7 HD: 3</p> 	<p>NCI: 13220 ΔG: -7.26(0.47) MW: 219.2 logP: 0.14 HA: 5 HD: 3</p> 	<p>This cell is intentionally left blank.</p>

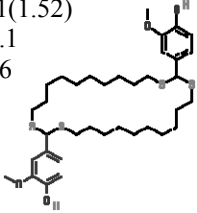
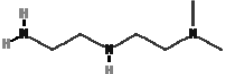
Appendix A-2: Ligands from the NCIDS that seem to differentiate between the three species of AChBP, as judged by the standard deviation in the binding energy (> 1.00 kcal mol⁻¹). 'NCI' is the National Cancer Institute's identifying number, also known as the NSC number. ' ΔG ' is the calculated free energy of binding, in kcal mol⁻¹ along with the standard deviation (in parentheses) across all 15 receptor complexes. 'MW' is the molecular weight of the compound in g mol⁻¹. 'log P' is the solubility (octanol/water partitioning), 'HA' and 'HD' are the numbers of hydrogen bond acceptors and donors (respectively) on the ligand. See reference 160 for further pharmacological data.

NCI: 109128 ΔG : -12.49(1.72) MW: 415.6 logP: 2.65 HA: 5 HD: 0 	NCI: 48458 ΔG : -12.16(1.78) MW: 484.7 logP: 8.79 HA: 4 HD: 0 	NCI: 47455 ΔG : -12.03(2.57) MW: 247.3 logP: -0.26 HA: 5 HD: 1 
NCI: 108697 ΔG : -11.45(1.80) MW: 358.3 logP: 2.65 HA: 8 HD: 6 	NCI: 99804 ΔG : -11.21(1.01) MW: 509.6 logP: -1.2 HA: 9 HD: 7 	NCI: 40781 ΔG : -10.94(1.22) MW: 291.4 logP: 5.47 HA: 3 HD: 2 
NCI: 88915 ΔG : -10.63(1.00) MW: 549.5 logP: 4.64 HA: 5 HD: 0 	NCI: 114381 ΔG : -10.29(1.10) MW: 486.1 logP: 3.94 HA: 7 HD: 2 	NCI: 143101 ΔG : -10.25(1.07) MW: 610.5 logP: 2.2 HA: 14 HD: 11 
NCI: 159631 ΔG : -11.78(1.29) MW: 638.6 logP: 2.24 HA: 14 HD: 6 	NCI: 44102 ΔG : -11.70(2.20) MW: 276.3 logP: 2.03 HA: 4 HD: 2 	NCI: 50352 ΔG : -10.73(1.22) MW: 527.6 logP: -0.79 HA: 10 HD: 6 

Appendix A-2 (continued):

<p>NCI: 143099 ΔG: -10.70(1.40) MW: 578.5 logP: 1.88 HA: 12 HD: 10</p> 	<p>NCI: 117274 ΔG: -10.20(1.14) MW: 464.4 logP: 4.84 HA: 6 HD: 2</p> 	<p>NCI: 113909 ΔG: -10.09(1.02) MW: 418.4 logP: 3.83 HA: 9 HD: 5</p> 
<p>NCI: 13984 ΔG: -10.03(1.33) MW: 392.5 logP: 5.77 HA: 3 HD: 3</p> 	<p>NCI: 351123 ΔG: -9.77(1.32) MW: 434.6 logP: 7.86 HA: 2 HD: 2</p> 	<p>NCI: 35450 ΔG: -9.37(1.06) MW: 335.4 logP: -1.76 HA: 4 HD: 0</p> 
<p>NCI: 5857 ΔG: -8.60(1.01) MW: 409.4 logP: 9.26 HA: 2 HD: 2</p> 	<p>NCI: 101825 ΔG: -8.39(1.00) MW: 276.3 logP: 1.09 HA: 10 HD: 4</p> 	<p>NCI: 93317 ΔG: -8.10(1.08) MW: 453.8 logP: 4.45 HA: 4 HD: 0</p> 
<p>NCI: 177383 ΔG: -7.64(1.26) MW: 822.9 logP: 6.55 HA: 15 HD: 5</p> 	<p>NCI: 339497 ΔG: -7.55(1.13) MW: 134.2 logP: -2.77 HA: 4 HD: 4</p> 	<p>NCI: 77554 ΔG: -7.33(1.27) MW: 356.5 logP: --- HA: 4 HD: 4</p> 
<p>NCI: 211332 ΔG: -9.36(1.46) MW: 141.2 logP: -4.94 HA: 5 HD: 4</p> 	<p>NCI: 25869 ΔG: -9.34(1.05) MW: 438.3 logP: 1.89 HA: 7 HD: 3</p> 	<p>NCI: 74472 ΔG: -7.74(1.00) MW: 157.3 logP: -0.38 HA: 3 HD: 3</p> 

Appendix A-2 (continued):

<p>NCI: 94783 ΔG: -7.71(1.52) MW: 681.1 logP: 12.96 HA: 4 HD: 2</p> 	<p>NCI: 345672 ΔG: -6.67(1.08) MW: 131.2 logP: -1.46 HA: 3 HD: 2</p> 	<p>This cell is intentionally left blank.</p>
--	--	---

References

1. Heath, M. T. *Scientific Computing: An Introductory Survey* **2002**, 2nd Edition, The McGraw-Hill Companies Inc.
2. Butcher, J. C. *Numerical Methods for Ordinary Differential Equations* **2003**, 2nd Edition, Wiley.
3. Humphreys, P. *Extending Ourselves: Computational Science, Empiricism, and Scientific Method* **2007**, 1st Edition, Oxford University Press.
4. McClean, J. L.; Maltrud, Mathew E.; Bryan, F. O. *Measures of the fidelity of eddying ocean models* **2006**, *Oceanography*, 19, 104-117.
5. Chourasia, A.; Cutchin, S.; Aagaard, B. *Visualizaing the ground motions of the 1906 San Francisco earthquake* **2008**, *Computers & Geosciences*, 34, 1798-1805.
6. Haile, J. M. *Molecular Dynamics Simulation: Elementary Methods* **1997**, 1st Edition, Wiley-Interscience.
7. Croarken, M. J. L. *J. Comrie and the origins of the scientific computing service* **1999**, *IEEE Anals of the History of Computing*, 21, 70-71.
8. McCartney, S. *ENIAC: The Triumphs and Tragedies of the World's First Computer* **2001**, 1st Edition, Berkley Trade.
9. Allan, R. A. *A History of the Personal Computer: The People and the Technology* **2001**, 1st Edition, Allan Publishing.
10. Press, W. H.; Teukolsky, S. A.; Vetterling, W. T.; Flannery, B. P. *Numerical Recipes in C++: The Art of Scientific Computing* **2002**, 2nd Edition, Cambridge University Press.
11. Gropp, W.; Lusk, E.; Skjellum, A. *Using MPI: Portable Parallel Programming with the Message-Passing Interface* **1999**, 2nd Edition, MIT Press.
12. Schindler, S.; Mueller, E. *Simulations of the evolution of galaxy clusters. II. dynamics of the intra-cluster gas* **1993**, *Astronomy and Astrophysics*, 272, 137-152.
13. Oppong, J. R.; Mikler, A. R.; Moonan, P.; Weis, S. *From medical geography to computational epidemiology – dynamics of tuberculosis transmission in enclosed spaces* **2006**, *Lecture Notes in Computer Science*, 3473, 189-197.
14. Olsen, R. *Computational finance as a driver of economics: A research agenda for financial studies* **2008**, *IEEE Computational Intelligence Magazine*, 3, 35-38.

-
15. Pople, J. A. *Nobel lecture: quantum chemical models* **1999**, Reviews of Modern Physics, 71, 1267-1274.
 16. Kohn, W. *Nobel lecture: electronic structure of matter—wave functions and density functionals* **1999**, Reviews of Modern Physics, 71, 1253-1266.
 17. McCammon, J. A.; Gelin, B. R.; Karplus, M. *Dynamics of folded proteins* **1977**, Nature, 267, 585-590.
 18. Karplus, M.; McCammon, J. A. *Protein structural fluctuations during a period of 100 ps* **1979**, Nature, 277, 578.
 19. Van der Spoel, D.; Lindahl, E.; Hess, B.; Groenhof, G.; Mark, A. E.; Berendsen, H. J. *GROMACS: fast, flexible, and free* **2005**, Journal of Computational Chemistry, 26, 1701-1718.
 20. Case, D. A.; Cheatham, T. E.; Darden, T.; Gohlke, H.; Luo, R.; Merz, K. M.; Onufriev, A.; Simmerling, C.; Wang, B.; Woods, R. *The Amber biomolecular simulation programs* **2005**, Journal of Computational Chemistry, 26, 1668-1688.
 21. Phillips, J. C.; Braun, R.; Wang, W.; Gumbart, J.; Tajkhorshid, E.; Villa, E.; Chipot, C.; Skeel, R. D.; Kalé, L.; Schulten, K. *Scalable molecular dynamics with NAMD* **2005**, Journal of Computational Chemistry, 26, 1781-1802.
 22. Alvarez, J. C. *High-throughput docking as a source of novel drug leads* **2004**, Current Opinion in Chemical Biology, 8, 365-370.
 23. Schlick, T. *Molecular Modeling and Simulation: An Interdisciplinary Guide* **2002**, 1st Edition, Springer-Verlag New York Inc.
 24. Kitchen, D. B.; Decornez, H.; Furr, J. R.; Bajorath, J. *Docking and scoring in virtual screening for drug discovery: methods and applications* **2004**, Nature Reviews Drug Discovery, 3, 935-949.
 25. Arkhipov, A.; Freddolino, P. L.; Schulten, K. *Stability and dynamics of virus capsids described by coarse-grained modeling* **2006**, Structure, 14, 1767-1777.
 26. Romanowska, J.; Setny, P.; Trylska, J. *Molecular dynamics study of the ribosomal A-site* **2008**, Journal of Physical Chemistry B, 112, 15227-15243.
 27. Lauf, P. K.; Poulik, M. D. *Solubilization and structural integrity of the human red cell membrane* **2008**, British Journal of Haematology, 15, 191-202.

-
28. Simons, K. *Model systems, lipid rafts, and cell membranes* **2004**, Annual Review of Biophysics and Biomolecular Structure, 33, 269-295.
 29. Van der Ploeg, P.; Berendsen, H. J. C. *Molecular dynamics simulation of a bilayer membrane* **1982**, Journal of Chemical Physics, 76, 3271–3276.
 30. Tieleman, D. P.; Berendsen, H. J. C. *Molecular dynamics simulations of fully hydrated DPPC with different macroscopic boundary conditions and parameters* **1996**, Journal of Chemical Physics, 105, 4871-4880.
 31. Marrink, S. J.; Berger, O.; Tieleman, D. P.; Jaehnig, F. *Adhesion forces of lipids in a phospholipid membrane studied by molecular dynamics simulations* **1998**, Biophysical Journal, 74, 931-943.
 32. Gullingsrud, J.; Schulten, K. *Lipid bilayer pressure profiles and mechanosensitive channel gating* **2004**, Biophysical Journal, 86, 3496-3509.
 33. Sansom, M. S. P.; Adcock, C.; Smith, G. R. *Modeling and simulation of ion channels: applications to the nicotinic acetylcholine receptor* **1998**, Journal of Structural Biology, 121, 246-262.
 34. Rocca, P. L.; Biggin, P. C.; Tieleman, D. P.; Sansom, M. S. P. *Simulation studies of the interaction of anti-microbial peptides and lipid bilayers* **1999**, Biochimica et Biophysica Acta (BBA) – Biomembranes, 1462, 185-200.
 35. Luo, X.; Zhang, D.; Weinstein, H. *Ligand-induced domain motion in the activation mechanism of a G-protein-coupled receptor* **1994**, Protein Engineering, 7, 1441-1448.
 36. Marsh, D. *Lateral pressure in membranes* **1996**, Biochimica et Biophysica Acta, 1286, 183-223.
 37. Cantor, R. *The influence of membrane lateral pressures on simple geometric models of protein conformational equilibria* **1999**, Chemistry Physics of Lipids, 101, 45-56.
 38. Templer, R. H.; Castle, S. J.; Curran, A. R.; Rumbles, G.; Klug, D. R. *Sensing isothermal changes in the lateral pressure in model membranes using di-pyrenyl phosphatidylcholine* **1998**, Faraday Discussions, 111, 69-78.
 39. Brannigan, G.; Philips, P. F. Brown F. L. *Flexible lipid bilayers in implicit solvent* **2005**, . Physical Review E Statistical Nonlinear Soft Matter Physics, 72, 01191, 1-4.
 40. Goetz, R.; Lipowsky, R. *Computer simulations of bilayer membranes: self-assembly and interfacial tension* **1998**, Journal of Chemical Physics, 108, 7397-7409.

-
41. Lindahl, E.; Edholm, O. *Spatial and energetic-entropic decomposition of surface tension in lipid bilayers from molecular dynamics simulations* **2000**, Journal of Chemical Physics, 113, 3882-3893.
 42. de Planque, M. R. ; Rijkers, D. T. ; Liskamp, R. M. ; Separovic, F. *The alphaM1 transmembrane segment of the nicotinic acetylcholine receptor interacts strongly with model membranes* **2004**, Magnetic Resonance in Chemistry, 42, 148-154.
 43. Martinez, K. L.; Gohon, Y.; Corringer, P. J.; Tribet, C.; Merola, F.; Changeux, J. P.; Popot, J. L. *Allosteric transitions of torpedo acetylcholine receptor in lipids, detergent and amphipols: molecular interactions vs. physical constraints* **2002**, FEBS Letters, 528, 251-256.
 44. Baenziger, J. E.; Morris, M. L.; Darsaut, T. E.; Ryan, S. E. *Effect of membrane lipid composition on the conformational equilibria of the nicotinic acetylcholine receptor* **2000**, Journal of Biological Chemistry, 275, 777-784.
 45. Carrillo-Tripp, M.; Feller, S. E. *Evidence for a mechanism by which omega-3 polyunsaturated lipids may affect membrane protein function* **2005**, Biochemistry, 44, 10164-10169.
 46. Patra, M. *Lateral pressure profiles in cholesterol-DPPC bilayers* **2005**, European Biophysical Journal, 35, 79-88.
 47. Hessa, T.; Kim, H.; Bihlmaier, K.; Lundin, C.; Boekel, J.; Andersson, H.; Nilsson, I.; White, S. H.; von Heijne, G. *Recognition of transmembrane helices by the endoplasmic reticulum translocon* **2005**, Nature, 433, 377-381.
 48. Dawson, C. R.; Drake, A. F.; Helliwell, J.; Hider, R. C. *The interaction of bee melittin with lipid bilayer membranes* **1978**, Biochimica et Biophysica Acta, 510, 75-86.
 49. Berneche, S.; Nina, M.; Roux, B. *Molecular dynamics simulation of melittin in a dimyristoylphosphatidylcholine bilayer membrane* **1998**, Biophysical Journal, 75, 1603-1618.
 50. Terwilliger, T. C.; Eisenberg, D. *The structure of melittin: structure determination and partial refinement* **1982**, Journal of Biological Chemistry, 257, 6010-6015.
 51. Humphrey, W.; Dalke, A.; Schulten, K. *VMD-visual molecular dynamics* **1996**, Journal of Molecular Graphics, 14, 33-38.
 52. Bachar, M.; Becker, O. M. *Protein-induced membrane disorder: a molecular dynamics study of melittin in a dipalmitoylphosphatidylcholine bilayer* **2000**, Biophysical Journal, 78, 1359-1375.

-
53. Kal, L.; Skeel, R.; Bhandarkar, M.; Brunner, R.; Gursoy, A.; Krawetz, N.; Phillips, J.; Shinozaki, A.; Varadarajan, K.; Schulten, K. *NAMD2: greater scalability for parallel molecular dynamics* 1999, *Journal of Computational Physics*, 151, 283-312.
54. MacKerell, A. D.; Bashford, D.; Bellott, M.; Dunbrack, R. L.; Evanseck, J. D.; Field, M. J.; Fischer, S.; Gao, J.; Guo, H.; Ha, S.; Joseph-McCarthy, D.; Kuchnir, L.; Kuczera, K.; Lau, F. T. K.; Mattos, C.; Michnick, S.; Ngo, T.; Nguyen, D. T.; Prodhom, B.; Reiher, W. E.; Roux, B.; Schlenkrich, M.; Smith, J. C.; Stote, R.; Straub, J.; Watanabe, M.; Wiorkiewicz-Kuczera, J.; Yin, D.; Karplus, M. *All-atom empirical potential for molecular modeling and dynamics studies of proteins* 1998, *Journal of Physical Chemistry B*, 102, 3586-3616.
55. Feller, S. E.; Zhang, Y. H.; Pastor, R. W.; Brooks, B. R. *Constant pressure molecular dynamics simulation—the Langevin piston method* 1995, *Journal of Chemical Physics*, 103, 4613-4621.
56. Essmann, U.; Perera, L.; Berkowitz, M. L.; Darden, T.; Lee, H.; Pedersen, L. G. *A smooth particle mesh Ewald method* 1995, *Journal of Chemical Physics*, 103, 8577-8593.
57. Irving, J. H.; Kirkwood, J. G. *The statistical mechanical theory of transport processes. IV. The equations of hydrodynamics* 1950, *Journal of Chemical Physics*, 18, 817-829.
58. Sonne, J.; Hansen, F. Y.; Peters, G. H. *Methodological problems in pressure profile calculations for lipid bilayers* 2005, *Journal of Chemical Physics*, 122, 124903, 1-9.
59. Harasima, A. *Molecular theory of surface tension* 1958, *Advances in Chemical Physics*, 1, 203-237.
60. Kaszycki, P.; Wasylewski, Z. *Fluorescence-quenching-resolved spectra of melittin in lipid bilayers* 1990, *Biochimica et Biophysica Acta: Protein Structure and Molecular Enzymology*, 1040, 337-345.
61. Seelig, J.; Browning, J. L. *General features of phospholipid conformation in membranes* 1978, *FEBS Letters*, 92, 41-44.
62. Feller, S. E.; Pastor, R. W. *Constant surface tension simulations of lipid bilayers: the sensitivity of surface areas and compressibilities* 1999, *Journal of Chemical Physics*, 111, 1281-1287.

-
63. Skibinsky A.; Venable, R. M.; Pastor, R. W. *A molecular dynamics study of the response of lipid bilayers and monolayers to trehalose* **2005**, Biophysical Journal, 89, 4111-4121.
64. Taylor, C.W. *The role of G proteins in transmembrane signaling* **1990**, Biochemical Journal, 272, 1-13.
65. Van der Wel, P. C. A.; Strandberg, E.; Killian, J. A.; Koeppe, R. E. *Geometry and intrinsic tilt of a tryptophan-anchored transmembrane α -Helix determined by ^2H NMR* **2002**, Biophysical Journal, 83, 1479-1488.
66. Aruya, T.; Takeuchi, H. *Raman linear intensity difference of membrane-bound peptides: indole ring orientations of tryptophans 11 and 13 in the gramicidin A transmembrane channel* **1997**, Biospectroscopy, 4, 171-184.
67. Kim, J. E.; McCamant, D. W.; Zhu, L.; Mathies, R. A. *Resonance raman structural evidence that the cis-to-trans isomerization in rhodopsin occurs in femtoseconds* **2001**, Journal of Physical Chemistry B, 105, 1240-1249.
68. Caesar, C.; Esbjorner, E. K.; Lincoln, P.; Norden, B. *Membrane interactions of cell-penetrating peptides probed by tryptophan fluorescence and dichroism techniques: correlations of structure to cellular uptake* **2006**, Biochemistry, 45, 7682-7692.
69. Im, W.; Brooks, C. L. *Interfacial folding and membrane insertion of designed peptides studied by molecular dynamics simulations* **2004**, Proceedings of the National Academy of Sciences, 102, 6771-6776.
70. Bond, P.; Sansom, M. S. P. *Insertion and assembly of membrane proteins via simulation* **2006**, Journal of the American Chemical Society, 128, 2697-2704.
71. Stevens, M. J. *Coarse-grained simulations of lipid bilayers* **2004**, Journal of Chemical Physics, 121, 11942-11948.
72. Lopez, C. F.; Nielsen, S.O.; Srinivas, G.; DeGrado, W. F.; Klein, M. L. *Probing membrane insertion activity of antimicrobial polymers via coarse-grain molecular dynamics* **2006**, Journal of Chemical Theory and Computation, 2, 649-655.
73. Haider, S.; Grottesi, A.; Hall, B. A.; Ashcroft, F. M.; Sansom, M. S. P. *Conformational dynamics of the ligand-binding domain of inward rectifier K channels as revealed by molecular dynamics simulations: toward an understanding of Kir channel gating* **2005**, Biophysical Journal, 88, 3310-3320.

-
74. Aliste, M. P.; Tieleman, D. P. *Computer simulation of partitioning of ten pentapeptides Ace-WLXLL at the cyclohexane/water and phospholipid/water interfaces* **2005**, BMC Biochemistry, 6, 30.
75. Wimley, W. C.; White, S. H. *Experimentally determined hydrophobicity scale for proteins at membrane interfaces* **1996**, Nature Structure Biology, 3, 842-848.
76. Bradshaw, J. P.; Darkes, M. J.; Malcom, J. M.; Harroun, T. A.; Katsaras, J.; Epanand, R. M. *Oblique membrane insertion of viral fusion peptide probed by neutron diffraction* **2000**, Biochemistry, 39, 6581-6585.
77. Liu, W.; Caffrey, M. *Interactions of tryptophan, tryptophan peptides and tryptophan alkyl esters at curved membrane interfaces* **2006**, Biochemistry, 45, 11713-11726.
78. Gorfe, A. A.; Pellarin, R.; Caflisch, A. *Membrane localization and flexibility of a lipidated ras peptide studied by molecular dynamics simulations* **2004**, Journal of the American Chemical Society, 126, 15277-15286.
79. Stepaniants, S.; Izrailev, S.; Schulten, K. *Extraction of lipids from phospholipid membranes by steered molecular dynamics* **1997**, Journal of Molecular Modeling, 3, 473-475.
80. Efremov, R.G.; Nolde, D.E.; Konshina, A.G.; Syrtcev, N.P.; Arseniev, A.S. *Peptides and proteins in membranes: what can we learn via computer simulations?* **2004**, Current Medicinal Chemistry, 11, 2421-2442.
81. Wimley, W. C.; Hristova, K.; Ladokhin, A. S.; Silvestro, L.; Axelsen, P. H.; White, S. H. *Folding of β -sheet membrane proteins: a hydrophobic hexapeptide model* **1998**, Journal of Molecular Biology, 277, 1091-1110
82. Wimley, W. C.; White, S. H. *Reversible unfolding of β -sheets in membranes: a calorimetric study* **2004**, Journal of Molecular Biology, 342, 703-711.
83. Paul, C.; Wang, J.; Wimley, W.C.; Hochstrasser, R. M.; Axelsen, P. H. *Vibrational coupling, isotopic editing, and beta-sheet structure in a membrane-bound polypeptide* **2004**, Journal of the American Chemical Society, 126, 5843-5850.
84. TriposTM, Inc. www.tripos.com , St. Louis, MO, U.S.A.
85. http://moose.bio.ucalgary.ca/index.php?page=Structures_and_Topologies
86. Berger, O.; Edholm, O.; Jahnig, F. *Molecular dynamics simulations of a fluid bilayer of dipalmitoylphosphatidylcholine at full hydration, constant pressure, and constant temperature* **1997**, Biophysical Journal, 72, 2002-2013.

-
87. Darden, T.; York, D.; Pedersen, L. *Particle mesh Ewald an $n\log(n)$ method for Ewald sums in large systems* **1993**, *Journal of Chemical Physics*, 98, 10089-10092.
88. Berendsen, H. J. C.; Postma, J. P. M.; DiNola, A.; Haak, J. R. *Molecular dynamics with coupling to an external bath* **1984**, *Journal of Chemical Physics*, 81, 3684-3690.
89. The MathWorks Inc, 1994-2006, <http://www.mathworks.com/>
90. Raudino, A.; Mauzerall, D. *Dielectric properties of the polar head group region of zwitterionic lipid bilayers* **1986**, *Biophysical Journal*, 50, 441-449.
91. Huang, W.; Levitt, D. G. *Theoretical calculation of the dielectric constant of a bilayer membrane* **1977**, *Biophysical Journal*, 17, 111-128.
92. Cherstvy, A. G. *Electrostatic screening and energy barriers of ions in low-dielectric membranes* **2006**, *Journal of Physical Chemistry B*, 110, 14503-14506.
93. Yau, W.; Wimley, W. C.; Gawrish, K.; White, S. H. *The preference of tryptophan for membrane interfaces* **1998**, *Biochemistry*, 37, 14713-14718.
94. Nelson, D. L.; Cox, M. M. *Lehninger Principles of Biochemistry* **2000**, 3rd Edition, Worth Publishers.
95. Hanke, W.; Methfessel, C.; Wilmsen, H. U.; Katz, E.; Jung, G.; Boheim, G. *Melittin and a chemically modified trichotoxin form alamethicin-type multi-state pores* **1983**, *Biochimica Biophysica Acta*, 727, 108-114.
96. Gullingsrud, J.; Babakhani, A.; McCammon, J. A. *Computational investigation of pressure profiles in lipid bilayers with embedded proteins* **2006**, *Molecular Simulation*, 32, 831-838.
97. Gullingsrud, J.; Schulten, K. *Gating of MscL studied by steered molecular dynamics* **2003**, *Biophysical Journal*, 85, 2087-2099.
98. Popot, J. L.; Engelman, D. M. *Membrane protein folding and oligomerization: the two-stage model* **1990**, *Biochemistry*, 29, 4031-4037.
99. Pardo-Lopez, L.; Gomez, I.; Raussell, C.; Sanchez, J.; Soberon, M.; Bravo, A. *Structural changes of the cryIAc oligomeric pre-pore from bacillus thuringiensis induced by N-Acetylgalactosamine facilitates toxin membrane insertion* **2006**, *Biochemistry*, 45, 10329-10336.

-
100. Keifer, P. A.; Peterkofsky, A.; Guangshun, W. *Effects of detergent alkyl chain length and chemical structure on the properties of a micelle-bound bacterial membrane targeting peptide* **2004**, *Analytical Biochemistry*, 331, 33-39.
 101. Kelkar, D. A.; Chattopadhyay, A. *Membrane interfacial localization of aromatic amino acids and membrane protein function* **2006**, *Journal of Biosciences*, 31, 297-302.
 102. Norman, K. E.; Nymeyer, H. *Indole localization in lipid membranes revealed by molecular simulation* **2006**, *Biophysical Journal*, 91, 2046-2054.
 103. Shai, Y. *Mechanism of the binding, insertion and destabilization of phospholipid bilayer membranes by α -helical antimicrobial and cell non-selective membrane-lytic peptides* **1999**, *Biochimica Biophysica Acta*, 1462, 55-70.
 104. Aungst, B. J. *Novel formulation strategies for improving oral bioavailability of drugs with poor membrane permeation or presystemic metabolism* **2006**, *Journal of Pharmaceutical Sciences*, 82, 979-987.
 105. Dykstra, M.; Cherukuri, A.; Sohn, H. W.; Tzeng, S. J.; Pierce, S. K. *Location is everything: lipid rafts and immune cell signaling* **2003**, *Annual Review of Immunology*, 21, 457-481.
 106. Rehmann, B.; Nascimbeni, M. *Immunology of hepatitis B virus and hepatitis C virus infection* **2004**, *Nature Reviews Immunology*, 5, 215-229.
 107. Mukherjee, S.; Maxfield, F. R. *Membrane domains* **2004**, *Annual Review of Cell and Developmental Biology*, 20, 839-866.
 108. Stevens, T. J.; Mizuguchi, K.; Arkin, I. T. *Distinct protein interfaces in transmembrane domains suggest an in vivo folding model* **2004**, *Protein Science*, 13, 3028-3037.
 109. Tang, M.; Waring, A. J.; Hong, M. *Phosphate-mediated arginine insertion into lipid membranes and pore formation by a cationic membrane peptide from solid-state NMR* **2007**, *Journal of the American Chemical Society*, 129, 11438-11446.
 110. Bringezu, F.; Wen, S.; Dante, S.; Hauss, T.; Majerowicz, M.; Waring, A. *The insertion of the antimicrobial peptide dicynthaurin monomer in model membranes: thermodynamics and structural characterization* **2007**, *Biochemistry*, 46, 5678-5686.
 111. Alaouie, A. M.; Lewis, R. N.; McElhaney, R. N. *Differential scanning calorimetry and fourier transform infrared spectroscopic studies of phospholipid organization and lipid-peptide interactions in nanoporous substrate-supported lipid model membranes* **2007**, *Langmuir*, 23, 7229-7234.

-
112. Caesar, C. E.; Esbjorner, E. K.; Lincoln, R.; Norden, B. *Membrane interactions of cell-penetrating peptides probed by tryptophan fluorescence and dichroism techniques: correlations of structure to cellular uptake* **2006**, *Biochemistry*, 45, 7682-7692.
 113. Hong, M. *Structure, topology, and dynamics of membrane peptides and proteins from solid-state NMR spectroscopy* **2007**, *Journal of Physical Chemistry B*, 111, 10340-10351.
 114. Wimley, W. C.; Creamer, T. P.; White, S. H. *Solvation energies of amino acid side chains and backbone in a family of host-guest pentapeptides* **1996**, *Biochemistry*, 35, 5109-5124.
 115. Han, X.; Hristova, K.; Wimley, W. C. *Protein folding in membranes: insights from neutron diffraction studies of a membrane β -sheet oligomer* **2008**, *Biophysical Journal*, 94, 492-505.
 116. Bond, P. J.; Sansom, M. S. *Insertion and assembly of membrane proteins via simulation* **2006**, *Journal of the American Chemical Society*, 128, 2697-2704.
 117. Ayton, G. S.; Blood, P. D.; Voth, G. A. *Membrane remodeling from N-BAR domain interactions: insights from multi-scale simulation* **2007**, *Biophysical Journal*, 92, 3595-3602.
 118. Gorfe, A. A.; Babakhani, A.; McCammon, J. A. *H-ras protein in a bilayer: interaction and structure perturbation* **2007**, *Journal of the American Chemical Society*, 129, 12280-12286.
 119. Gorfe, A. A.; Babakhani, A.; McCammon, J. A. *Free energy profile of H-ras membrane anchor upon membrane insertion* **2007**, *Angewandte Chemie International Edition*, 46, 8234-8237.
 120. MacCallum, J. L.; Bennett, W. F. D.; Tieleman, D. P. *Partitioning of amino acid side chains into lipid bilayers: results from computer simulations and comparison to experiment* **2007**, *Journal of General Physiology*, 129, 371-377.
 121. Bartels, C.; Karplus, M. *Multidimensional adaptive umbrella sampling: applications to main chain and side chain peptide conformations* **1997**, *Journal of Computational Chemistry*, 18, 1450-1462.
 122. Shroll, R. M.; Smith, D. E. *Molecular dynamics simulations in the grand canonical ensemble: formulation of a bias potential for umbrella sampling* **1999**, *Journal of Chemical Physics*, 110, 8295-8302.
 123. Babakhani, A.; Gorfe, A. A.; Gullingsrud, J.; Kim, J. E.; McCammon, J. A. *Peptide insertion, positioning, and stabilization in a membrane: insight from an all-atom molecular dynamics simulation* **2007**, *Biopolymers*, 85, 490-497.

-
124. Saccani, J.; Castano, S.; Desbat, B.; Blaudez, D. *A phospholipid bilayer supported under a polymerized langmuir film* **2003**, *Biophysical Journal*, 85, 3781-3787.
 125. Ramamoorthy, A.; Kandasamy, S. K.; Lee, D. K.; Kidambi, S.; Larson, R. G. *Structure, topology, and tilt of cell-signaling peptides containing nuclear localization sequences in membrane bilayers determined by solid-state NMR and molecular dynamics simulation studies* **2007**, *Biochemistry*, 46, 965-975.
 126. Chandler, D. *Interfaces and the driving force of hydrophobic assembly* **2005**, *Nature*, 437, 640-647.
 127. Li, F.; Gangal, M.; Juliano, C.; Gorfain, E.; Taylor, S. S.; Johnson, D. A. *Evidence for an internal entropy contribution to phosphoryl transfer: a study of domain closure, backbone flexibility, and the catalytic cycle of cAMP-dependent protein kinase* **2005**, *Journal of Molecular Biology*, 315, 459-469.
 128. Grossfield, A.; Woolf, T. B. *Interaction of tryptophan analogs with POPC lipid bilayers investigated by molecular dynamics calculations* **2002**, *Langmuir*, 18, 198-210.
 129. Narita, M.; Chen, J. Y.; Sato, H.; Kim, Y. *Influence of the nucleophilic and electrophilic properties of solvents for peptide solubilization: CD monitoring and the special effect of the water molecule* **1985**, *Bulletin Chemical Society of Japan*, 58, 2494-2501.
 130. Stevens, T. J.; Mizuguchi, K.; Arkin, I. T. *Distinct protein interfaces in transmembrane domains suggest an in vivo folding model* **2004**, *Protein Science*, 13, 3028-3037.
 131. Sheng, M.; Pak, D. T. S. *Ligand-gated ion channel interactions with cytoskeletal and signaling proteins* **2000**, *Annual Review Physiology*, 62, 755-778.
 132. Whatley, V. J.; Harris, R. A. *The cytoskeleton and neurotransmitter receptors* **1996**, *International Reviews Neurobiology*, 39, 113-143.
 133. Cami, J.; Farre, M. *Mechanisms of disease and drug addiction* **2003**, *New England Journal of Medicine*, 349, 975-986.
 134. Tanczos, A. C.; Palmer, R. A.; Potter, B. S.; Saldanha, J. W.; Howlin, B. J. *Antagonist binding in the rat muscarinic receptor: a study by docking and x-ray crystallography* **2004**, *Computational Biology and Chemistry*, 28, 375-385.
 135. Ehrenpreis, S.; Kellock, M. G. *Acetylcholine receptor protein and nerve activity. I. specific reaction of local anesthetics with the protein* **1960**, *Biochemical and Biophysical Research Communications*, 2, 311-313.

-
136. Buisson, B.; Bertrand, D. *Chronic exposure to nicotine upregulates the human alpha-4-beta-2 nicotinic acetylcholine receptor function* **2001**, *Journal of Neuroscience*, 21, 1819-1829.
137. Swanson, K. L.; Albuquerque, E. X. *Nicotinic acetylcholine receptor ion channel blockade by cocaine: the mechanism of synaptic action* **1987**, *Journal of Pharmacology and Experimental Therapeutics*, 243, 1202-1210.
138. Ivetac, A.; Sansom, M. S. P. *Molecular dynamics simulations and membrane protein structure quality* **2008**, *European Biophysical Journal*, 37, 403-409.
139. Unwin, N. *Refined structure of the nicotinic acetylcholine receptor at 4 Å resolution* **2005**, *Journal of Molecular Biology*, 346, 967-989.
140. Ulens, C.; Hogg, R. C.; Celie, P. H.; Bertrand, D.; Tsetlin, V.; Smit, A. B.; Sixma, T. K. *Structural determinants of selective alpha-conotoxin binding to a nicotinic acetylcholine receptor homolog of AChBP* **2006**, *Proceedings of the National Academy of Sciences*, 103, 3615-3620.
141. Brejc, K.; van Dijk, W. J.; Klaassen, R. V.; Schuurmans, M.; van der Oost, J.; Smit, A. B.; Sixma, T. K. *Crystal structure of an ACh-binding protein reveals the ligand-binding domain of nicotinic receptors* **2001**, *Nature*, 411, 269-276.
142. Celie, P. H. N.; van Rossum-Fikkert, S. E.; van Dijk, W. J.; Brejc, K.; Smit, A. B.; Sixma, T. K. *Nicotine and carbamylcholine binding to nicotinic acetylcholine receptors as studied in AChBP crystal structures* **2004**, *Neuron*, 41, 907-914.
143. Celie, P. H. N.; Kasheverov, I. E.; Mordvintsev, D. Y.; Hogg, R. C.; van Nierop, P.; van Elk, R.; van Rossum-Fikkert, S. E.; Zhmak, M. N.; Bertrand, D.; Tsetlin, V.; Sixma, T. K.; Smit, A. B. *Crystal structure of nicotinic acetylcholine receptor homolog AChBP in complex with an alpha-conotoxin PnIA variant* **2005**, *Nature Structure Molecular Biology*, 12, 582-588.
144. Hansen, S. B.; Sulzenbacher, G.; Huxford, T.; Marchot, P.; Taylor, P.; Bourne, Y. *Structures of Aplysia AChBP complexes with nicotinic agonists and antagonists reveal distinctive binding interfaces and conformations* **2005**, *European Molecular Biology Organization*, 24, 3635-3646.
145. Bourne, Y.; Talley, T. T.; Hansen, S. B.; Taylor, P.; Marchot, P. *Crystal structure of a Cbtx-AChBP complex reveals essential interactions between snake alpha-neurotoxins and nicotinic receptors* **2005**, *European Molecular Biology Organization*, 24, 1512-1522.

-
146. Hansen, S. B.; Radic, Z.; Talley, T. T.; Molles, B. E.; Deerinck, T.; Tsigelny, I.; Taylor, P. *Tryptophan fluorescence reveals conformational changes in the acetylcholine binding protein* **2002**, *Journal of Biological Chemistry*, 277, 41299-41302.
147. Talley, T. T.; Yalda, S.; Ho, K. Y.; Tor, Y.; Soti, F. S.; Kem, W. R.; Taylor, P. *Spectroscopic analysis of benzylidene anabaseine complexes with acetylcholine binding proteins as models for ligand-nicotinic receptor interactions* **2006**, *Biochemistry*, 45, 8894-8902.
148. Talley, T. T.; Olivera, B. M.; Han, K. H.; Christensen, S. B.; Dowell, C.; Tsigelny, I.; Ho, K. Y.; Taylor, P.; McIntosh, J. M. *Alpha-conotoxin OmlA is a potent ligand for the acetylcholine-binding protein as well as alpha-3-beta-2 and alpha-7 nicotinic acetylcholine receptors* **2006**, *Journal of Biological Chemistry*, 281, 24678-24686.
149. Fagen, Z. M.; Mitchum, R.; Vezina, P.; McGehee, D. S. *Enhanced nicotinic receptor function and drug abuse vulnerability* **2007**, *Journal of Neuroscience*, 27, 8771-8778.
150. <http://dtp.nci.nih.gov/index.html>
151. <http://flipdock.scripps.edu/>
152. Lin, J. H.; Perryman, A. L.; Schames, J. R.; McCammon, J. A. *Computational drug design accommodating receptor flexibility: the relaxed complex scheme* **2002**, *Journal of the American Chemical Society*, 124, 5632-5633.
153. Amaro, R. E.; Baron, R.; McCammon, J. A. *An improved relaxed complex scheme for receptor flexibility in computer-aided drug design* **2008**, *Journal of Computer Aided Molecular Design*, 22, 693-705.
154. Celie, P. H. N.; Klaassen, R. V.; van Rossum-Fikkert, S. E.; van Elk, R.; van Nierop, P.; Smit, A. B.; Sixma, T. K. *Crystal structure of acetylcholine-binding protein from *bulinus truncatus* reveals the conserved structural scaffold and sites of variation in nicotinic acetylcholine receptors* **2005**, *Journal of Biological Chemistry*, 280, 26457-26466.
155. Kaminski, G. A.; Friesner, R. A.; Tirado-Reves, J.; Jorgensen, W. L. *Evaluation and reparametrization of the OPLS-AA force field for proteins via comparison with accurate quantum chemical calculations on peptides* **2001**, *Journal of Physical Chemistry B*, 105, 6474-6487.

-
156. Morris, G. M.; Goodsell, D. S.; Halliday, R. S.; Huey, R.; Hart, W. E.; Belew, R. K.; Olson, A. J. *Automated docking using a lamarckian genetic algorithm and empirical binding free energy function* **1998**, *Journal of Computational Chemistry*, 19, 1639-1662.
157. Huey, R.; Morris, G. M.; Olson, A. J.; Goodsell, D. S. *A semiempirical free energy force field with charge-based desolvation* **2007**, *Journal of Computational Chemistry*, 28, 1145-1152.
158. Chang, M. W.; Lindstrom, W.; Olson, A. J.; Belew, R. K. *Analysis of HIV wild-type and mutant structures via in-silico docking against diverse ligand libraries* **2007**, *Journal of Chemical Informatics and Modeling*, 47, 1258-1262.
159. <http://www.nbcr.net/>
160. <http://129.43.27.140/ncidb2/>
161. Cromer, B. A.; Morton, C. J.; Parker, M. W. *Anxiety over GABA(A) receptor structure relieved by AChBP* **2002**, *Trends in Biochemical Sciences*, 27, 280-287.
162. Shi, J.; Koeppe, J. R.; Komives, E. A.; Taylor, P. *Ligand-induced conformational changes in the acetylcholine-binding protein analyzed by hydrogen-deuterium exchange mass spectrometry* **2006**, *Journal of Biological Chemistry*, 281, 12170-12177.
163. Gao, F.; Bren, N.; Burghardt, T. P.; Hansen, S.; Henchman, R. H.; Taylor, P.; McCammon, J. A.; Sine, S. M. *Agonist-mediated conformational changes in acetylcholine-binding protein revealed by simulation and intrinsic tryptophan fluorescence* **2005**, *Journal of Biological Chemistry*, 280, 8443-8451.
164. Liu, X.; Xu, Y.; Wang, X.; Barrantes, F. J.; Jiang, H. *Unbinding of nicotine from the acetylcholine binding protein: steered molecular dynamics simulations* **2008**, *Journal of Physical Chemistry B*, 112, 4087-4093.
165. Hansen, S. B.; Talley, T. T.; Radic, Z.; Taylor, P. *Structural and ligand recognition characteristics of an acetylcholine-binding protein from *aplysia californica** **2004**, *Journal of Biological Chemistry*, 279, 24197-24202.
166. Warren, G. L.; Andrews, C. W.; Capelli, A. M.; Clarke, B.; LaLonde, J.; Lambert, M. H.; Lindvall, M.; Nevins, N.; Semus, S. F.; Senger, S.; Tedesco, G.; Wall, I. D.; Woolven, J. M.; Peishoff, C. E.; Head, M. S. *A critical assessment of docking programs and scoring functions* **2006**, *Journal of Medicinal Chemistry*, 49, 5912-5931.

-
167. Hibbs, R. E.; Talley, T. T.; Taylor, P. *Acrylodan-conjugated cysteine side chains reveal conformational state and ligand site locations of the acetylcholine-binding protein* **2004**, *Journal of Biological Chemistry*, 279, 28483-28491.
168. Taylor, P.; Talley, T. T.; Radic, Z.; Hansen, S. B.; Hibbs, R. E.; Shi, J. *Structure-guided drug design: conferring selectivity among neuronal nicotinic receptor and acetylcholine-binding protein subtypes* **2007**, *Biochemical Pharmacology*, 74, 1164-1171.
169. Sixma, T. K.; Smit, A. B. *Acetylcholine binding protein (AChBP): a secreted glial protein that provides a high-resolution model for the extracellular domain of pentameric ligand-gated ion channels* **2003**, *Annual Reviews Biophysics and Biomolecular Structure*, 32, 311-334.
170. Gao, F.; Bren, N.; Little, A.; Wang, H. L.; Hansen, S. B.; Talley, T. T.; Taylor, P.; Sine, S. M. *Curariform antagonists bind in different orientations to acetylcholine-binding protein* **2008**, *Journal of Biological Chemistry*, 278, 23020-23026.
171. Talley, T. T.; Harel, M.; Hibbs, R. E.; Radic, Z.; Tomizawa, M.; Casida, J. E.; Taylor, P. *Atomic interactions of neonicotinoid agonists with AChBP: molecular recognition of the distinctive electronegative pharmacophore* **2008**, *Proceedings of the National Academy of Sciences*, 105, 7606-7611.
172. Schames, J. R.; Henchman, R. H.; Siegel, J. S.; Sotriffer, C. A.; Ni, H.; McCammon, J. A. *Discovery of a novel binding trench in HIV integrase* **2004**, *Journal of Medicinal Chemistry*, 47, 1879-1881.
173. Hibbs, R. E.; Radic, Z.; Taylor, P.; Johnson, D. A. *Influence of agonists and antagonists on the segmental motion of residues near the agonist binding pocket of the acetylcholine-binding protein* **2006**, *Journal of Biological Chemistry*, 281, 39708-39718.
174. Schaloske, R. H.; Dennis, E. A. *The phospholipase A2 superfamily and its group numbering system* **2006**, *Biochimica et Biophysica Acta*, 1761, 1246-1259.
175. Six, D. A.; Dennis, E. A. *The expanding superfamily of phospholipase A2 enzymes: classification and characterization* **2000**, *Biochimica Biophysica Acta*, 1488, 1-19.
176. Clark, J. D.; Milona, N.; Knopf, J. L. *Purification of a 110-kilodalton cytosolic phospholipase A2 from the human monocytic cell line U937* **1990**, *Proceedings of the National Academy of Sciences USA*, 87, 7708-7712.
177. Clark, J. D.; Lin, L. L.; Kriz, R. W.; Ramesha, C. S.; Sultzman, L. A.; Lin, A. Y.; Milona, N.; Knopf, J. L. *A novel arachidonic acid-selective cytosolic PLA2*

-
- contains a Ca²⁺-dependent translocation domain with homology to PKC and GAP* **1991**, Cell, 65, 1043-1051.
178. Funk, C. D. *Prostaglandins and leukotrienes: advances in eicosanoid biology* **2001**, Science, 294, 1871-1875.
179. Bonventre, J. V.; Huang, Z.; Taheri, M. R.; O' Leary, E.; Li, E.; Moskowitz, M. A.; Sapirstein, A. *Reduced fertility and postischaemic brain injury in mice deficient in cytosolic phospholipase A2* **1997**, Nature, 390, 622-625.
180. Nagase, T.; Uozumi, N.; Ishii, S.; Kume, K.; Izumi, T.; Ouchi, Y.; Shimizu, T. *Acute lung injury by sepsis and acid aspiration: key role for cytosolic phospholipase A2* **2000**, Nature Immunology, 1, 42-46.
181. Uozumi, N.; Kume, K.; Nagase, T.; Nakatani, N.; Ishii, S.; Tashiro, F.; Komagata, Y.; Maki, K.; Ikuta, K.; Ouchi, Y.; Miyazaki, J.; Shimizu, T. *Role of cytosolic phospholipase A2 in allergic response and parturition* **1997**, Nature, 390, 618-622.
182. Pickard, R. T.; Chiou, X. G.; Striffler, B. A.; DeFelippis, M. R.; Hyslop, P. A.; Tebbe, A. L.; Yee, Y. K.; Reynolds, L. J.; Dennis, E. A.; Kramer, R. M.; Sharp, J. D. *Identification of essential residues for the catalytic function of 85-kDa cytosolic phospholipase A2: probing the role of histidine, aspartic acid, cysteine, and arginine* **1996**, Journal of Biological Chemistry, 271, 19225-19231.
183. Dessen, A.; Tang, J.; Schmidt, H.; Stahl, M.; Clark, J. D.; Sehra, J.; Somers, W. S. *Human cytosolic phospholipase A2* **1999**, Cell, 97, 349-360.
184. Liu, S.; Laliberte, F.; Falguyret, J. P.; Street, I.; Huang, Z. *Methyl arachidonyl fluorophosphonate, a potent irreversible CPLA2 inhibitor blocks the mobilization of arachidonic-acid in human platelets, neutrophils and differentiated U937 cells* **1995**, FASEB Journal, 9, A1310-A1310.
185. Riendeau, D.; Guay, J.; Weech, P. K.; Laliberte, F.; Yergey, J.; Li, C.; Desmarais, S.; Perrier, H.; Liu, S.; Nicoll-Griffith, D. *Arachidonyl trifluoromethyl ketone, a potent inhibitor of 85-kDa phospholipase A2, blocks production of arachidonate and 12-hydroxyeicosatetraenoic acid by calcium ionophore-challenged platelets* **1994**, Journal of Biological Chemistry, 269, 15619-15624.
186. Trimble, L. A.; Street, I. P.; Perrier, H.; Tremblay, N. M.; Weech, P. K.; Bernstein, M. A. *NMR structural studies of the tight complex between a trifluoromethyl ketone inhibitor and the 85-kDa human phospholipase A2* **1993**, Biochemistry, 32, 12560-12565.

-
187. McKew, J. C.; Lovering, F.; Clark, J. D.; Bemis, J.; Xiang, Y.; Shen, M.; Zhang, W.; Alvarez, J. C.; Joseph-McCarthy, D. *Structure-activity relationships of indole cytosolic phospholipase A(2)alpha inhibitors: substrate mimetics* **2003**, *Bioorganic Medicinal Chemistry Letters*, 13, 4501-4504.
188. McKew, J. C.; Foley, M. A.; Thakker, P.; Behnke, M. L.; Lovering, F. E.; Sum, F. W.; Tam, S.; Wu, K.; Shen, M. W.; Zhang, W.; Gonzalez, M.; Liu, S.; Mahadevan, A.; Sard, H.; Khor, S. P.; Clark, J. D. *Inhibition of cytosolic phospholipase A2alpha: hit to lead optimization* **2006**, *Journal of Medicinal Chemistry*, 49, 135-158.
189. Lee, K. L.; Foley, M. A.; Chen, L.; Behnke, M. L.; Lovering, F. E.; Kirincich, S. J.; Wang, W.; Shim, J.; Tam, S.; Shen, M. W.; Khor, S.; Xu, X.; Goodwin, D. G.; Ramarao, M. K.; Nickerson-Nutter, C.; Donahue, F.; Ku, M. S.; Clark, J. D.; McKew, J. C. *Discovery of Ecopladib, an indole inhibitor of cytosolic phospholipase A2alpha* **2007**, *Journal of Medicinal Chemistry*, 50, 1380-400.
190. McKew, J. C.; Lee, K. L.; Shen, M. W.; Thakker, P.; Foley, M. A.; Behnke, M. L.; Hu, B.; Sum, F. W.; Tam, S.; Hu, Y.; Chen, L.; Kirincich, S. J.; Michalak, R.; Thomason, J.; Ipek, M.; Wu, K.; Wooder, L.; Ramarao, M. K.; Murphy, E. A.; Goodwin, D. G.; Albert, L.; Xu, X.; Donahue, F.; Ku, M. S.; Keith, J.; Nickerson-Nutter, C. L.; Abraham, W. M.; Williams, C.; Hegen, M.; Clark, J. D. *Indole cytosolic phospholipase A2 alpha inhibitors: discovery and in vitro and in vivo characterization of 4-{3- [5- chloro- 2- (2- {(3,4-dichlorobenzyl)sulfonyl}amino)ethyl]- 1- (diphenylmethyl)- 1H-indol- 3-yl]propyl}benzoic acid, efipladib* **2008**, *Journal of Medicinal Chemistry*, 51, 3388-3413.
191. Seno, K.; Okuno, T.; Nishi, K.; Murakami, Y.; Watanabe, F.; Matsuura, T.; Wada, M.; Fujii, Y.; Yamada, M.; Ogawa, T.; Okada, T.; Hashizume, H.; Kii, M.; Hara, S.; Hagishita, S.; Nakamoto, S.; Yamada, K.; Chikazawa, Y.; Ueno, M.; Teshirogi, I.; Ono, T.; Ohtani, M. *Pyrrolidine Inhibitors of Human Cytosolic Phospholipase A2* **2000**, *Journal of Medicinal Chemistry*, 43, 1041-1044.
192. Seno, K.; Okuno, T.; Nishi, K.; Murakami, Y.; Yamada, K.; Nakamoto, S.; Ono, T. *Pyrrolidine inhibitors of human cytosolic phospholipase A2. Part 2: synthesis of potent and crystallized 4-triphenylmethylthio derivative 'pyrrophenone'* **2001**, *Bioorganic and Medicinal Chemistry Letters*, 11, 587-590.
193. Ono, T.; Yamada, K.; Chikazawa, Y.; Ueno, M.; Nakamoto, S.; Okuno, T.; Seno, K. *Characterization of a novel inhibitor of cytosolic phospholipase A2a, pyrrophenone* **2002**, *Biochemical Journal*, 363, 727-735.

-
194. Flamand, N.; Picard, S.; Lemieux, L.; Pouliot, M.; Bourgoin, S. G.; Borgeat, P. *Effects of pyrrophenone, an inhibitor of group IVA phospholipase A2, on eicosanoid and PAF biosynthesis in human neutrophils* **2006**, *British Journal of Pharmacology*, 149, 385-392.
195. Ludwig, J.; Bovens, S.; Brauch, C.; Elfringhoff, A. S.; Lehr, M. *Design and synthesis of 1-indol-1-yl-propan-2-ones as inhibitors of human cytosolic phospholipase A(2)alpha* **2006**, *Journal of Medicinal Chemistry*, 49, 2611-2620.
196. Hess, M.; Elfringhoff, A. S.; Lehr, M. *1-(5-carboxy- and 5-carbamoylindol-1-yl)propan-2-ones as inhibitors of human cytosolic phospholipase A(2)alpha: Bioisosteric replacement of the carboxylic acid and carboxamide moiety* **2007**, *Bioorganic and Medicinal Chemistry* **2007**, 15, 2883-2891.
197. Fritsche, A.; Elfringhoff, A. S.; Fabian, J.; Lehr, M. *1-(2-Carboxyindol-5-yl)oxy)propan-2-ones as inhibitors of human cytosolic phospholipase A(2)alpha: synthesis, biological activity, metabolic stability, and solubility* **2008**, *Bioorganic and Medicinal Chemistry*, 16, 3489-3500.
198. Kokotos, G.; Kotsovolou, S.; Six, D. A.; Constantinou-Kokotou, V.; Beltzner, C. C.; Dennis, E. A. *Novel 2-oxo amide inhibitors of human group IVA phospholipase A2* **2002**, *Journal of Medicinal Chemistry*, 45, 2891-2893.
199. Kokotos, G.; Six, D. A.; Loukas, V.; Smith, T.; Constantinou-Kokotou, V.; Hadjipavlou-Litina, D.; Kotsovolou, S.; Chiou, A.; Beltzner, C. C.; Dennis, E. A. *Inhibition of group IVA cytosolic phospholipase A2 by novel 2-oxoamides in vitro, in cells, and in vivo* **2004**, *Journal of Medicinal Chemistry*, 47, 3615-3628.
200. Stephens, D.; Barbayianni, E.; Constantinou-Kokotou, V.; Peristeraki, A.; Six, D. A.; Cooper, J.; Harkewicz, R.; Deems, R. A.; Dennis, E. A.; Kokotos, G. *Differential inhibition of group IVA and group VIA phospholipases A2 by 2-Oxoamides* **2006**, *Journal of Medicinal Chemistry*, 49, 2821-2828.
201. Six, D. A.; Barbayianni, E.; Loukas, V.; Constantinou-Kokotou, V.; Hadjipavlou-Litina, D.; Stephens, D.; Wong, A. C.; Magrioti, V.; Moutevelis-Minakakis, P.; Baker, S. F.; Dennis, E. A.; Kokotos, G. *Structure-activity relationship of 2-oxoamide inhibition of group IVA cytosolic phospholipase A2 and group V secreted phospholipase A2* **2007**, *Journal of Medicinal Chemistry*, 50, 4222-4235.
202. Gopalsamy, A.; Yang, H.; Ellingboe, J. W.; McKew, J. C.; Tam, S.; Joseph-McCarthy, D.; Zhang, W.; Shen, M.; Clark, J. D. *1,2,4-Oxadiazolidin-3,5-diones and 1,3,5-triazin-2,4,6-triones as cytosolic phospholipase A2alpha inhibitors* **2006**, *Bioorganic Medicinal Chemistry Letters*, 16, 2978-81.

-
203. Yaksh, T. L.; Kokotos, G.; Svensson, C. I.; Stephens, D.; Kokotos, C. G.; Fitzsimmons, B.; Hadjipavlou-Litina, D.; Hua, X. Y.; Dennis, E. A. *Systemic and intrathecal effects of a novel series of phospholipase A2 inhibitors on hyperalgesia and spinal prostaglandin E2 release* **2006**, *Journal of Pharmacology and Experimental Therapeutics*, 316, 466-475.
204. Hamuro, Y.; Anand, G. S.; Kim, J. S.; Juliano, C.; Stranz, D. D.; Taylor, S. S.; Woods, V. L., Jr. *Mapping intersubunit interactions of the regulatory subunit (RIa) in the type I holoenzyme of protein kinase A by enhanced amide hydrogen/deuterium exchange mass spectrometry* **2004**, *Journal of Molecular Biology*, 340, 1185-1196.
205. Mandell, J. G.; Falick, A. M.; Komives, E. A. *Identification of protein-protein interfaces by decreased amide proton solvent accessibility* **1998**, *Proceeding of the National Academy of Sciences USA*, 95, 14705-14710.
206. Brudler, R.; Gessner, C. R.; Li, S.; Tyndall, S.; Getzoff, E. D.; Woods, V. L., Jr. *PAS domain allostery and light-induced conformational changes in photoactive yellow protein upon I2 intermediate formation, probed with enhanced hydrogen/deuterium exchange mass spectrometry* **2006**, *Journal of Molecular Biology*, 363, 148-160.
207. Hoofnagle, A. N.; Resing, K. A.; Goldsmith, E. J.; Ahn, N. G. *Changes in protein conformational mobility upon activation of extracellular regulated protein kinase-2 as detected by hydrogen exchange* **2001**, *Proceedings of the National Academy of Sciences*, 98, 956-961.
208. Wales, T. E.; Engen, J. R. *Hydrogen exchange mass spectrometry for the analysis of protein dynamics* **2006**, *Mass Spectrometry Reviews*, 25, 158-170.
209. Burke, J. E.; Karbarz, M. J.; Deems, R. A.; Li, S.; Woods, V. L., Jr.; Dennis, E. A. *Interaction of group IA phospholipase A2 with metal ions and phospholipid vesicles probed with deuterium exchange mass spectrometry* **2008**, *Biochemistry*, 48, 6451-6459.
210. Brier, S.; Lemaire, D.; DeBonis, S.; Forest, E.; Kozielski, F. *Molecular dissection of the inhibitor binding pocket of mitotic kinesin Eg5 reveals mutants that confer resistance to antimetabolic agents* **2006**, *Journal of Molecular Biology*, 360, 360-376.
211. Brier, S.; Lemaire, D.; DeBonis, S.; Kozielski, F.; Forest, E. *Use of hydrogen/deuterium exchange mass spectrometry and mutagenesis as a tool to identify the binding region of inhibitors targeting the human mitotic kinesin Eg5* **2006**, *Rapid Communications in Mass Spectrometry*, 20, 456-462.

-
212. Wee, C. L.; Balali-Mood, K.; Gavaghan, D.; Sansom, M. S. P. *The interaction of phospholipase A2 with a phospholipid bilayer: coarse-grained molecular dynamics simulations* **2008**, *Biophysical Journal*, 95, 1649-1657.
213. Bala, P.; Grochowski, P.; Nowinski, K.; Lesyng, B.; McCammon, J. A. *Quantum and quantum-classical studies of phosphoryl-transfer mechanisms in model systems* **2000**, *Biophysical Journal*, 79, 1253-1262.
214. Hsu, Y. H.; Burke, J. E.; Stephens, D. L.; Deems, R. A.; Li, S.; Asmus, K. M.; Woods, V. L., Jr.; Dennis, E. A. *Calcium binding rigidifies the C2 domain and the intradomain interaction of GIVA phospholipase A2 as revealed by hydrogen/deuterium exchange mass spectrometry* **2008**, *Journal of Biological Chemistry*, 283, 9820-9827.
215. Lucas, K. K.; Dennis, E. A. *Distinguishing phospholipase A2 types in biological samples by employing group-specific assays in the presence of inhibitors* **2005**, *Prostaglandins and Other Lipid Mediators*, 77, 235-248.
216. Peitsch, M. C. *ProMod and Swiss-Model: Internet-based tools for automated comparative protein modeling* **1996**, *Biochemical Society Transactions*, 24, 274-279.